Properties of the integrated spectrum of active galactic nuclei

Pooja Chaudhary

München 2011

Properties of the integrated spectrum of active galactic nuclei

Pooja Chaudhary

Dissertation
an der Fakultät für Physik
der Ludwig–Maximilians–Universität
München

zur Erlangung des Grades
Doktor der Naturwissenschaften
Dr.rer.nat.

vorgelegt von
Pooja Chaudhary
aus Uttar Pradesh, India

München, Oktober 2011

Erstgutachter: Prof. Dr. Ralf Bender
Zweitgutachter: Prof. Kirpal Nandra
Tag der mündlichen Prüfung: den 24. November 2011

Contents

1 Introduction **1**
- 1.1 A brief history of AGNs . . . 2
- 1.2 Observational characteristics of AGNs . . . 3
  - 1.2.1 Broad band continuum . . . 3
  - 1.2.2 Broad and high ionization emission lines . . . 4
  - 1.2.3 Variability . . . 6
  - 1.2.4 Jets and outflows . . . 7
- 1.3 X-ray emission from AGNs . . . 8
- 1.4 The unified model for AGNs . . . 11
- 1.5 Accretion onto a black hole . . . 15
  - 1.5.1 Basic parameters . . . 15
  - 1.5.2 The Eddington limit . . . 16
  - 1.5.3 Accretion disks . . . 17
  - 1.5.4 Accretion disk coronae . . . 18
- 1.6 Iron Kα line . . . 21
  - 1.6.1 The iron line profile . . . 23
  - 1.6.2 Dependence of the line profile on disk inclination and emissivity . . . 25
  - 1.6.3 Dependence of the line profile on the inner disk radius and black hole spin 26
- 1.7 Observations of iron lines in AGNs . . . 27
- 1.8 This thesis . . . 29
- 1.9 Outline of the thesis . . . 29

2 Sample preparation **31**
- 2.1 XMM-*Newton* observatory . . . 31
- 2.2 The 2XMM catalog . . . 33
- 2.3 Quality evaluation of the archival products . . . 36
- 2.4 The sample . . . 36

3 Properties of the integrated spectrum of serendipitous 2XMM catalog sources **41**
- 3.1 Rationale . . . 41
- 3.2 Splitting the sample in redshift and luminosity bins . . . 42
- 3.3 Computation and spectral fitting of the integrated spectrum . . . 43
  - 3.3.1 Contribution from single sources . . . 44

3.4 Simulations . . . 47
3.5 Results and Discussion . . . 56
3.5.1 Evolution of the Fe line equivalent width with redshift . . . 56
3.5.2 The IT effect . . . 57
3.6 Conclusions . . . 60

4 Rest-frame stacking of 2XMM catalog sources: Properties of the Fe Kα line 63
4.1 Rationale . . . 63
4.2 The sample . . . 64
4.3 Rest-frame stacking procedures . . . 66
4.3.1 Stacked ratio . . . 66
4.3.2 Stacked spectrum . . . 68
4.3.3 Simulations . . . 69
4.4 Results . . . 70
4.4.1 "Averaged ratio flux spectrum" fitting . . . 70
4.4.2 "Averaged X-ray spectrum" fitting . . . 73
4.4.3 Complex fits . . . 76
4.5 Discussion . . . 79
4.6 Conclusions . . . 84

5 Summary and future perspectives 87
5.1 Future perspectives . . . 89

Appendix 91
A.1 Background normalization in XSPEC . . . 91
A.2 Observed-frame stacking procedure . . . 92
A.3 The sample . . . 94

Bibliography 103

Acknowledgments 114

List of Figures

1.1 Schematic representation of the broadband continuum spectral energy distribution (SED) observed in the different types of AGNs 4
1.2 Optical spectra of many different types of AGNs as compared to a normal galaxy 5
1.3 Examples of line and continuum flux variability seen at different wavelengths in various types of AGNs 6
1.4 Hubble Space Telescope (HST) high-resolution spectrum of the C IV λ1550 region in the Seyfert 1 galaxy NGC 5548 7
1.5 Monte Carlo simulations of the X-ray reflection spectrum from a slab of uniform density neutral matter with solar abundances 10
1.6 A schematic representation of the intrinsic type-1 (unabsorbed) AGN X-ray spectrum in the 0.1–400 keV 11
1.7 Schematic picture illustrating the main components of an AGN as postulated by the unified model 12
1.8 A series of schematic, logarithmic views of the basic AGN components embedded in the host galaxy 13
1.9 Possible geometries for an accretion disk corona 21
1.10 Ionized reflection spectra for different ionization parameters 23
1.11 Schematic illustration of the iron line shape distortion caused by the interplay of Doppler and transverse Doppler shifts, relativistic beaming, and gravitational redshifting. 24
1.12 The dependence of the line profile on the observer inclination and disk emissivity profile 25
1.13 The dependence of the line profile on the inner disk radius 26

2.1 On-axis effective area of the EPIC-PN and EPIC-MOS1 cameras on-board XMM-*Newton* 32
2.2 A simplified schematic of the data processing steps undertaken in the creation of the 2XMM catalog 35
2.3 Comparison of the EPIC-PN spectra extracted from the raw observation data files with the pipeline processed archival spectra for four sources 37
2.4 An example 2XMM EPIC-PN 0.2–12 keV image in which the background annulus is contaminated by three sources 38

2.5 Comparison of the distributions of the EPIC-PN net counts and flux in the observed-frame 0.2–12 keV band for the total sample of 2646 point sources selected from the 2XMM catalog, its sub-sample of 919 objects with redshift available and our final sample of 507 sources 39

3.1 Spectral fits to the stacked spectra in different redshift and luminosity bins (1) . . 46
3.2 Spectral fits to the stacked spectra in different redshift and luminosity bins (2) . . 47
3.3 Comparison of the simulated and real stacked spectra (1) 49
3.4 Comparison of the simulated and real stacked spectra (2) 50
3.5 Histograms of the simulated stacked spectrum fit parameters in the redshift bins (1) 51
3.6 Histograms of the simulated stacked spectrum fit parameters in the redshift bins (2) 52
3.7 Comparison of the power law photon indices of the real and simulated stacked spectra in the quoted redshift and luminosity bins 53
3.8 Comparison of the 2–10 keV X-ray luminosities of the real and simulated stacked spectra in the quoted redshift and luminosity bins 54
3.9 Comparison of the narrow Fe Kα lines equivalent widths in the real and simulated stacked spectra in the quoted redshift and luminosity bins 55
3.10 Rest-frame equivalent width as a function of redshift. 56
3.11 Variation of the narrow Fe Kα line equivalent width with the X-ray luminosity in the redshift range $0 < z < 5$ 58
3.12 Variation of the narrow Fe Kα line equivalent width with the X-ray luminosity in the redshift range $0 < z < 0.8$ 59
3.13 X-ray luminosity dependence of the power law photon index 60

4.1 Comparison of the distributions of the net counts, power law photon indices, redshifts and X-ray luminosities for the reference (final) sample of 507 sources and the sample of 248 sources selected for the rest-frame stacking analysis 65
4.2 Six redshift corrected source spectra grouped in 26 predefined energy bins in the 2–10 keV band 67
4.3 Comparison of the mean ratio profiles 68
4.4 Ratio of the “averaged X-ray spectrum” with respect to a power law overlaid with the mean ratio profile of the 248 sources created using 3–sigma clipping . . 69
4.5 Averaged ratio of the 248 spectra after applying 3–sigma clipping, mean simulated continuum along with its 1σ and 3σ confidence limits 70
4.6 Spectral fits to the “averaged ratio flux spectrum” 72
4.7 Contour plots of the `diskline` versus narrow component intensities for the “averaged ratio flux spectrum” 74
4.8 Contour plots of the `diskline` versus narrow component intensities for the “averaged X-ray spectrum” 74
4.9 Spectral fits to the “averaged X-ray spectrum” 75

4.10 Spectral fit to the "averaged ratio flux spectrum" using a model including a power law, a distant neutral reflector and a diskline 77
4.11 Spectral fit to the "averaged ratio flux spectrum" using a power law and dual neutral reflection spectra 77
4.12 Spectral fits to the "averaged X-ray spectrum" using complex models 80
4.13 Equivalent width of the narrow Fe Kα line measured from the spectral fitting of the "averaged ratio flux spectrum" and "averaged X-ray spectrum" of the total sample comprising 248 AGNs and the sub-samples used in three hard X-ray luminosity bins 82
4.14 Comparison of the equivalent width of the broad Fe Kα line measured from the spectral fitting of the "averaged ratio flux spectrum" and "averaged X-ray spectrum" of the total sample comprising 248 AGNs 83

List of Tables

3.1 Statistics of the sources 42
3.2 Results of spectral fitting in different redshift bins. 45

4.1 Results of the “averaged ratio flux spectrum” spectral fitting in the 3–10 keV . . . 81
4.2 Results of the “averaged X-ray spectrum” spectral fitting in the 3–10 keV 81
4.3 Results of the “averaged ratio flux spectrum” and “averaged X-ray spectrum” spectral fitting in the 3–10 keV using complex models 81

A.3 Properties of the final sample 94

Galaxies are a prominent component of the universe. The central regions or nuclei of many galaxies are the sites of energetic phenomena, which cannot be related to ordinary stellar processes. These nuclei emit prodigious amounts of energy of the order of 10^{44} to 10^{48} erg s^{-1} and are therefore capable of outshining the power emitted by the entire host galaxy by several orders of magnitudes. The emission is widely spread across the electromagnetic spectrum with the peak in the ultraviolet and a substantial fraction in the X-ray and infrared bands. Galaxies harboring these nuclei are called active galactic nuclei (AGNs).

AGNs are thought to be powered by material accreting onto supermassive black holes. When observed in the X-ray waveband AGNs are found to be very bright and rapidly variable (on time scales as small as 1000 sec, implying that the X-ray emission must originate from the innermost regions of the central engine) and exhibit distinct spectral features. The iron Kα emission line at 6.4 keV (Fe Kα) is the most prominent spectral line observed in the X-ray spectra of AGNs and is a useful probe to various physical properties of the nuclear region. Therefore, the X-ray spectroscopic observations of AGNs can be used to probe the physics of accretion flows in the immediate environment of these objects.

With the current instrumentation, the X-ray spectroscopic observations of AGNs are still in the photon-limited regime in most cases, and the study of the Fe Kα emission lines are limited to small samples of nearby bright objects. The low photon counting statistics in the X-ray spectra of distant AGNs prevents a full characterization of the spectral parameters in these objects. This problem can be solved by employing the spectral averaging ("stacking") techniques which improve the counting statistics and provide an insight into the average physical properties of faint AGNs.

This thesis is aimed at characterizing the properties of the integrated spectrum of AGNs, such as the ubiquity of the Fe Kα emission in AGNs, the dependence of the spectral parameters (e.g. the power law photon index and the Fe Kα equivalent width etc.) on the X-ray luminosity and redshift, and mean properties (including the line profile) of the Fe Kα line which can be addressed via stacking in the source rest-frame.

I selected 2646 point sources observed with XMM-*Newton* at high galactic latitude ($|BII| > 25$ degrees) and with the sum of EPIC-PN and EPIC-MOS 0.2–12 keV counts greater than 1000. Redshifts were obtained for 919 sources from the Nasa's Extragalactic Database. In order to prepare a clean sample, I retained only reliable sources (those for which the detection and the spectral products do not show obvious problems). I also excluded sources classified as HII regions, groups/clusters, star-forming/starburst galaxies. The final sample consists of 507 AGNs.

To examine the ubiquity of the Fe Kα emission in AGNs and the dependence of the spectral parameters on the X-ray luminosity and redshift, I employed the observed-frame stacking technique, in which individual source spectra were summed in the observed-frame to compute the integrated spectra in different redshift and luminosity bins over the range $0 < z < 5$. Detailed analysis of these spectra used appropriately normalized background spectra and exposure time-weighted response and ancillary files. I find that the narrow Fe Kα line at 6.4 keV is significantly detected up to $z = 1$. The line equivalent width decreases with increasing the X-ray luminosity in the 2–10 keV band ("Iwasawa-Taniguchi effect"). The anticorrelation is characterized by the relation $\log(EW_{Fe}) = (1.66 \pm 0.09) + (-0.43 \pm 0.07)\log(L_{X,44})$, where EW_{Fe} is the rest-frame equivalent width of the neutral Fe Kα line in eV and $L_{X,44}$ is the 2–10 keV X-ray luminosity in

units of 10^{44} erg s^{-1}. The equivalent width is nearly independent of redshift up to $z \sim 0.8$ with an average value of 101 ± 40 (rms dispersion) eV in the luminosity range $43.5 \leq \log L_X \leq 44.5$. This analysis also confirms the hardening of the spectral indices at low luminosities, implying a dependence of obscuration on luminosity.

To derive the mean properties of the Fe Kα line in the source rest-frame, I refined the final sample of 507 AGNs and selected 248 AGNs with the EPIC-PN net 2–10 keV rest-frame counts ≥200 and power law photon indices in the range 1.5–2.2. I computed the integrated spectrum of these 248 AGNs in the source rest-frame using two different rest-frame stacking procedures. I carried out a detailed spectral analysis of these integrated spectra using various models comprising simple/complex continuum and Fe Kα line components. I find that the average Fe Kα line profile in our sample is best represented by a combination of a narrow and a broad line. The equivalent widths of the narrow and broad components are ∼30 eV and ∼100 eV, respectively. The broad line parameters such as its shape, equivalent width and its detection significance in the integrated spectrum of the 248 AGNs are observed to be very sensitive to the assumed continuum and adopted stacking method. However, despite having a well-defined sample with reasonable statistics (net counts ∼ 198000) in the integrated spectrum, I do not detect a clear extended red-wing, and the measured equivalent width of the broad feature is always lower than 170 eV, implying that most black holes are not maximally rotating.

Galaxien sind eine markante Komponente des Universums. In den zentralen Regionen oder Kernen vieler Galaxien finden energetische Phänomene statt, die nicht durch gewöhnliche stellare Prozesse erklärbar sind. Diese Kerne emittieren ungeheure Mengen an Energie in der Größenordnung von 10^{44} bis 10^{48} erg s^{-1} und können damit die emittierte Strahlungsleistung der gesamten Host-Galxie um mehrere Größenordnungen übertreffen. Die Emission ist weit über das elektromagnetische Spektrum verteilt, mit dem Maximum im Ultravioletten und einem erheblichen Anteil im Röntgen- und Infrarot-Band. Galaxien, die diese Kerne beheimaten, werden als Aktive Galaktische Kerne (Active Galactic Nuclei, AGNs) bezeichnet.

Es wird vermutet, dass AGNs ihre Leistung aus Materie beziehen, die auf supermassive schwarze Löcher akkretiert wird. Im Röntgenlicht beobachtet erscheinen AGNs sehr hell und schnell variabel (auf so kurzen Zeitskalen wie 1000 Sekunden, was impliziert, dass die Röntgenemission von der innersten Region der zentralen Maschine stammen muss) und zeigen ausgeprägte spektrale Merkmale. Die Eisen Kα Emissionslinie bei 6.4 keV (Fe Kα) ist die markanteste in Röntgenspektren von AGNs beobachtete Spektrallinie, und sie ist ein hilfreiches Testobjekt für verschiedene physikalische Eigenschaften der Kernregion. Daher können spektroskopische Röntgenbeobachtungen von AGNs dazu verwendet werden, um die Physik der Akkretionsströme in der unmittelbaren Umgebung dieser Objekte zu testen.

Mit gegenwärtigen Instrumenten finden spektroskopische Röntgenbeobachtungen von AGNs noch meist im Photonen-limitierten Regime statt und Studien der Fe Kα Emissionslinien sind auf wenige Stichproben von nahen hellen Objekten beschränkt. Die niedrige Photonenenstatistk in den Röntgenspektren von fernen AGNs macht eine volle Charakterisierung der spektralen Parameter dieser Objekte unmöglich. Dieses Problem kann gelöst werden durch Anwendung von Techniken der spektralen Mittelung ("stacking"), welche die Statistik verbessern und einen Einblick in die mittleren physikalischen Eigenschaften von schwachen AGNs erlauben.

Die vorliegende Arbeit zielt auf die Charakterisierung der Eigenschaften des integrierten Spektrums von AGNs, wie z.B. die Allgegenwart der Fe Kα Emission in AGNs, die Abhängigkeit der spektralen Parameter (z.B. des Photon-Index des Potenzgesetzes und die Fe Kα Äquivalentbreite, etc.) von der Röntgenleuchtkraft und der Rotverschiebung, sowie mittlere Eigenschaften (inclusive des Linienprofils) der Fe Kα Linie, die durch Stacking im Ruhesystem der Quelle untersucht werden können.

Ich habe 2646 mit XMM-*Newton* bei hoher galaktischer Breite ($|BII| > 25$ Grad) beobachtete Punktquellen ausgewählt, mit einer Gesamtzahl an counts in EPIC-PN und EPIC-MOS 0.2–12 keV größer als 1000. Rotverschiebungen wurden für 919 Quellen aus Nasa's Extragalactic Database gewonnen. Um eine saubere Stichprobe zu erhalten, habe ich nur verlässliche Quellen (für die die Detektion und die spektralen Produkte keine offensichtlichen Probleme aufzeigen) behalten. Zusätzlich habe ich als HII Regionen, Gruppen/Haufen oder sternbildende Galaxien klassifizierte Quellen ausgeschlossen. Die endgültige Stichprobe besteht aus 507 AGNs.

Um die Allgegenwart der Fe Kα Emission in AGNs und die Abhängigkeit der spektralen Parameter von der Röntgenleuchtkraft und der Rotverschiebung zu untersuchen, verwendete ich die "observed-frame stacking technique", bei der einzelne Quellspektren im Ruhesystem des Beobachters aufsummiert wurden, um integrierte Spektren in verschiedenen Rotverschiebungs- und Leuchtkraft-Bins im Bereich $0 < z < 5$ zu berechnen. Eine detaillierte Analyse dieser Spektren verwendete entsprechend normalisierte Hintergrundspektren und mit der Belichtungszeit

gewichtete Response- und Ancilliary-Dateien.

Ich beobachte, dass die schmale Fe Kα Linie bei 6.4 keV bis zu $z = 1$ signifikant detektiert wird. Die Äquivalentbreite der Linie nimmt ab mit zunehmender Röntgenleuchtkraft im Band 2–10 keV ("Iwasawa-Taniguchi Effekt"). Die Antikorrelation ist durch die Relation $\log(EW_{Fe}) = (1.66 \pm 0.09) + (-0.43 \pm 0.07) \log(L_{X,44})$ charakterisiert, wobei EW_{Fe} die Ruhesystem-Äquivalentbreite der neutralen Fe Kα line in eV und $L_{X,44}$ die Röntgenleuchtkraft im Band 2–10 keV in Einheiten von 10^{44} erg s^{-1} darstellen. Bis $z \sim 0.8$ ist die Äquivalentbreite nahezu unabhängig von der Rotverschiebung mit einem mittleren Wert von 101 ± 40 (RMS Dispersion) eV im Leuchtkraft-Bereich $43.5 \leq \log L_X \leq 44.5$. Des weiteren bestätigt diese Analyse das härter-Werden des spektralen Index bei niedrigen Leuchtkräften, was eine Abhängigkeit des Verdunkelungsgrades von der Leuchtkraft impliziert.

Um die mittleren Eigenschaften der Fe Kα Linie im Ruhesystem der Quelle herzuleiten, verfeinerte ich die Stichprobe von 507 AGNs und wählte 248 AGNs aus, mit einer Mindestanzahl an Netto-counts in EPIC-PN im 2–10 keV Ruhesystem von ≥200 und Photon-Indizes des Potenzgesetz im Bereich 1.5–2.2. Ich berechnete das integrierte Spektrum dieser 248 AGNs im Ruhesystem der Quelle mit zwei verschiedenen Ruhesystem Stacking-Methoden. Ich habe eine detaillierte spektrale Analyse dieser integrierten Spektren durchgeführt, unter Anwendung verschiedener Modelle, welche Komponenten für einfache/komplexe Kontinua und Fe Kα Linien umfassten.

Ich beobachte, dass das mittlere Fe Kα Linienprofil in unserer Stichprobe am besten durch eine Kombination aus einer schmalen und einer breiten Linie repräsentiert wird. Die Äquivalentbreiten der schmalen und breiten Komponenten sind ∼30 eV bzw. ∼100 eV. Die Parameter der breiten Linie, wie z.B. ihre Form, Äquivalentbreite und Detektions-Signifikanz im integrierten Spektrum von 248 AGNs scheinen sehr sensitiv vom angenommenen Kontinuum und der verwendeten Stacking-Methode abzuhängen.

Trotz der Verwendung einer wohl definierten Stichprobe mit angemessener Statistik (Netto-counts ∼ 198000) im integrierten Spektrum finde ich jedoch keine klare erweiterte rote Flanke und die gemessene Äquivalentbreite der breiten Struktur ist durchgehend kleiner als 170 eV, was impliziert, dass die meisten schwarzen Löcher nicht maximal rotieren.

Chapter 1

Introduction

Active galactic nuclei (AGNs) are among the most luminous sources in the universe. The term AGN refers to the existence of energetic phenomena at the centers of many galaxies, which cannot be related to the ordinary stellar processes as in "normal galaxies". AGNs emit strong radiation over the full range of electromagnetic spectrum – from radio waves to γ-rays. The access to most regions of electromagnetic spectrum now available with several ground and space observatories have revealed that these objects display complex phenomenology. Their properties include not only bright emission lines but also strong thermal and nonthermal continua, X-ray and radio emission. This complexity is further enhanced by myriad classification and sub-classifications of AGNs resulted from the multiwavelength observations. Since the first identification of AGNs in 1943 (Seyfert 1943), understanding the physical processes responsible for their complex behavior and the possible association between different types of AGNs has been one of the key research area in astrophysics.

Many models have been developed to account for the enormous energy output of AGNs (for a good discussion of some of the main hypotheses and their basic properties see Ginzburg & Ozernoi 1977; Terlevich et al. 1992). However, the most widely accepted model of the energy source of AGNs is accretion of matter onto supermassive black holes (SMBH) (Salpeter 1964; Lynden-Bell 1969; Rees 1984). Most of the accretion power is released in the innermost region around the central SMBH (Shakura & Sunyaev 1973; Pringle 1981), where the emerging spectrum is significantly affected by strong relativistic effects (Page & Thorne 1974; Cunningham 1975). In this chapter, we present a brief overview of AGNs phenomena and of the physical mechanisms giving rise to the observed emission. The description is not intended to be comprehensive. In-depth reviews of the topics discussed here can be found in (Peterson 1997, an observational perspective of AGNs), (Krolik 1999, theoretical consideration of AGNs), (Fabian et al. 2000; Reynolds & Nowak 2003; Fabian & Miniutti 2005; Miller 2007, fluorescent iron lines).

1.1 A brief history of AGNs

The observational study of AGNs started more than a century ago with the work of Fath in 1908, who first identified six emission lines in the spectrum of NGC 1068. In 1943, Carl K. Seyfert carried out a systematic study of a small sample of "normal" spiral galaxies. Seyfert obtained optical spectra of these galaxies and noticed the presence of high-excitation nuclear emission lines in the spectra of six galaxies (NGC 1068, NGC 1275, NGC 3516, NGC 4051, NGC 4151, NGC 7469). He noted that these galaxies have nuclei of high luminosity and their emission lines are broad with widths up to ~8500 km s^{-1}. Seyfert's work (Seyfert 1943) laid the foundation for a distinct class of galaxies characterized by an exceeding luminous stellar or semistellar nucleus and prominent broad emission lines. However, these galaxies, now known as Seyfert galaxies, did not receive any further attention until 1955, when NGC 1068 and NGC 1275 were detected as radio sources.

The boom in AGNs research occurred in the late 1950s following advances in radio astronomy. Several sky surveys were performed to identify the strongest radio sources associated with individual optical objects. The third Cambridge (3C) catalog (Edge et al. 1959) and its revised version, the 3CR catalog (Bennett & Smith 1961) detected the brightest radio sources in the northern sky. Most of these radio sources were identified with resolved galaxies. The sources 3C 48 and 3C 273 were the two sources that were identified with stellar objects. Optical spectra of these objects revealed blue continua with very strong broad emission lines at unidentified wavelengths. Many astronomers were puzzled by the strange nature of these objects.

The first breakthrough in understanding these extraordinary objects came in 1963, when Martin Schmidt (Schmidt 1963) realized that the emission lines seen in the spectrum of 3C 273 are actually the Balmer lines at an unusually high redshift of $z = 0.158$. This redshift was among the largest ever measured at that time. The derived absolute magnitude ($M_B = -26$) of 3C 273 implied that 3C 273 was about 100 times as luminous as normal bright spirals like the Milky Way ($M_B = -20.5$). Once the redshift mystery was solved, identification of lines in 3C 48 (Greenstein 1963) and other similar objects followed quickly. Due to their strong radio emission and star like appearance, these sources were dubbed "quasi-stellar radio sources", a term soon shortened to quasars.

Quasars were considered to be valuable astrophysical probes as their extremely high luminosities implied the existence of extreme physical conditions that were not found elsewhere in the nearby universe. Cosmological importance of quasars was also recognized, since they could be detected and identified at very large distances due to their high luminosities. These considerations provided early and continuing strong motivation for finding quasars and studying their properties. Thanks to optical sky surveys, more than 100000 quasars are now known (Schneider et al. 2010). Currently the object ULASJ1120+0641 holds the redshift record among the quasars with $z = 7.085$ (Mortlock et al. 2011).

AGNs emit a significant fraction (10–20%) of their bolometric luminosity as X-rays. As a comparison, emission in X-ray from normal galaxies is of the order of a few percent. Therefore, the X-ray selection is the cleanest possible method to assemble complete samples of AGNs. The X-ray properties of AGNs have been intensively studied in the last few decades. The first detections of AGNs in X-rays were performed by balloon-borne or rocket experiments in the

1960s (Bowyer et al. 1970), however only very crude measurements were possible. Dedicated X-ray satellites launched in the 1970s enabled observations of large samples of AGNs. The X-ray spectral analysis was performed on the brightest sources (see Mushotzky et al. 1993, for a review of these early results). Observations by the *Ariel-V* observatory established that the X-ray emission and its variability on timescales greater than one day are common properties of AGNs (Elvis et al. 1978; Marshall et al. 1981). The detections of high redshift quasars were made possible only with the *Einstein* observatory owing to its high source detection sensitivity. Since then many technologically advanced X-ray observatories, in particular *Ginga*, *ROSAT*, *ASCA*, *BeppoSAX*, *INTEGRAL*, *Chandra*, XMM-*Newton*, *Swift* and *Suzaku* have enabled the spectral and timing measurements of a wide variety of lower luminosity, more typical AGNs over a broad range of X-ray energies and constrained their cosmological evolution (Brandt & Hasinger 2005).

1.2 Observational characteristics of AGNs

The field of AGN research is a diverse one with many types of AGNs known. AGNs can be broadly classified into three main categories: Seyfert galaxies, quasars and blazars. Seyfert galaxies are nearby, spiral galaxies with modest bolometric luminosities (10^{43} erg s^{-1} to 10^{45} erg s^{-1}). Quasars are more luminous than Seyfert galaxies and are particularly numerous at a redshift of $\simeq$2. About 10% of quasars are strong sources of radio emission and are therefore called “radio-loud”, the remaining 90% are “radio-quiet”, although not silent. Radio loudness is generally associated either directly with a collimated relativistic outflow or jet or with regions where a jet has collided with surrounding material. A blazar is seen when our line of sight lies close to the direction of a jet. In this section, the observational characteristics of AGNs are discussed, with more emphasis on the X-ray component.

1.2.1 Broad band continuum

AGNs produce large amounts of radiation over the entire observable wavelength range, from X-rays and γ-rays through long-wavelength radio waves. The broad spectral energy distribution or SED is one of the defining characteristics of AGNs. The SED carry important information on the physical processes at work in AGNs. A schematic representation of the broadband continuum spectral energy distribution observed in the different types of AGNs is displayed in Fig. 1.1. Compared to the SED of a normal galaxy, which has two main peaks (in the optical and infrared regions respectively from starlight and cool dust emission), the AGN SED has a much broader distribution with nearly equal amount of energy per unit logarithmic frequency interval from radio through X-rays. In addition, the SEDs of AGNs show notable features as labeled in Fig. 1.1. For radio-quiet AGNs, this broadband spectrum can be divided into three major components: the infrared bump, the Big Blue Bump, and the X-ray region.

The Big Blue Bump (BBB) continuum component in AGNs generally extends from the near-infrared at $\sim$1 μm to past 1000 Å in the ultraviolet (UV) region of the spectrum. Unobscured AGNs emit a substantial fraction (>50%) of their bolometric luminosities within this spectral range. Therefore, the origin of this component is directly related to the primary energy produc-

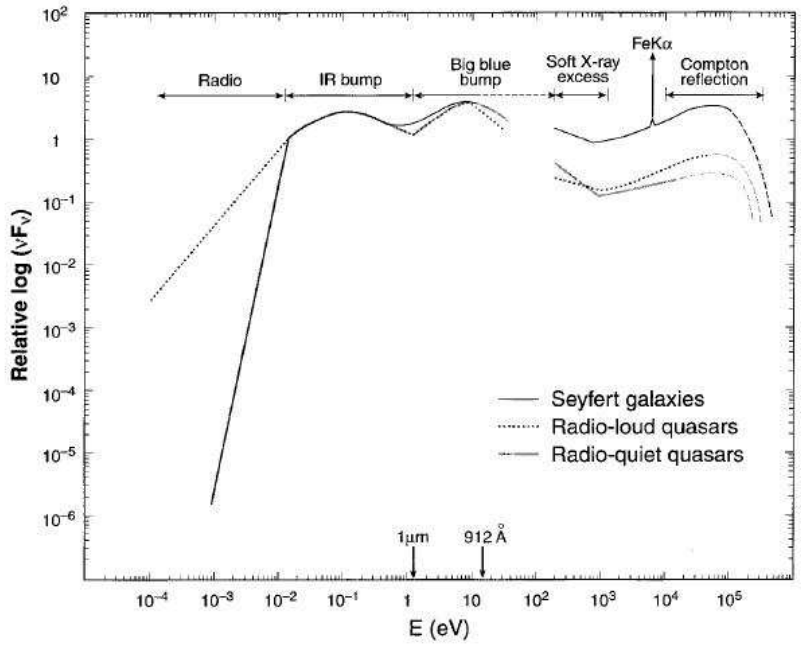

Figure 1.1: Schematic representation of the broadband continuum spectral energy distribution (SED) observed in the different types of AGNs. Labels represent primary spectral features in the SED. Figure taken from Koratkar & Blaes (1999), their figure 1.

tion mechanism. The BBB is ascribed to thermal emission from the gas in an accretion disk surrounding the SMBH.

The broad infrared bump extends from ~100 to ~1 μm. Quasars show a local minimum in the vicinity of 1 μm and have a sharp cutoff in the sub-millimeter. The infrared bump is thought to originate from reprocessing of the BBB emission by dust with temperatures in the range 10–1800 K and at a range of distances from the central UV source (Barvainis 1987, 1990).

There is a significant observational gap in the extreme ultraviolet (~10^{16} Hz) region of the spectrum. The EUV gap is primarily due to the opacity of the interstellar medium in our own Galaxy that prevents the observations. In the X-ray region, the AGN's SED consists of several notable features, e.g. a soft X-ray excess, power law continuum, Fe Kα line and Compton reflection. We discuss these features in detail in Section 1.3.

1.2.2 Broad and high ionization emission lines

The presence of strong emission lines in the optical-UV spectra was one of the original distinguishing characteristic of AGNs. These lines serve as a key diagnostic tool to probe the physical state of the material (e.g. temperature and density etc.) in the regions producing the lines. Emission lines in AGNs come in two categories: (i) strong, permitted lines, e.g. hydrogen Balmer series lines (Hα λ6563, Hβ λ4861, Hγ λ4340), hydrogen Lyα λ1216, and prominent lines of abundant ions (Mg II λ2798, C III λ1909, C IV λ1549) and (ii) weak, forbidden lines, e.g. [O

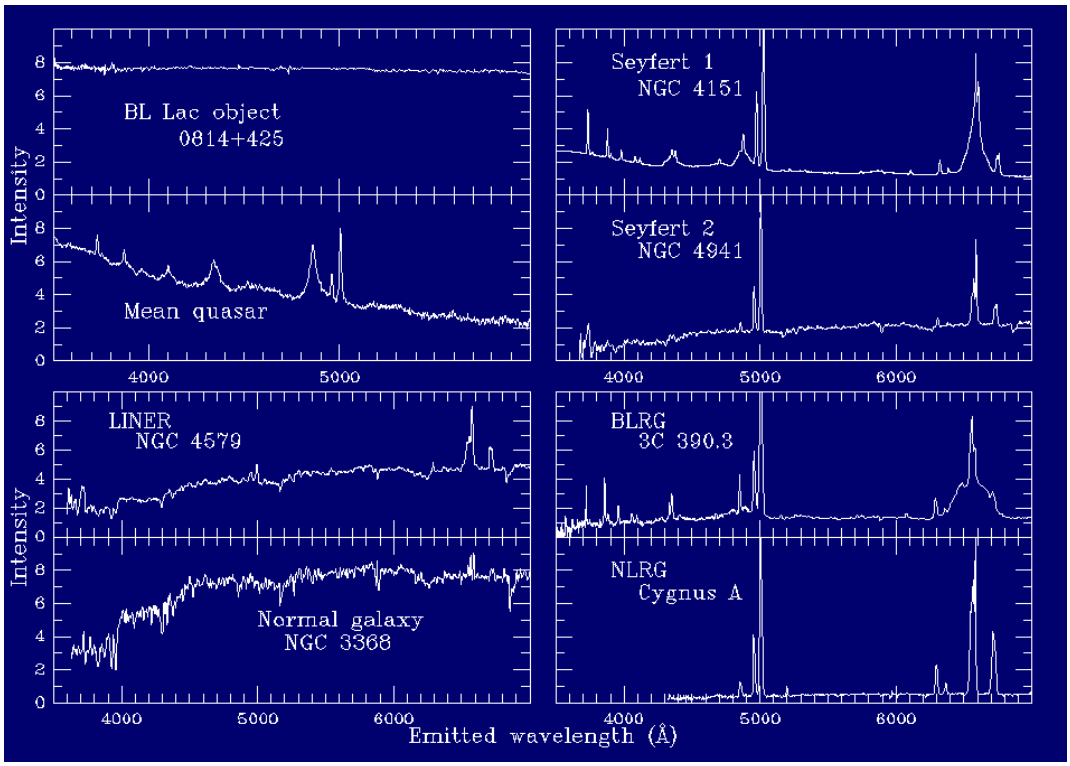

Figure 1.2: Optical spectra of many different types of AGNs as compared to a normal galaxy (NGC 3368). Strong emission lines are present in all AGNs spectra (e.g. Seyfert 1 (NGC 4151), Seyfert 2 (NGC 4941), BLRG (3C 3903), NLRG (Cygnus A) and Mean quasar) except the BL Lacs object 0814+425 and LINER (NGC 4579), where these lines are absent or comparatively weaker. Variation in the line widths in different AGNs is also noticeable. Figure taken from on-line material of William C. Keel.

III] (λ4363, λ4959, λ5007) and [O II] λ3727. The permitted lines are observed to be broad with the full width half maximum (Δv_{FWHM}) > 1000 km s^{-1}, while the forbidden lines are observed to be narrow with Δv_{FWHM} < 1000 km s^{-1}. The widths of these lines are generally interpreted as Doppler shifts due to bulk motion of gas in the producing regions.

Different types of AGNs reveal variation in their emission line profiles as illustrated in Fig. 1.2, which displays the optical spectrum of Seyfert 1 and 2 galaxies, a mean quasar, a LINER (Low-ionization emission region) galaxy, a BL Lacertae, broad and narrow line radio galaxies (BLRG and NLRG respectively) along with that of a normal galaxy. As compared to the normal galaxy spectrum (the *lower left panel* in Fig. 1.3) which is dominated by stellar absorption lines, all AGNs spectra show prominent emission lines except the BL Lacs object (the *upper left panel* in Fig. 1.3) and LINER (the *lower left panel* in Fig. 1.3), where these lines are absent or comparatively weaker. It is interesting to note that Seyfert 2 and narrow line objects completely lack the broad emission lines observed in Seyfert 1 and broad line radio galaxies. This variation in the emission line profiles observed in various types of AGNs played a key role in the genesis of unification schemes, which will be discussed in Section 1.4.

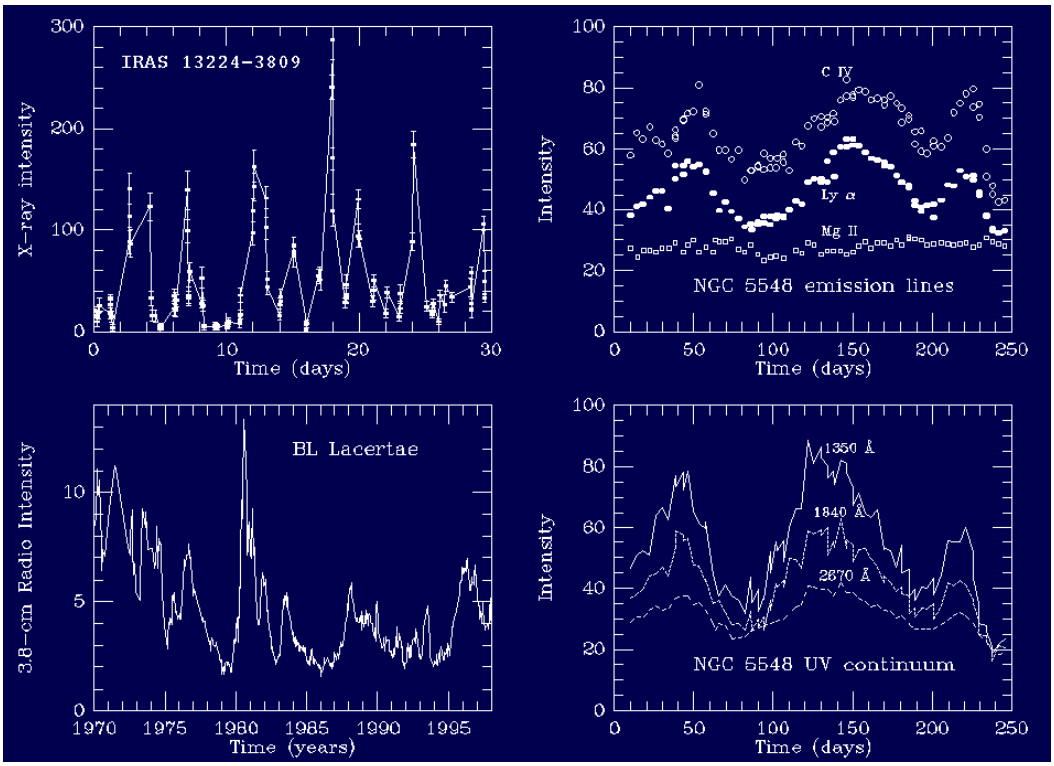

Figure 1.3: Examples of line and continuum flux variability seen at different wavelengths in various types of AGNs. The *top left panel* shows the ROSAT X-ray light curve of radio-quiet, narrow line Seyfert 1 galaxy IRAS 13224-3809, which is one of the well-studied AGN showing rapid X-ray variability, on time scale of days this source varies by more than a factor of 20. The *bottom left panel* is the radio light curve of BL Lacertae at λ = 3.8 cm covering a period of 28 years. Emission lines and continuum light curves of Seyfert galaxy NGC 5548 measured at three ultraviolet wavelengths are shown in the *right panels*. Figure taken from on-line material of William C. Keel.

1.2.3 Variability

AGNs exhibit variability in the continuum and line fluxes in almost all energy bands in which they have been observed, from X-ray to radio wavelengths (for a review see Ulrich et al. 1997). The observed variability timescales in AGNs range from a few hundred seconds to years. Figure 1.3 shows a few examples of the line and continuum flux variability seen at different wavelengths in AGNs. The examples include two Seyfert galaxies (IRAS 13224-3809 and NGC 5548) and one BL Lacertae. Comparison of the three continuum bands and emission lines light curves of NGC 5548 shows that the continuum is most variable in the deep ultraviolet (1350 Å) and the Lyα and C IV emission lines follow the continuum changes closely, while Mg II does not show any significant variation. This implies that the Lyα and C IV lines come from areas a few light-days in extent, while Mg II originates in a region at least light-months in radius. Variability studies are therefore of great importance as they allow to put tight constrains on the size of the emitting region.

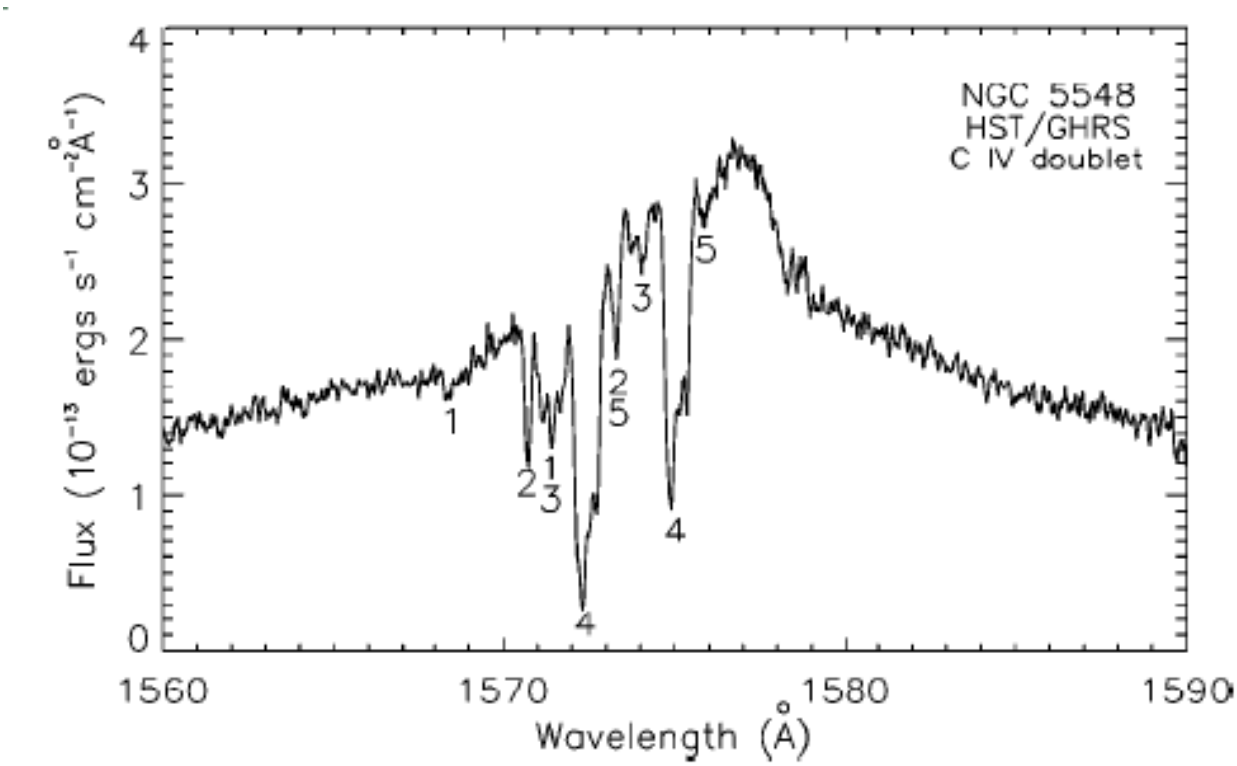

Figure 1.4: HST high-resolution spectrum of the C IV λ1550 region in the Seyfert 1 galaxy NGC 5548 showing strong, multicomponent absorption lines superimposed on the broad C IV emission line. There are five separate regions at different velocities producing the absorption. Each region appears twice because C IV λ1550 is a doublet separated by 3 Å. Figure taken from Crenshaw et al. (2003).

1.2.4 Jets and outflows

As already mentioned, a small fraction ($\lesssim$10%) of AGNs are radio-loud, while the remaining 90% appear to be radio-quiet sources. Typical radio-loud AGNs have radio continuum emission that is about 1000 times brighter than a typical radio-quiet AGNs (see Fig. 1.1 for comparison of the SED of radio-loud and radio-quiet AGNs). According to Kellermann et al. (1989), radio-loud AGNs have high radio-loudness parameter (R > 10), where R is the flux ratio at 4.85 GHz and 4400 Å. Some radio-loud AGNs exhibit highly columnized jet-like structures and giant lobes which extend on kiloparsec scales from the center of the host galaxy. These structures are believed to be due to nuclear material expelled from supermassive black hole vicinity at significant fractions of the speed of the light.

The optical-UV and X-ray spectra of many AGNs show emission lines with blueshifted broad absorption troughs. The absorption is always detected at wavelengths shortward of the line center (blueshifted), which indicates that the absorbing gas is outflowing from the nucleus. Figure 1.4 is the HST high-resolution spectrum of the C IV λ1550 region in the Seyfert 1 galaxy NGC 5548.

It shows many sharp absorption features produced by multiple, outflowing regions of highly ionized material moving towards us with different speeds. Many models have been proposed to explain the origin and means of acceleration of mass outflow in AGNs. Among the most popular physical models of the dynamics of mass outflow are thermal wind arising from the putative accretion disk, radiation pressure driven accretion disk wind, and accretion driven wind (see Crenshaw et al. 2003, for a review).

1.3 X-ray emission from AGNs

The X-ray emission from AGNs extends from the Galactic absorption cutoff at ~0.1 keV to ~300 keV. To the first order, the intrinsic AGN spectrum can be described by a power law (photon flux $F(E) \propto E^{-\Gamma}$, where E is the photon energy and Γ is the power law photon index). The most promising physical mechanism to produce such power law component is Compton upscattering of soft photons from a geometrically thin, optically thick accretion disk in a hot and possibly extended electron plasma, the "accretion disk corona" (Haardt & Maraschi 1991, 1993; Haardt et al. 1994). The photon index lies in the range 1.8–2.0 for low luminosity Seyfert galaxies and high luminosity quasars. Radio-loud AGNs are observed to have a comparatively flatter spectrum with Γ between 1.5 and 1.7. The difference between radio-loud and radio-quiet X-ray spectral shapes is ascribed to the additional hard component emitted by inverse Compton scattering taking place within the jet's inner regions.

High resolution and better signal-to-noise data available over a wide energy range demonstrate that the AGN X-ray spectrum deviates from a simple power law. The first indications of any spectral complexity in the X-ray emission from Seyferts came from the *EXOSAT* observatory which had a bandpass extending from 0.05 keV in the soft X-ray band to 50 keV in the hard X-ray domain. It was found that at low energies ($\lesssim$1 keV) there was a rise in the spectrum above the extrapolation of the hard X-ray power law. This "soft-excess" (e.g. Arnaud et al. 1985) was found to occur in about half of all Seyferts (Turner & Pounds 1989). Subsequent ROSAT observations by Walter & Fink (1993) suggested that the fraction of AGNs exhibiting soft-excess was much higher (~90%). Recent studies based on the XMM-*Newton* data have confirmed the existence of this spectral feature in a large majority of Seyferts and quasars (Pounds & Reeves 2002; Porquet et al. 2004). However, the physical origin of the soft-excess is an open question. This feature has been assigned several interpretations, e.g. the high energy continuation of the BBB or comptonization of EUV accretion disk photons (Arnaud et al. 1985; Kawaguchi et al. 2001; Porquet et al. 2004) and reprocessing of the hard X-ray power law through reflection and scattering of X-rays off the optically thick disk (George & Fabian 1991). Ionized disk reflection has also been proposed as an explanation (Crummy et al. 2006; Ross & Fabian 2005).

The soft X-ray spectra of Seyfert galaxies also show other spectral features called as "warm absorber". The warm absorber is believed to arise from an optically-thin ionized gas along the line of sight. The term warm absorber was first introduced by Halpern (1984) to explain the unusual spectrum of the QSO MR 2251–178. However, it was not fully characterized until *ROSAT* observations detected an oxygen absorption edge at ~0.8 keV in the soft X-ray spectrum of MCG–6–30–15 (Nandra & Pounds 1992). The high sensitivity ASCA observations of Seyferts

galaxies found evidence of the presence of O VII (0.739 keV) and O VIII (0.871 keV) absorption edges in ∼50% of the sample sources (George et al. 1998). The high resolution grating spectrographs on-board the *Chandra* and XMM-*Newton* X-ray observatories are revolutionizing the study of warm absorber. Hundreds of absorption and emission lines from various atomic species have been resolved in a few AGNs (e.g. Kaspi et al. 2002; Behar et al. 2003). These lines are generally blueshifted with outflow velocities of hundreds to thousands km s^{-1}(e.g. Blustin et al. 2007). This fact, combined with the high ionization state of the gas, implies that the material is exposed to the extreme radiation environment of the central AGN, however its geometry and location remain unknown.

At hard X-ray energies as well, AGNs spectra show considerable spectral complexities, which were first discovered with the *Ginga* observatory. Pounds et al. (1990) and Nandra & Pounds (1994) reported that almost all Seyfert galaxies had a strong iron (Fe) Kα emission line at 6.4 keV. These *Ginga* data also showed a spectral flattening at $E > 8$ keV and a Compton reflection hump peaking at ∼30 keV. These features can be attributed to the reprocessing of the primary X-ray continuum ("X-ray reflection") in optically thick material subtending a substantial solid angle to the X-ray source (Lightman & White 1988; Guilbert & Rees 1988; George & Fabian 1991; Matt et al. 1991), possibly the putative accretion disk. Because of the energy dependence of the photoelectric absorption cross section ($\sigma_{pe} \propto E^{-3}$), the X-ray photons from the accretion disk corona with energies >> 10 keV will mainly interact with the accretion disk through Compton scattering off the bound electrons of the disk material. Since the relative energy change per Compton scatter is $\Delta E/E \sim -E/m_e c^2$, these photons are typically downscattered in energy. For photon energies << 10 keV, photoelectric absorption is the dominant mechanism of interaction. The interplay between photoelectric absorption at low and Compton scattering at high energies results in the formation of a broad hump like structure around 20–30 keV (the so-called Compton hump).

The absorption of photons in the inner shell of atoms in the accretion disk also produces fluorescent line emission from transitions of the outer shell electrons to the inner shell vacancy caused by the photoabsorption. Owing to a combination of large cosmic abundance and high fluorescent yield, the Fe Kα line is the most prominent fluorescent line in the X-ray reflection spectrum. An example of a Monte Carlo calculation of the X-ray reflection spectrum from a neutral and uniform density semi-infinite slab of gas is shown in Fig. 1.5 where fluorescent emission lines dominate at energies below 8 keV and the Compton reflection hump is seen above 20 keV (from Fabian et al. 2000).

In AGNs, the accretion disk is not the only reflector able to produce the X-ray reflection spectrum. The dusty molecular torus surrounding the accreting system at the parsec scale (a key AGN component hypothesized in the unification models) acts as an additional reflector producing a spectrum very similar to that seen in Fig. 1.5. Special and general relativistic effects shape the reflection spectrum originated from the center of the accretion disk and not that from regions far away from the central black hole (such as the torus). The accretion disk and torus contributions to the reflection spectrum can therefore be disentangled. However, the precise measurements are complex and require high resolution broad band spectral data.

The first broad band (0.1–200 keV) spectra of AGNs with high signal-to-noise ratio were provided by the *BeppoSAX* observatory. The *BeppoSAX* data established the ubiquitous presence

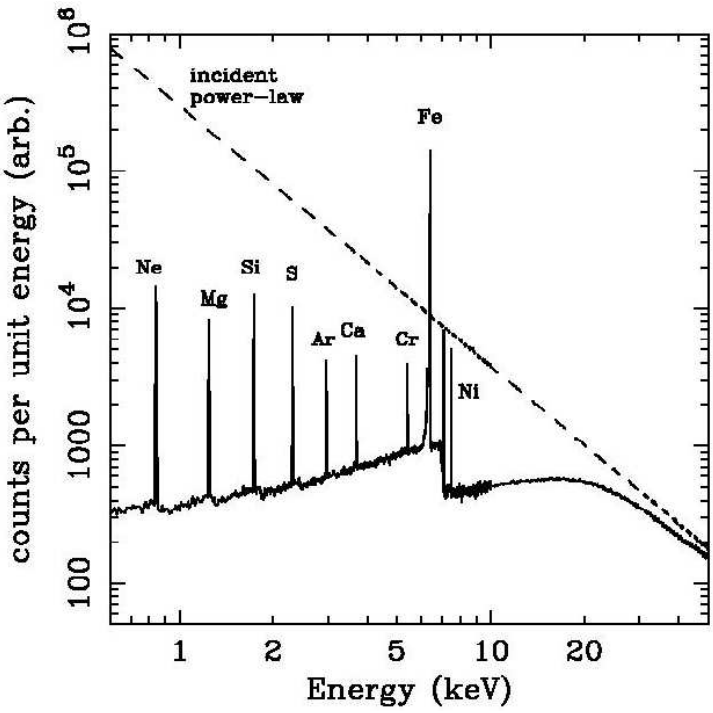

Figure 1.5: Monte Carlo simulations of the X-ray reflection spectrum from a slab of uniform density neutral matter with solar abundances. Dashed line shows the incident power law continuum, while solid line shows the reflected spectrum. Figure taken from Fabian et al. (2000), based on simulations from Reynolds (1996)

.

of the reflection features (Fe K line and Compton hump) in the X-ray spectra of Seyfert galaxies (Matt 1999). These data also confirmed that the power law continuum of Seyfert galaxies cuts off exponentially at energies between 80–300 keV (Perola et al. 2002), a feature first reported in the composite spectra of Seyferts observed by the *Ginga* and *CGRO* (Zdziarski et al. 1995).

All of these various spectral features of the AGN X-ray spectrum are illustrated schematically in Fig. 1.6. The solid red line represents the total spectral model, while the different colors denote the various model components. At low energies there is a soft excess, which is parametrized by a blackbody with temperature of kT = 45 eV, and a warm absorber, which is characterized by absorption edges of O VII (0.739 keV) and O VIII (0.871 keV). The primary power law continuum has a slope of $\Gamma = 2$ and a cutoff energy E_{cut} = 200 keV. The Compton hump at energies between 20–30 keV, an Fe Kα line at 6.4 keV and an Fe K absorption edge at 7.1 keV represent the components of the X-ray reflection spectrum that arises from the reprocessing of the primary power law continuum. It should be noted that this picture is an unabsorbed idealization. In reality, the absorption effect due to our Galaxy, which has a column density of a few times 10^{20} atoms cm^{-2}, modifies the X-ray spectrum below E < 0.6 keV. In the case of an absorbed AGN, the X-ray spectrum is substantially modified by the intrinsic AGN absorption (through the torus).

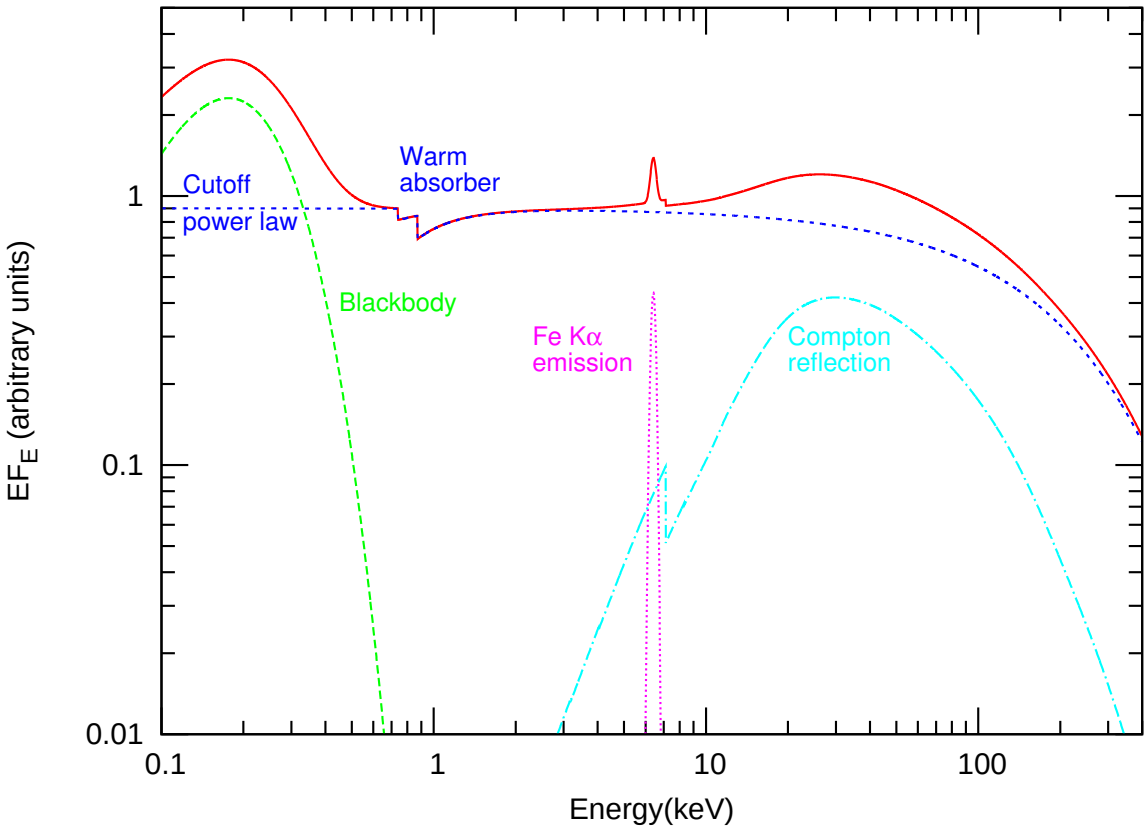

Figure 1.6: A schematic representation of the intrinsic type-1 (unabsorbed) AGN X-ray spectrum in the 0.1–400 keV. The total spectral model is represented by the red solid line, while the individual components that make up the model are shown in different colors. The primary continuum is the power law component with a photon index of $\Gamma = 2$ and a cutoff energy $E_{cut} = 200$ keV. In addition, the continuum consists of a soft-excess below ~0.7 keV (parametrized by a blackbody with temperature of $kT = 45$ eV) and a Compton reflection component at $E \gtrsim 8$ keV. The reflection also gives rise to a neutral Fe Kα line at 6.4 keV. Imprinted on the X-ray spectrum are two absorption edges from O VII (0.739 keV) and O VIII (0.871 keV), that are associated to absorption from an ionized gas along the line of sight, the warm absorber.

1.4 The unified model for AGNs

The unified model of AGNs (Antonucci 1993) has been developed to provide an integrated explanation for the broad range of AGNs properties and types discussed in the previous sections, with as few parameters as possible. The basic principle of the unified model is that the underlying scenario for all AGNs is intrinsically similar and the AGNs diversity is just an orientation effect. A schematic view of our current understanding of the AGN is shown in Fig. 1.7, while the basic AGN components embedded in the host galaxy are represented scaled to physical dimensions in Fig. 1.8.

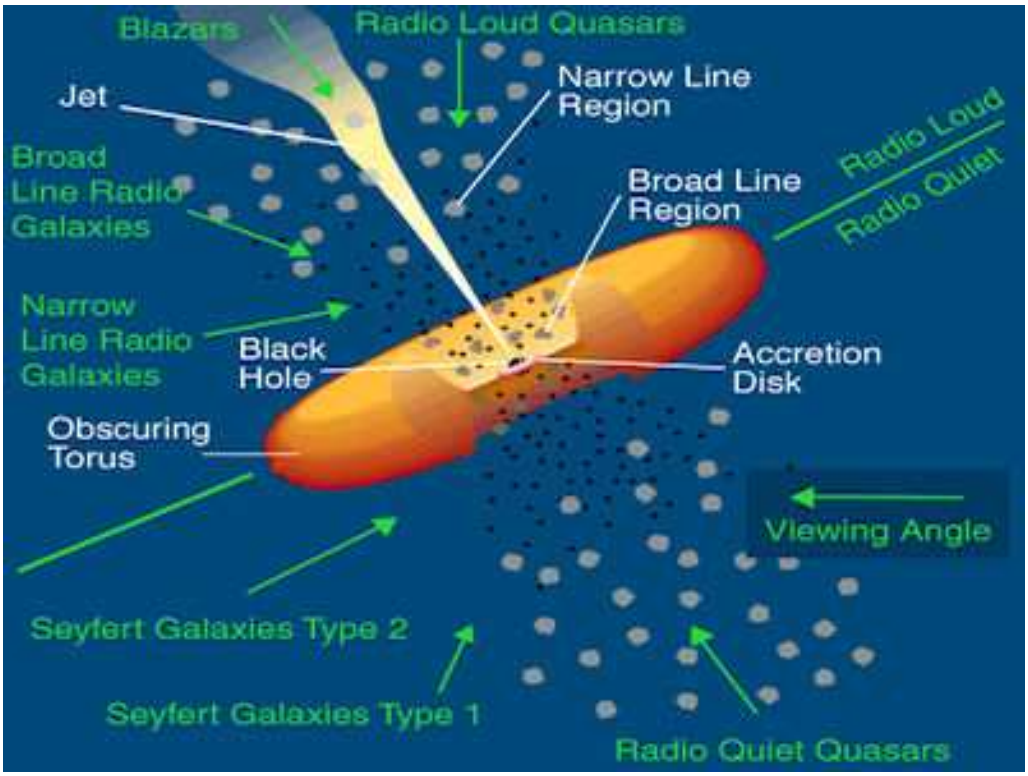

Figure 1.7: Schematic picture illustrating the main components of an AGN as postulated by the unified model (modeled after Urry & Padovani (1995)). The white labels represent the different AGN components. The dark dots represent ionized gas. The green labels note some of the different AGN types and arrows indicate how these different types are named based on the orientation of the obscuring torus or the viewing angle with respect to the observer's line of sight. The viewing angle is a crucial factor in the unified model as it establishes the line of sight towards different parts of the AGN. In Seyfert 1 galaxies, the observer sees the central source more-or-less directly (face-on view), thereby sampling the high velocity BLR clouds and the NLR. In contrast, in Seyfert 2 galaxies, the torus obscures the central source from the observer's line of sight (edge-on view) and only the NLR is seen. The other AGNs types also manifest themselves depending on the viewing angle that enables observations of different parts of AGN.

The model suggests that there is a central supermassive black hole with mass of (10^{6-10} $M_{\odot}$, SMBH), which is surrounded by an accretion disk formed by infalling material. Energy from infalling material heats the accretion disk and the resulting thermal radiation is observed in the optical and UV parts of an AGN's spectrum. The accretion disk is surrounded by the broad-line region (BLR) that produces the strong, broad emission lines. The BLR is characterized by bulk Doppler motions with velocities up to thousands of km s^{-1}, inferred from the width of emission lines such as the Hβ λ4860 or C IV λ1541 in the UV. The BLR has electron densities (determined from the absence of forbidden lines, in particular the [O III] λ4363, that are relatively more prominent in lower density gas) of at least $\sim 10^8$ $cm^{-3}$and temperatures $<10^4$ K.

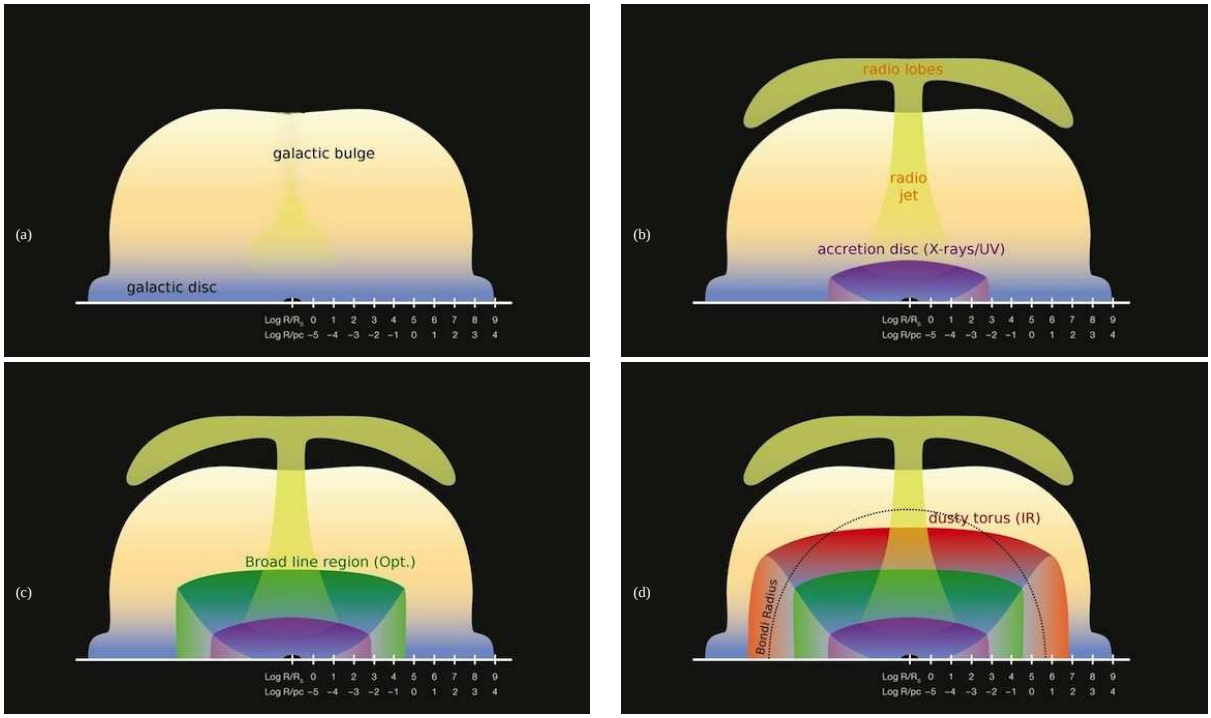

Figure 1.8: A series (in alphabetical order) of schematic, logarithmic views of the basic AGN components embedded in the host galaxy. Scales on the bottom axes are in units of Schwarzschild radii and parsec, and are approximately inferred for a $10^{11} M_{\odot}$ galaxy containing a $10^{8} M_{\odot}$ black hole (courtesy of A. Merloni, S. Bonoli and the ESO graphics department).

The BLR is surrounded by a uniform, optically and geometrically thick toroidal structure that is usually referred as the "obscuring torus" or "dusty torus". The torus is irradiated by the central engine of the AGN. The inner edge of the dusty torus is marked by the dust-sublimation radius, the closest point to the central source where dust grains can survive the strong ultraviolet radiation emitted by AGNs. The irradiated dust produces thermal emission mostly in the infrared region. The presence of parsec-sized obscuring torus has been recently confirmed by mid-infrared observations of the nuclear regions of NGC 1068 (Jaffe et al. 2004) and the Circinus galaxy (Tristram et al. 2007). All these components are embedded in a much larger region, known as the narrow-line region (NLR), which produces the narrow forbidden lines and permitted line cores. The NLR has a cone-shaped geometry because the illuminating radiation from the central engine can only reach the NLR through the openings along the axis of the torus, any gas near the plane of the torus lies in its shadow and will not be illuminated. The NLR has lower gas densities ($\sim 10^{3}$ cm^{-3}) and velocities (300–1000 km s^{-1}) as compared to the BLR. The distance to the NLR from the central source (R_{NLR}) is on the scales of kiloparsecs. The NLR has been resolved in the optical for nearby Seyfert galaxies (e.g. NGC 1068) (see Kraemer & Crenshaw 2000). The last component of the unified model is the presence of relativistic jets emanating from the innermost regions of AGN (~100 Schwarzschild radii). Jets can extend out to several hundred kiloparsecs.

The obscuring torus is a fundamental ingredient in the unified model for AGNs. Its orientation with respect to the observer determines the view along the line of sight to the central region. If we look at the model AGN in Fig. 1.7 from a direction far from the plane of the obscuring torus, we see radiation from the central source and the BLR, as well as the NLR i.e we observe features associated with a Seyfert type 1. On the other hand, if we look at the same model from a direction close to the plane of the torus, we directly see the NLR only. In this case, we will observe features associated with a Seyfert type 2.

The unified model also postulates that the radio-loud and radio-quiet AGNs can be distinguished by considering the orientation of the AGN with respect to the jet location. At an angle far from the jet axis the BLR is hidden and only the NLR is visible and a narrow line radio galaxy will be observed. On the other hand, closer to the jet axis the BLR comes into the view and a broad line radio galaxy is seen. As the angle continues to decrease the intense source of radiation surrounding the black hole comes into view and the object appears as a quasar, with never more than one visible jet[1]. Finally, a blazar is observed when we look face-on at the nucleus and directly into the jet.

The essence of the unified model is that it explains the observed differences between broad (Seyfert 1 like) and narrow (Seyfert 2 like) line active galaxies as obscuration from the torus and viewing angle effects rather than intrinsic physical differences. The unified model also provides a simple AGNs classification scheme, according to which AGNs can be splitted into two broad categories: type 1 (unabsorbed sources) and type 2 (absorbed sources). Both of these types include Seyferts and quasars. Type 1 AGNs exhibit broad and narrow emission lines in their optical spectra, whereas the spectra of type 2 AGNs only show narrow emission lines.

The validity of the unified model has been investigated by several studies conducted over a wide range of wavelengths from radio through X-rays. These studies provide compelling evidence in favor of the unified model. The detection of molecular emission features, notably those due to polycyclic aromatic hydrocarbon (PAH) molecules and strong silicate absorption features around 10 and 18 microns in the Spitzer infrared spectra of numerous type 2 AGNs indicate the presence of an optically thick obscuring structure (Wu et al. 2009b). The most strong evidence supporting the unified model is the presence of broad lines in the polarized spectrum of Seyfert 2 galaxy NGC 1068 (Antonucci & Miller 1985). X-ray observations of nearby Seyfert galaxies observed with *GINGA*, *BeppoSAX* and XMM-*Newton* have revealed that intrinsic X-ray spectral properties (i.e. spectral shapes and luminosities etc.) of Seyfert 1 and 2 are consistent, Seyfert 1 galaxies have lower column densities and Seyfert 2 galaxies have the highest, as expected from the unified model (Awaki et al. 1991; Smith & Done 1996; Bassani et al. 1999; Cappi et al. 2006; Singh et al. 2011).

However, recent studies have discovered that there are significant physical differences between Seyfert 1s and Seyfert 2s. Seyfert 1s with significant absorption (e.g. Fiore et al. 2001) and Seyfert 2s without X-ray absorption (e.g. Pappa et al. 2001; Panessa & Bassani 2002) have been found. Spectropolarimetric surveys find that only ∼30–50% of the Seyfert 2 galaxies show broad lines in their polarized spectra, possibly indicating that not all of these objects have hidden BLRs

[1] Relativistic beaming will cause an approaching jet to be brighter than a receding jet, so as the angle decreases one jet will fade at the expense of the other.

as predicted by the unified model (e.g. Tran 2001, 2003). Moreover, reverberation studies (A technique to measure the size of the BLR by timing the delay between flux variations of the ultraviolet and optical continuum and the response of the broad emission lines. The time delay is due to the light travel time across the BLR.) show that the distance to the BLR (R_{BLR}) in Seyfert galaxies is light days to light weeks from the central ionizing source (Peterson et al. 1998). On the other hand, the BLR in quasars may be up to ten times larger as the size of the BLR is observed to scale with luminosity, $R_{BLR} \propto L^{0.7}$, where L is the X-ray luminosity in the rest-frame 2-10 keV band (Kaspi et al. 2005). A similar anticorrelation between the size and luminosity has been reported for the NLR ($R_{NLR} \propto L_{OIII}^{0.5}$; Bennert et al. 2002).

These observational evidences suggest that the orientation-based unified model can explain the observed AGN phenomena up to the first order. However, it cannot fully account for the diverse and complex behavior exhibited by AGNs.

1.5 Accretion onto a black hole

1.5.1 Basic parameters

An accreting black hole system can be described by two important parameters: the black hole mass (M) and accretion rate ($\dot{M}$). The black hole mass provides a measure of the size scale of the system via the Schwarzschild radius, the radius of the event horizon for a non-rotating black hole,

$$R_S = \frac{2GM}{c^2} \tag{1.1}$$

or the gravitational radius

$$R_g = \frac{GM}{c^2} = \frac{R_S}{2} \tag{1.2}$$

where G is Newton's gravitational constant and c is the speed of light. The Schwarzschild radius for a black hole of 1 $M_\odot$ is 3×10^5 cm.

As the fundamental process at work in an active nucleus is the conversion of the accreted mass to energy, the mass accretion rate determines the total luminosity of the system via the relation

$$L = \frac{dE}{dt} = \frac{d}{dt}\left(\eta m c^2\right) = \eta \dot{M} c^2 \tag{1.3}$$

where E is the energy available from a mass m, $\dot{M} = dm/dt$ is the mass accretion rate and η is the efficiency of converting the rest mass energy of the infalling gas into electromagnetic radiation. The value of the efficiency factor η depends on the details of how accretion actually occurs. However, $\eta = 0.1$ is a reasonable approximation for accretion onto a black hole. Using Eqn. 1.3 with $\eta = 0.1$, we see that an accretion rate of 2 $M_\odot$ yr^{-1} can power a luminous quasar of $L \approx 10^{46}$ erg s^{-1}. It is important to note that every spherically symmetric accreting system has a critical accretion rate, which is defined by the maximum luminosity of the system.

1.5.2 The Eddington limit

Consider spherical accretion of a pure hydrogen gas onto a compact object of mass M. The infalling gas would experience two kinds of forces, one arising from the inward pull of gravity and a second (an outward radiation pressure force) due to Thomson scattering between charged particles in the gas and the photons diffusing outward. The luminosity scale of an accreting system is defined by the balance between these two forces.

Although both electrons and protons are present in the ionized gas[2], the outward radiation force will be dominated by Thomson scattering between the photons and electrons as the Thomson scattering by protons is much less important due to their significantly smaller cross-section[3]. Likewise, the gravitational force dominates for the protons these being the more massive particles.

The radiation pressure force acting on gas particles at a distance r from the central source of luminosity L is given by

$$F_{rad} = \frac{L\sigma_{Te}}{4\pi c r^2} \tag{1.4}$$

where σ_{Te} is the Thomson cross-section for electron scattering. The gravitational force is

$$F_{grav} = -\frac{GM(m_p + m_e)}{r^2} \tag{1.5}$$

where M is the black hole mass, G is the Gravitational constant. The m_p and m_e are the masses of the proton and electron, respectively. For the source to maintain its physical integrity, the outward radiation force on the infalling plasma must be less than the inward gravitational force, so it is required that

$$\frac{L\sigma_{Te}}{4\pi c r^2} \leq \frac{GM(m_p + m_e)}{r^2} \tag{1.6}$$

Since $m_p >> m_e$, putting $m_p + m_e \approx m_p$ in Eqn. 1.6 , we get

$$L \leq \frac{4\pi c G M m_p}{\sigma_{Te}} \tag{1.7}$$

Equation 1.7 is known as the "Eddington limit", and can be used to establish a minimum mass for a source of luminosity L.

The highest luminosity a source of mass M can have and still be stable against the radiation pressure is known as the "Eddington luminosity"

$$L_{Edd} = \frac{4\pi c G M m_p}{\sigma_{Te}} = 1.26 \times 10^{38} \left(\frac{M}{M_\odot}\right) \text{ ergs s}^{-1} \tag{1.8}$$

The Eddington luminosity is an important characteristic luminosity because sources with $L > L_{Edd}$ expel nearby matter and quench the process of accretion. Equation 1.8 shows that the Eddington luminosity of an AGN with black hole mass $M = 10^7 M_\odot$ is $\sim 10^{45}$ erg s^{-1}.

[2] In the case of AGNs, it is reasonable to assume that the matter is completely ionized.

[3] $\frac{\sigma_{Tp}}{\sigma_{Te}} = (\frac{m_e}{m_p})^2 \approx 3 \times 10^{-7}$, where σ_{Tp} and σ_{Te} represent the Thomson cross-sections for proton and electron, respectively.

Given the definition of L_{Edd} and the accretion rate $\dot{M} = L/\eta c^2$, we can define the Eddington accretion rate $\dot{M_{Edd}}$, which is the mass accretion rate necessary to sustain the Eddington luminosity,

$$\dot{M}_{Edd} = \frac{L_{Edd}}{\eta c^2} \simeq 3\left(\frac{M}{10^8 M_\odot}\right)\left(\frac{\eta}{0.1}\right)^{-1} M_\odot \text{ yr}^{-1} \tag{1.9}$$

In the case of spherical accretion, $\dot{M}_{Edd}$ represents a maximum possible accretion rate for the mass M. However, this critical accretion rate can be exceeded if the accretion is assumed to be non spherical, e.g. the mass accretion occurring primarily equatorially in a disk, but the radiation emerging primarily along the disk axis.

1.5.3 Accretion disks

The release of gravitational potential energy by matter falling onto supermassive ($>10^6 M_\odot$) collapsed objects is believed to be the principal source of power generated by AGNs (Salpeter 1964; Lynden-Bell 1969). When matter enters the gravitational potential well of the black hole it likely does so with some angular momentum. Under the attractive power of the black hole's gravity, the infalling material will contract inward. As it contracts, the principle of angular momentum conservation forces it to rotate faster. Material in the equatorial region (i.e. in the plane perpendicular to the rotation axis) moves inward more and more slowly because its rotation starts to balance the pull of gravity. Material above and below the equatorial region falls inward much faster. At some distance from the black hole the centrifugal forces are comparable to the gravitational forces and the matter begins to rotate in circular orbits. The resulting object is a rotationally supported accretion disk.

The detailed structure of the accretion disk depends on a variety of parameters, such as the magnetic field strength and the accretion rate, and the presence or absence of a disk corona or jets. Discussions of the basic structure of AGN accretion disk are given by Blandford (1985) and Begelman (1985) and a complete treatment of the theory of accretion disks is provided by Frank et al. (2002). A few of the basic properties of thin accretion disks that lead to a simple prediction of the emitted spectrum and are not dependent on the viscosity are discussed here.

Consider a black hole accreting through an optically thick and geometrically thin accretion disk. Such a disk would radiate locally like a blackbody (Shakura & Sunyaev 1973). As the matter spirals into the black hole, half of the gravitational potential energy goes into increasing the kinetic energy of the gas, while the other half is radiated away. So, the luminosity of the disk is

$$L = \frac{GM\dot{M}}{2r} = 2\pi r^2 \sigma T^4 \tag{1.10}$$

where T is the temperature at radius r, the σT^4 is the energy radiated per unit area and the factor πr^2 is the area of the disk, and the preceding factor of two accounts for the fact that the disk has two sides. We can rearrange this as

$$T = \left(\frac{GM\dot{M}}{4\pi\sigma r^3}\right)^{1/4} \tag{1.11}$$

It should be noted that this relation, due to Shakura & Sunyaev (1973), does not account for the transport of angular momentum and boundary conditions at the inner edge of the disk. A more correct derivation that takes into account these factors yields,

$$T(r) = \left[\frac{3GM\dot{M}}{8\pi\sigma r^3}\left\{1 - \left(\frac{R_{in}}{r}\right)^{1/2}\right\}\right]^{1/4} \tag{1.12}$$

where R_{in} defines the inner edge of the disk. For $r >> R_{in}$ this can be simplified as

$$T(r) = \left[\frac{3GM\dot{M}}{8\pi\sigma r^3}\right]^{1/4} \tag{1.13}$$

Expressing r in terms of R_S, we obtain

$$T(r) = \left[\frac{3GM\dot{M}}{8\pi\sigma R_S^3}\right]^{1/4}\left(\frac{r}{R_S}\right)^{-3/4} \tag{1.14}$$

Substituting $R_S = 2GM/c^2$, we can write this as

$$T(r) = \left[\frac{3c^6}{64\pi\sigma G^2}\right]^{1/4}\dot{M}^{1/4}M^{-1/2}\left(\frac{r}{R_S}\right)^{-3/4} \tag{1.15}$$

Expressing the accretion rate in normalized units of $\dot{M}/\dot{M}_{Edd}$ (i.e. for a given L/L_{Edd}) yields,

$$T(r) \approx 6.3\times10^5\left(\frac{M}{10^8M_\odot}\right)^{-1/4}\left(\frac{\dot{M}}{\dot{M}_{Edd}}\right)^{1/4}\left(\frac{r}{R_s}\right)^{-3/4} \tag{1.16}$$

For scaling purposes we note that in a thin accretion disk surrounding a $10^8M_\odot$ black hole accreting at the Eddington rate, the temperature is $T(12R_S) \sim 10^5$ K, which corresponds to a photon energy of ~10 eV. This implies that an AGN accretion disk radiates predominantly in the ultraviolet region of the spectrum as observed in the BBB. From Eqn. 1.16, the peak disk temperature scales like $M^{-1/4}$. Accretion disks around massive black holes are therefore expected to be much cooler than the stellar size accretion disks. The peak temperature of the accretion disk surrounding a stellar-mass black hole ($M \sim 1M_\odot$) is ~10^7 K. Such disks emit most of their energy in the X-ray part of the spectrum.

1.5.4 Accretion disk coronae

As discussed in Section 1.3, AGNs exhibit power law components to their spectra which extend to hard X-ray energies with exponential cutoff at high energy ($E \sim 300$ keV). This emission cannot originate from the accretion disk as an AGN accretion disk produces a soft, quasi-thermal spectrum that dominates in the optical/UV region. Yet, the rapid X-ray variability implies an

origin close to the black hole, so the accretion disk must be involved in the production of the X-rays.

A promising mechanism for producing the observed X-ray spectrum is unsaturated inverse Compton scattering. A detailed description of inverse Comptonization can be found in (Rybicki & Lightman 1979; Pozdnyakov et al. 1983; Longair 1992). In this section, we briefly summarize the Comptonization process.

To begin with, we consider Compton scattering, which is the scattering of a photon by a stationary electron. This process takes place in the rest-frame of the electron where the photon looses its energy as it imparts kinetic energy to the recoiling electron. The change in the wavelength of the scattered photon is given by

$$\Delta\lambda = \frac{h}{m_e c}(1 - cos\theta) \tag{1.17}$$

and the change in the energy of the photon is

$$\Delta E = -\frac{E^2}{m_e c^2}(1 - cos\theta) \tag{1.18}$$

where h is the Planck's constant, m_e is the electron mass, θ is the scattering angle of photon and E is the initial energy of the photon. In the laboratory frame, however, the electron can impart energy to the photon, up to $\Delta E = (\gamma - 1)m_e c^2$, where $\gamma = \left(1 - v^2/c^2\right)^{-1/2}$ is the electron's relativistic Lorentz factor.

For a non-relativistic thermal distribution of electrons with temperature T_e, the average photon energy change for a single scattering can be written as

$$\langle \Delta E \rangle = (4kT_e - E)\frac{E}{m_e c^2} \tag{1.19}$$

A photon will gain energy if its energy $E << 4kT_e$, with the fractional energy gain being approximately proportional to γ^2. One factor of γ in this proportionality comes from the boosting of the photon into the electron's initial rest-frame, while the other factor comes from a boosting of the scattered photon back into the lab frame (Rybicki & Lightman 1979; Pozdnyakov et al. 1983). This gain of photon energy is called as inverse Compton scattering.

The process of inverse Compton scattering can occur an arbitrary number of times, as long as the condition $E << 4kT_e$ is fulfilled. From Eqn. 1.19, the energy gained by the photon after each scattering event can be written as $\Delta E/E \approx 4kT_e/m_e c^2$. It can be shown that the average final photon energy, E_f, after N scattering would be

$$E_f \approx E_i exp\left(N\frac{4kT_e}{m_e c^2}\right) \tag{1.20}$$

The number of scatters is usually parametrized in terms of the optical depth τ_{es} of the medium. In this parametrization, the average number of scatters is roughly $\max(\tau_{es}, \tau_{es}^2)$. To simplify Eqn. 1.20, one often defines a parameter, known as the Compton y parameter,

$$y = max(\tau_{es}, \tau_{es}^2)\frac{4kT_e}{m_e c^2} \tag{1.21}$$

such that $E_f \approx E_i exp(y)$. If $y > 1$, the average photon energy increases by an 'amplification factor' $A(y) \approx exp(y)$. If $y >> 1$, the average photon energy reaches the thermal energy of the electrons and photons can no longer gain energy. The former case is referred to as 'unsaturated inverse Comptonization', while the latter case is referred to as saturated Compton scattering. Unsaturated inverse Comptonization is more important for AGN as it is the most viable mechanism for producing the hard X-ray continuum in the broadband spectrum of AGN.

For any accreting compact object, the maximum temperature (assuming standard, geometrically thin, optically thick disk) attained by the system scales with the compact object mass as $M^{-1/4}$. This naturally leads to lower disk temperatures for AGNs as compared to stellar mass black holes systems. For such systems it is therefore more appropriate to define a 'virial temperature', which refers to the average accretion energy per particle. Since, the gravitational energy released per particle of mass m scales as GMm/R, which itself scales as $mc^2/[R/(GM/c^2)]$. Thus, in terms of gravitational radii, the virial temperature is independent of compact object mass. Electron virial temperatures of tens to hundreds of keV ($T_e \sim 10^8 - 10^9$ K) can be readily achieved in the innermost regions of accreting black hole systems. The distribution of these low-to-moderate optical depth and high temperature electrons is thought to create the observed power law spectra of AGNs. For a given Compton y parameter, the photon index of the resulting power law is given by

$$\Gamma = -\frac{1}{2} + \sqrt{\frac{9}{4} + \frac{4}{y}} \tag{1.22}$$

i.e, $\Gamma = 2$ for $y = 1$. Of course, the exact function $\Gamma(y)$ depends on the geometry and other assumptions. A power law form is only achieved for photon energies less than the electron thermal energy. As the energy of the photons become comparable to the electron thermal energy, they no longer gain energy from scattering, and a sharp cutoff is expected in the spectrum at $E_{cut} = 2kT$. Thus, the observed high energy cutoff yields information about the temperature of the underlying electron distribution.

It should be noted that there are two substantial uncertainties in applying the coronal models to observed black hole systems. First, the mechanism to heat the coronal electrons to near virial temperatures and then to re-heat them when they have donated their energy, is currently unknown. Current hypotheses suggest that the process may be similar to solar flares on the sun or heating of the solar corona. Second, the geometry of the corona is also completely unconstrained. Various coronal models with a variety of geometries have been proposed (see Fig. 1.9). The slab or sandwich geometry predicts spectra that are softer than observed, while the other three geometries predict harder spectra. The spectral softening/hardening is caused by the efficient/inefficient Compton cooling of the corona.

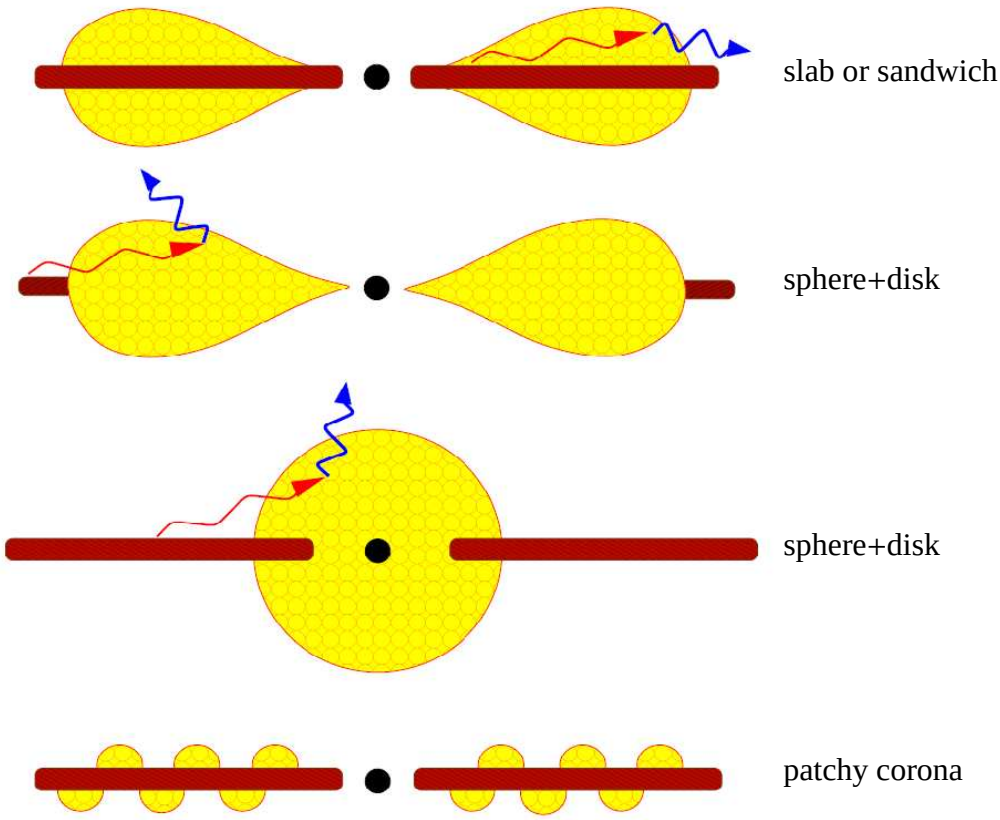

Figure 1.9: Possible geometries for an accretion disk corona. The black labels represent the names of geometries. The slab or sandwich geometry predicts spectra that are softer than observed, while the other three geometries predict harder spectra. The spectral softening/hardening is caused by the efficient/inefficient Compton cooling of the corona. Figure taken from Reynolds & Nowak (2003).

1.6 Iron Kα line

Having discussed that the X-ray spectrum of AGN consists of both direct radiation from the primary X-ray source and 'reflection' from the surrounding accretion flow, we now concentrate on the fluorescent iron line – the most prominent spectral feature imprinted on the X-ray reflection spectrum of AGN.

The fluorescent iron line is produced when one of the two K-shell (i.e. principal quantum number $n = 1$) electrons of an iron atom (or ion) is ejected following photoelectric absorption of an X-ray photon. For this to happen, the incident photon must possess an energy above the photoelectric threshold energy of the K-shell of the iron atom. Following the photoelectric event, the resulting excited state can de-excite in one of the two ways, both of which start with an L-shell ($n = 2$) electron dropping into the K-shell. In the first case, a fluorescent Kα photon of 6.4 keV is radiated. In the second case, the absorption of the fluorescent photon causes further ionization of the iron atom and an electron is ejected. This effect is called autoionization or the

Auger effect and the ejected electron is referred to as the Auger electron. The probability that the photoelectric absorption event is followed by fluorescent line emission is given by the K-shell fluorescence yield, while the probability of the ejection of an Auger electron is given by the K-shell Auger yield.

It is important to note that the K-shell photoelectric threshold energy, the energy of the resultant fluorescent photon and the K-shell fluorescence yield are all functions of the ionization state of the iron. The K-shell photoelectric threshold energy is at an energy of 7.1 keV for Fe I, rising to 7.8 keV for Fe XVIII, and 9.3 keV for Fe XXVI (e.g. Morita & Fujita 1983). The iron Kα fluorescent line energy is a slowly increasing function of the ionization state, rising from 6.4 keV in Fe I to 6.45 keV in Fe XVII, but then increasing steeply with the escalating number of vacancies in the L-shell to 6.7 keV in Fe XXV and 6.9 keV in Fe XXVI (e.g. House 1969; Makishima 1986). The K-shell fluorescence yield is 0.34 for Fe I, rising slowly to 0.49 for Fe XXII (Bambynek et al. 1972). Due to a combination of high fluorescent yield and large cosmic abundance, the iron Kα line is the strongest fluorescent line in the X-ray reflection spectrum[4].

The strength of the iron line is usually measured in terms of its equivalent width (EW) with respect to the direct emission. The EW is the energy (or wavelength) range over which the continuum radiation contains the same flux as the line. Monte Carlo calculations of the X-ray reflection spectra from neutral material have shown that the EW of the iron line is a strong function of the photon index (Γ) of the incident power law and the inclination angle at which the reflecting surface is viewed (George & Fabian 1991). More specifically, the EW of the iron Kα falls with Γ as a result of the decrease in the number of incident photons with energies above the photoelectric threshold energy for higher Γ. The EW varies approximately linearly from ~150 to ~90 eV for Γ = 1.2 to 2.1, respectively. For a given Γ, the EW decreases with the increase in the inclination angle of the reflecting material with respect to the observer. This is a result of the extra absorption and scattering suffered by the iron line photon as it leaves the reflecting surface at an oblique angle.

Considering that the X-ray irradiation can significantly photoionize the surface layers of the accretion disc, the reflection spectra have also been calculated for the ionized accretion disk (Ross & Fabian 1993; Ross et al. 1999). These studies have found that the reflection spectrum and the iron line emerging from an ionized accretion disk are very sensitive to the ionization parameter of the disk, which is given by

$$\xi(r) = 4\pi F_X(r)/n(r) \tag{1.23}$$

where $F_X(r)$ is the X-ray flux received per unit area of the disk at a radius r and $n(r)$ is the comoving electron number density. Reflection spectra from ionized matter for various values of the ionization parameter ξ are displayed in Fig. 1.10. The variation in the iron line energy and strength with the increase in the ξ is clearly evident.

[4] In fact, the Fe Kα fluorescence line consists of two components, Kα_1 at 6.404 keV and Kα_2 at 6.391 keV. However, the energy separation has generally been too small to be detected and a weighted mean at 6.4 keV is generally assumed.

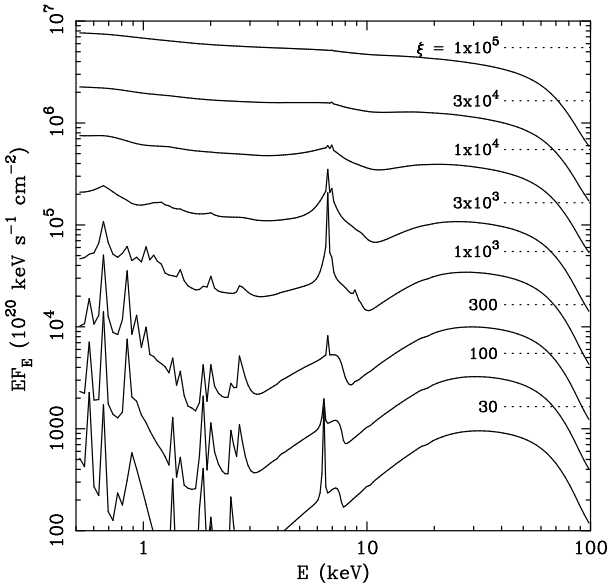

Figure 1.10: Ionized reflection spectra for different ionization parameters ξ. As ξ increases, the elements in the disk become more ionized. When the disk is fully ionized, it does not produce any line features. Relativistic effects close to the black hole have not been included in the calculation of these reflection spectra. Figure taken from Ross et al. (1999).

1.6.1 The iron line profile

The iron Kα line is intrinsically a narrow feature. Hence, the detailed line shape and broadening can be used to study the dynamics of the emitting region. If the reflection spectrum, and the iron line originates from the accretion disk, the line shape is modified by Newtonian, special and general relativistic effects (see e.g. Fabian et al. 2000). A schematic illustration of these effects is shown in Fig. 1.11.

Consider a narrow annulus on a disk at some distance from the central mass. Further assume that this annulus is viewed edge-on, such that one side of the disk approaches the observer, while the other side recedes from the observer. In a non-relativistic accretion disk, a symmetric double-peaked line profile will emerge as the approaching material is shifted to higher energies (blueshifted) and the receding material is shifted to lower energies (redshifted) (*top panel* of Fig. 1.11). The inner regions of the disk, where the material is moving the fastest, produce the broadest parts of the line. Near a black hole, where the orbital velocities of the disk are mildly relativistic, special relativistic effects become considerable (*second panel* of Fig. 1.11). Special relativistic beaming enhances the blue peak of the line with respect to the red one, resulting in an asymmetric profile. In addition, the transverse Doppler effect (i.e "moving clocks run slowly") shifts the entire profile to lower energies. Finally, the gravitational redshifting (i.e. "clocks near black holes run slowly") further shifts the line profile to lower energies (*third panel* of Fig. 1.11). Integrating over all the different annuli on the accretion disk, a broad and skewed line profile is produced (*fourth panel* of Fig. 1.11).

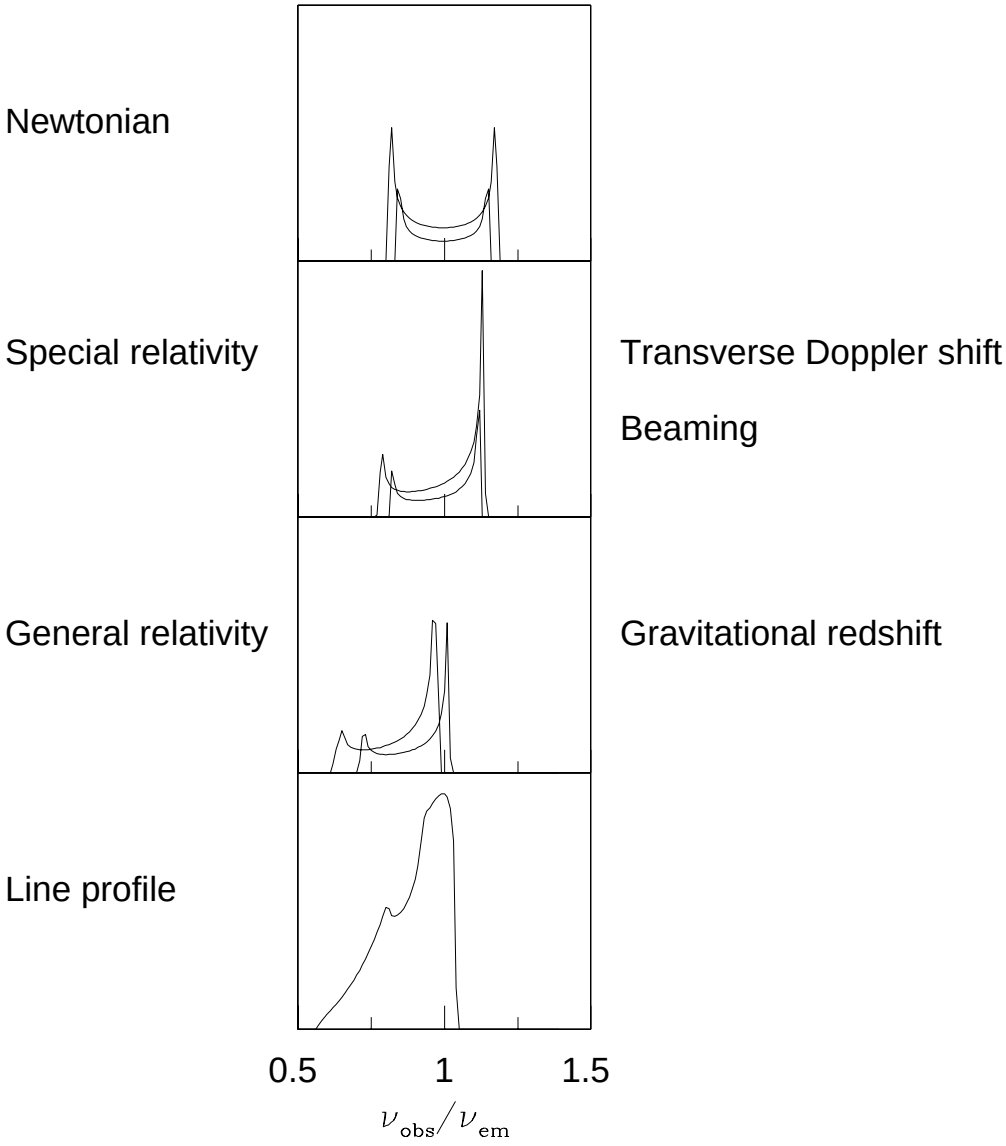

Figure 1.11: Schematic illustration of the iron line shape distortion caused by the interplay of Doppler and transverse Doppler shifts, relativistic beaming, and gravitational redshifting. The *top panel* shows the symmetric double-peaked profile from two annuli on a non-relativistic Newtonian disk. In the *second panel*, the effects of transverse Doppler shifts and of relativistic beaming have been included. In the *third panel*, gravitational redshifting shifts the overall profile to the red side. All these effects give rise to a broad, skewed line profile which is shown in the *last panel*, after integrating over the contributions from all the different annuli on the accretion disk. Figure taken from Fabian et al. (2000).

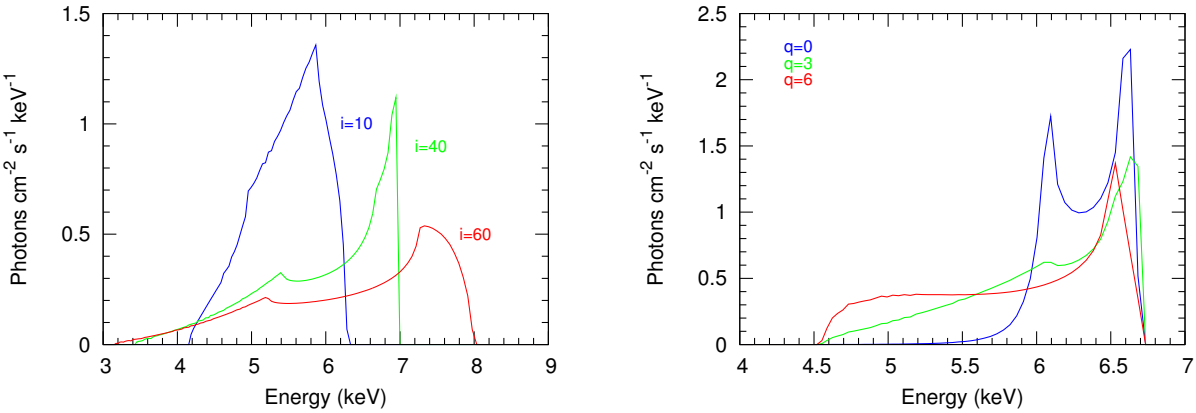

Figure 1.12: *Left panel:* The dependence of the line profile on the observer inclination is shown for an accretion disk around a non-rotating (Schwarzschild) black hole. It is assumed that the fluorescencing region of the accretion disk extends from 6 R_g to 30 R_g. *Right panel:* The dependence of the line profile on the disk emissivity profile is shown. The disk emissivity is assumed to scale as $\epsilon(r) = r^{-q}$. The steepest emissivity ($q = 6$) produces the broadest and most redshifted line profile, because more emphasis is given to the innermost radii, where gravity dominates.

1.6.2 Dependence of the line profile on disk inclination and emissivity

The relativistic line profile exhibits a dependence for many physical parameters. The energy of the blue peak of the line is a strong function of the inclination of the observer line of sight with respect to the accretion disk axis. This is clear in the *left panel* of Fig. 1.12 where we show relativistic line profiles from an accretion disk around a non-rotating (Schwarzschild) black hole. Each line is assumed to be emitted from an annulus of the disk extending between 6 R_g and 30 R_g, where R_g is the gravitational radius. The inclination of the observer line of sight with respect to the accretion disk axis is different for each line. It is seen that the higher the inclination angle, the bluer the line is, providing a robust way to measure the inclination of the accretion disk.

Another important parameter is the form of the emissivity profile, i.e. the efficiency with which the line is emitted as function of the radial position on the disk. As discussed previously, the iron Kα line is assumed to originate through fluorescence of hard photons illuminating the accretion disk. Since these hard photons were produced by Compton upscattering of soft disk photons in the accretion disk corona, the hard photon flux illuminating the accretion disk is in fact proportional to the soft photon flux emitted by the accretion disk. Therefore, the efficiency of the line emission from the accretion disk mainly depends on the illumination profile by the hard X-rays from the corona, which is in turn determined by the energy dissipation on the disk and by the heating events in the corona. The emissivity profile is generally represented by a simple power law $\epsilon(r) = r^{-q}$, where q is the emissivity index. The standard value for the emissivity index is $q = 3$ (e.g. Pringle 1981). In the *right panel* of Fig. 1.12, the dependence of the line profile on the emissivity profile on the disk is illustrated. The cases of a uniform ($q = 0$), standard ($q = 3$) and steep ($q = 6$) emissivity profile are shown. A steep emissivity profile indicates that the conversion of the soft photons to hard photons in the corona is centrally concentrated, thereby

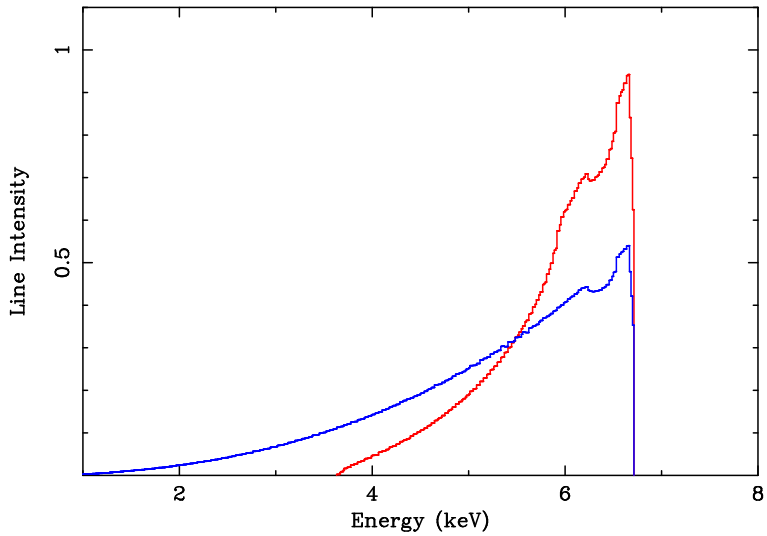

Figure 1.13: The dependence of the line profile on the inner disk radius is shown for the two extremal cases of a Schwarzschild black hole (red) and of a Kerr black hole (blue). Figure taken from Fabian & Miniutti (2005).

irradiating more efficiently the very inner regions of the accretion disk. It is evident from the Figure that steeper emissivity profiles produce much broader and redshifted lines, because more weight is given to the innermost radius, where gravitational redshift dominates.

1.6.3 Dependence of the line profile on the inner disk radius and black hole spin

A key feature of the black hole spacetime is the existence of an innermost radius within which the circular test particle orbits are no longer stable. This radius is known as the innermost stable circular orbit (ISCO), sometimes referred to as the marginally stable orbit (Bardeen et al. 1972). Beyond the ISCO, the test particle will rapidly plunge into the black hole. The region inside the ISCO is therefore called as the plunging region. Considering that the accretion disk is made of gas particles in circular (or nearly circular), orbital motion, the disk can extend down to the ISCO.

The actual radius of the ISCO depends on the black hole spin parameter a/M which can take any value from 0 (Schwarzschild black hole) and 1 (maximally rotating Kerr black hole[5]). The ISCO is located at 6 R_g from the center for a Schwarzschild black hole and at $\simeq 1.24R_g$ for a maximally rotating Kerr black hole, where $R_g = GM/c^2$ is the gravitational radius.

The inner edge of the accretion disk (i.e. the location of the ISCO) strongly affects the shape of the line profile, especially its redward extent. This is shown in Fig. 1.13 where the line profiles for a Schwarzschild (red) and maximally rotating Kerr black hole (blue) are computed. The line is much broader in the Kerr case as compared to the Schwarzschild one. The extra broadening

[5] The maximal value of the spin parameter for the Kerr black hole is likely to be ~0.998 (Thorne 1974).

in the Kerr black hole is caused by stronger relativistic effects (such as gravitational redshift), which act on the line photons emitted from the smaller ISCO.

The above discussion illustrates that the detailed profile of a broad relativistic iron line from the accretion disk carries crucial information on the system inclination, the radial efficiency of the coronal hard X-ray emission and the black hole spin. Moreover, the iron Kα line appears in a relatively unconfused (free from absorption) X-ray spectral region. These factors make this particular emission feature a powerful and remarkable diagnostic tool to probe the dynamics of the innermost accretion flow in accreting black holes.

1.7 Observations of iron lines in AGNs

The first detailed studies of iron lines from AGNs were performed with the Japanese *Ginga* X-ray observatory. These *Ginga* AGN data showed that a significant fraction of all Seyfert galaxies exhibit iron lines (Pounds et al. 1990; Nandra & Pounds 1994). A Compton reflection hump was also detected above the underlying power law continuum. These features were suggested to originate from the circumnuclear optically thick material (i.e the disk and/or the molecular torus) (George & Fabian 1991; Matt et al. 1991).

The shape of the iron Kα line was first resolved with *ASCA* satellite. A broad ($\Delta v \sim 100000$ km s^{-1}) and skewed iron line was first observed in the *ASCA* spectrum of a Seyfert 1 galaxy MCG-6-30-15 (Tanaka et al. 1995). Evidence for similar relativistic iron line profiles in the X-ray spectra of Seyfert galaxies observed by *ASCA* was also found (Nandra et al. 1997). These asymmetric lines were described as originating in the accretion disk. These early detections of relativistic lines from AGNs provided a strong motivation for iron line studies because they were considered as the best evidence for the existence of supermassive black holes in the centers of active galaxies.

The advent of high-sensitivity X-ray satellites XMM-*Newton*, *Chandra* and *Suzaku* has allowed more detailed investigations of this spectral feature and provided important insights into its properties. In particular, the ubiquitous presence of a neutral, narrow ($\sigma \leq 0.1$ keV) iron Kα line in the X-ray spectra of bright Seyfert galaxies has been established (Yaqoob & Padmanabhan 2004; Guainazzi et al. 2006a; Reeves et al. 2006; Nandra et al. 2007). The behavior of the iron Kα line as a function of the X-luminosity has also been examined. The equivalent width of the narrow iron Kα line decreases with the increase in the X-ray luminosity, a trend first discovered by Iwasawa & Taniguchi (1993) using *Ginga* AGN data. This anticorrelation between the iron line equivalent width and the X-ray luminosity was similar to the well-known phenomenon called "UV/optical Baldwin effect" (decrease in the C IV λ1549 equivalent width with increasing UV luminosity). Taking account of the similarity, Iwasawa & Taniguchi (1993) named this inverse relation as the "X-ray Baldwin effect" or "Iwasawa Taniguchi effect" (hereafter IT effect). This trend was confirmed by later *ASCA* observations of broad iron lines (Nandra et al. 1997). In recent years, the existence of the IT effect for the narrow Fe Kα emission lines in the local type 1 AGNs observed by XMM-*Newton* and *Chandra* has been well established (Page et al. 2004; Zhou & Wang 2005; Bianchi et al. 2007; Wu et al. 2009a).

The most fundamental problem, however, is that the physical causes for the "UV/optical Baldwin effect" and "IT effect" still remain unknown. Several models have been proposed to account for these phenomena. Mushotzky & Ferland (1984) suggested that the observed relation is due to a combination of decreasing ionization parameter and covering factor with increasing continuum luminosity. Korista et al. (1998) pointed out that the Baldwin effect is driven by a softening of the ionizing continuum and increasing metallicity towards higher luminosities. Other studies propose that the underlying physical parameters driving the Baldwin effect may be the Eddington ratio (Baskin & Laor 2004; Warner et al. 2004; Dong et al. 2009) and black hole mass (Xu et al. 2008). Nandra et al. (1997) attributed the IT effect to the presence of an ionized skin on the accretion disk, with the degree of ionization increasing with luminosity (Nayakshin 2000a,b).

Another important result from XMM-*Newton*, *Chandra* and *Suzaku* AGNs data is the detection of statistically significant broad iron lines in relatively deep observations. Using a sample of 102 AGNs observed with XMM-*Newton* at $z < 0.5$, Guainazzi et al. (2006a) detected relativistic lines in about 25% of the sample objects ($\simeq$50% when the "well-exposed" spectra with $\gtrsim$10000 net counts in the 2–10 keV band are considered). They also stacked residuals in four equally populated luminosity classes and find that the average EWs are $\lesssim$150 eV for all luminosity classes. Nandra et al. (2007) performed a spectral analysis of a sample of 26 nearby Seyfert galaxies ($z < 0.05$) observed by XMM-*Newton* with a minimum of 30000 net counts in the EPIC-PN spectrum in the 2–10 keV band. They found evidence of broad line emission in around 65% of the sample with a typical EW of $\sim$77 $\pm$ 16 eV, when fitted with a broad Gaussian. de La Calle Pérez et al. (2010) carried out a systematic and uniform analysis of 149 local radio quiet type 1 AGNs and found strong evidence of a relativistic iron Kα line in 36% of the sources, with an average EW of 100 eV (see also Patrick et al. 2010).

The X-ray spectra of distant AGNs are often photon starved. The low photon counting statistics in such AGNs spectra prevents an appropriate modeling of the underlying continuum and therefore the significance of the broad line component and its measured parameters suffer from considerable uncertainties. This problem can be solved by averaging/stacking a number of spectra classified according to their measurable spectral properties, such as the continuum slope, flux and hardness ratio etc. This technique is referred to as the "stacking analysis". The stacking analysis is a powerful technique to improve the counting statistics and to gain an insight into the average properties of faint AGNs.

Streblyanska et al. (2005) derived an average rest-frame spectrum of AGNs detected in a 770 ksec XMM-*Newton* observation of the Lockman Hole field. Using a sample of 104 X-ray sources (53 type 1 and 41 type 2 AGNs and 10 galaxies) covering $0 < z < 4.5$ in redshift space, they report a clear relativistic line in the average rest-frame spectra with an EW of $\sim$560 eV and $\sim$460 eV for the type 1 and type 2 AGNs, respectively. Brusa et al. (2005) studied the average spectra of AGNs detected in the Chandra Deep Field North and South. They used a large sample of 352 spectroscopically identified AGNs and stacked X-ray counts in the observed-frame in seven redshift bins over the range $0.5 < z < 4$. The measured Fe Kα line EWs are consistent with those reported by Streblyanska et al. (2005). However, a broad component was not required by the data. Longinotti et al. (2008) stacked X-ray spectra from a local sample of 157 AGNs and found that the EW of the broad relativistic line is never higher than 100 eV, either when stacking

the whole sample or different sub-samples. Corral et al. (2008) computed the mean Fe emission from a large sample of more than 600 type 1 AGNs spanning a redshift range up to ~3.5. They detected significant unresolved Fe Kα emission line around 6.4 keV with an EW ~ 90 eV and found no compelling evidence of any significant broad relativistic emission line in the average spectrum (see also Mao et al. 2010).

While the presence of a narrow line component is confirmed by all independent analyses, the evidence of the presence of a broad line is more debated. The complex nature of AGNs spectra, and, in particular, the degeneracy between the spectral parameters and the dependence of the line equivalent width and shape over the fitted (absorbed) continuum, hampered so far a comprehensive interpretation of the physics behind the observed features. As an example, it has also been proposed that the observed red-wing can also be ascribed to complex (clumpy) absorption at least for MCG–6-30-15 (Miller et al. 2009). It is therefore critical to have multiple independent stacking procedures to determine the iron line parameters in the average spectrum.

1.8 This thesis

This thesis is aimed at characterizing the properties of the integrated spectrum of AGNs to address the following key points: (i) ubiquity of the iron Kα emission line in distant AGNs, (ii) origin of the IT effect, (iii) evolution of the iron Kα equivalent width with redshift and (iv) mean properties of the iron Kα line in the source rest-frame. In order to address these goals, a large sample of AGNs is required. We use the sample derived from the 2XMM catalog, the second comprehensive catalog of serendipitous X-ray sources from the European Space Agency's (ESA) XMM-*Newton* observatory. We compute the integrated spectrum of AGNs using two approaches: (i) observed-frame stacking and (ii) rest-frame stacking. We also performed simulations to assess the accuracy of the stacking procedure.

Throughout this work a cosmology with $\Omega_m = 0.27$, $\Omega_\Lambda = 0.73$ and $H_0 = 70$ km s^{-1} Mpc^{-1} is used. Spectral analysis was carried out with X-ray spectral fitting package (`XSPEC`, version 12.6.0, Arnaud 1996).

1.9 Outline of the thesis

Chapter 2 briefly summarizes the salient features of the XMM-*Newton* observatory and introduces the 2XMM catalog. It also describes various steps undertaken in the preparation of our final sample together with its main properties.

Chapter 3 is dedicated to addressing the first three main points mentioned above. It details the splitting of our final sample in different redshift and luminosity intervals and outlines the computation and spectral analysis of the integrated spectra in these intervals. In addition, it presents the results of simulations performed to assess the accuracy of the adopted stacking procedure. We note that the work presented in this chapter has been published in Chaudhary et al. (2010).

Chapter 4 characterizes the average iron Kα emission properties of AGNs in the source rest-frame using two different stacking procedures. It also discusses the results of simulations performed to identify the artifacts introduced by the stacking procedure. We note that the work presented in this chapter has been submitted to the Astronomy & Astrophysics journal.

Chapter 5 summarizes the thesis, compiles its main conclusions and discusses future perspectives.

Chapter 2

Sample preparation

An essential requirement to characterize the average X-ray properties of AGNs over a broad redshift and luminosity interval (the aim of this study) is to assemble a large sample of the X-ray selected AGNs. The 2XMM (second comprehensive catalog of serendipitous X-ray sources observed with the XMM-*Newton* observatory) catalog being the largest (until August 2007) catalog of the X-ray sources, comprising a wealth of information on the detected sources, serves as a unique resource for such studies. We therefore exploited the 2XMM catalog for our work.

This chapter is structured as follows: In Section 2.1 we summarize the main characteristics of the XMM-*Newton* observatory. Section 2.2 briefly introduces the 2XMM catalog. In Section 2.3 we describe the safety checks we performed to assess the quality of the archival data products. In the following Section, the selection criteria and the basic properties of our sample are described. The relevant table is presented in the Appendix.

2.1 XMM-*Newton* observatory

The XMM-*Newton* (X-ray Multi-mirror Mission) is a cornerstone mission of the European space agency's Horizon 2000 science program (Jansen et al. 2001; Ness et al. 2010). The primary scientific objective of the XMM-*Newton* is to perform high throughput spectroscopy of cosmic X-ray sources over a broad band of energies ranging from 0.1 to 15 keV. It was launched on December 10, 1999 from Kourou in French Guiana in a highly eccentric 48 hour orbit around the Earth with an apogee of 114000 km and a perigee of 7000 km. It is the largest X-ray satellite ever built in Europe.

The XMM-*Newton* observatory consists of six scientific instruments: three co-aligned X-ray telescopes (XRTs), two reflection grating spectrometers (RGS) and one optical/UV telescope. Each of the three XRTs on-board XMM-*Newton* consists of 58 nested Wolter I mirror shells with a focal length of 7.5 m and is equipped with one European Photon Imaging Camera (EPIC) as focal plane detector. One of the XRTs uses EPIC PN CCD imaging spectrometer (EPIC-PN, Strüder et al. 2001). The EPIC-PN is made up of twelve backside-illuminated CCDs, each of them is organized as a 64×200 matrix of 150 micron-sized pixels. The incoming X-rays are directly focused on to the EPIC-PN. The other two XRTs contain Metal Oxide Semiconductor

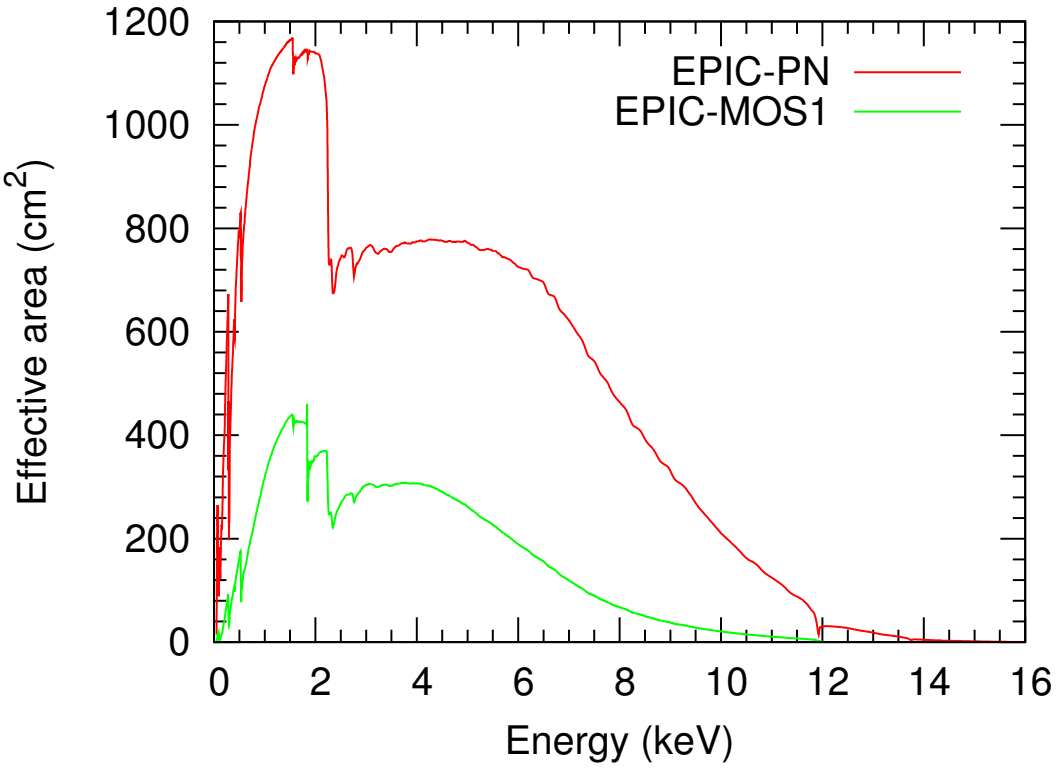

Figure 2.1: On-axis effective area of the EPIC-PN and EPIC-MOS1 cameras on-board XMM-*Newton* .

CCD arrays (EPIC-MOS, Turner et al. 2001) with each EPIC-MOS detector comprising seven front-illuminated CCDs arranged as a 600 × 600 matrix of 40 micron-sized pixels. These XRTs have reflection grating arrays in their light paths, diverting about 50% of the incoming radiation to the reflection grating spectrometers (RGS, den Herder et al. 2001). This design provides high resolution spectroscopy in the 0.33–2.5 keV range. However, due to the light path splitting, approximately 44% of the original flux reaches the EPIC-MOS detectors. This in turn leads to lower effective areas[1] of the two EPIC-MOS cameras as compared to the EPIC-PN detector. The on-axis effective area for the EPIC-PN camera is approximately 1200 cm^2 at 1.5 keV and 600 cm^2 at 8 keV, while corresponding effective areas of the two EPIC-MOS cameras are about 450 cm^2 and 100 cm^2, respectively. The on-axis effective areas of the EPIC-PN and EPIC-MOS1 cameras are displayed in Fig. 2.1.

The energy resolution (i.e the ability to resolve X-ray photons of different energy) for the EPIC-PN is ∼120 eV at 1.5 keV and ∼160 eV at 6 keV, while for the EPIC-MOS detectors it is ∼90 eV and ∼135 eV, respectively. The field of view of the EPIC detectors is approximately circular with a diameter of 30 arcminutes.

The optical/UV telescope (OM, Mason et al. 2001) extends the spectral coverage of the

[1] Mirror effective area, A_e, reflects the ability of the mirror to collect radiation at different photon energies.

XMM-*Newton* observatory into the ultraviolet (UV) and optical range (1800 Å to 6000 Å). It provides monitoring and identification of the optical/UV counterparts of the X-ray sources seen with the XRTs as well as imaging of the surrounding field. All instruments on-board XMM-*Newton* can be operated in a variety of different modes and with several filters.

In a nutshell, wide field of view of the EPIC cameras in combination with high throughput afforded by the heavily nested telescope modules and extended energy range (~0.2–12 keV) of the XMM-*Newton* make it a powerful observatory to perform serendipitous X-ray surveys, providing a significant harvest of serendipitous X-ray sources.

2.2 The 2XMM catalog

The 2XMM is the second comprehensive catalog of serendipitous X-ray sources observed with the XMM-*Newton*[2]. It is constructed by the XMM-*Newton* Survey Science Center (SSC), an international consortium of ten European institutions, led by the University of Leicester, as a formal project activity performed on behalf of ESA. The 2XMM catalog is based on the serendipitous EPIC data from almost 3500 XMM-*Newton* pointed observations made between February 2000 and March 2007 (Watson et al. 2009).

The SSC uses the scientific pipeline (XMM-*Newton* Science Analysis Software, SAS) to process all the XMM-*Newton* data. The data processing is a multi-step process. The schematic flowchart in Fig. 2.2 illustrates the main steps performed in the processing of the EPIC data. To select XMM-*Newton* observations to be used in source detection and source products generation, the data processing system applies several suitability tests on each XMM-*Newton* observation. This includes identification of "useful" exposures[3] based on the minimum duration of the exposure (>1000 seconds), data acquisition mode of the instrument and scientific filter used during the exposure.

Event list[4] processing was performed on all initially selected exposures. The main steps in the event list processing involve examination of CCD event lists on a frame by frame basis, telemetry dropouts corrections, Good-Time-Interval (GTI) list generation for each CCD, flagging of bad frames, identification and flagging of event patterns taking account of the event position (e.g in the vicinity of a bad pixel or CCD edge etc.), identification and removal of events caused by CCD bad pixels as well as cosmic ray events. In addition, the event lists from individual CCD are merged into exposure event lists and the event positions are converted from raw (satellite) coordinates to the detector and sky coordinate systems, yielding calibrated event lists. After identification of the useful period of low background level in each EPIC detector (by removing high flaring background intervals), filtered calibrated event lists are created. High quality images in 5 energy bands spanning a range of 0.2 to 12 keV are generated from these event lists.

Source detection methods are then applied on each image of the five individual bands and of the three cameras. The end product of the EPIC source detection procedure is a combined source

[2] http://xmmssc-www.star.le.ac.uk/Catalogue/2XMM/

[3] Within each observation there are several measurements with different instruments, called exposures.

[4] An event list contains all the events detected in a specific CCD of the EPIC.

list, which, for every detected source lists among other parameters the source identification number, the instrument and energy band where it was detected, the source counts, source position and extent, source flux and count rate as well as hardness ratios. The source extent parameter represented by EP_{EXTENT} is a crucial parameter in the 2XMM catalog because it allows to discriminate the point sources from the extended sources. In the 2XMM catalog point sources are characterized by the $EP_{EXTENT} = 0$. It is worthwhile to point out that the source extent below 6 arcsec is considered as a point source and the extent is re-set to zero.

To identify potential problems associated with the data processing, in particular, the source detection algorithms and parametrization, several automatic and visual screening procedures were applied to the data products. Based on these screening procedures, sources were assigned "automated" and "manual" quality warning flags. These flags provide essential information about the possible problematic issues such as proximity to a bright source, a location within an extended source emission, insufficient detector coverage of the point spread function of the detection etc. Additionally, a summary flag which combines the automated and manual quality warning flags was set for each source. The summary flag, with values in the range 0–4, indicates the overall quality of each detection ordered by increasing severity. A detailed description of the possible values of the summary flag is given in Section 7.5 of Watson et al. (2009).

The output of all data processing steps, briefly outlined above, was thereafter assembled to construct the 2XMM catalog. First, the data of individual detections from the separate observation source lists were combined into a single list of detected objects along with the information about each detection and meta-data relating to the observation in which the detection was made. XMM-*Newton* observations may yield multiple detections of the same source on the sky either because a particular field was the subject of repeated pointings or an interesting object was a target more than once, or because two or more fields happened to overlap. Therefore, in the next step, detections were cross-matched and all detections pertaining to the same celestial source were assigned a unique source number. Key quantities (e.g. co-ordinates, fluxes in various energy bands, detections likelihoods, summary flag, and hardness ratios etc.) for unique sources were determined by combining or averaging the corresponding values from the associated detections. Finally, the data on detections and unique X-ray sources were merged to produce the catalog.

The 2XMM catalog contains 246897 X-ray source detections which relate to 191870 unique X-ray sources, among which 173066 are point sources and 18804 are extended sources. There are 297 columns in the catalog, with the maximum number of columns (223) providing information on the measured parameters of the detections, while the remaining columns yield information on the source identification, coordinates, flags to qualify the detections, variability and unique source parameters. For a complete description of the 2XMM catalog see Watson et al. (2009). We note that incremental versions of the 2XMM catalog produced from the new XMM-*Newton* observations performed after 2007 have now become available.

In summary, the 2XMM catalog is a unique resource for exploring the high-energy properties of various classes of the X-ray emitters such as stars, AGNs and galaxy clusters. When combined with the optical spectroscopic information, the 2XMM catalog offers the opportunity to generate large and well-defined samples of both the bright, local and faint galactic/extragalactic X-ray sources (see e.g. Pineau et al. 2011). These large samples can be used for many specific studies,

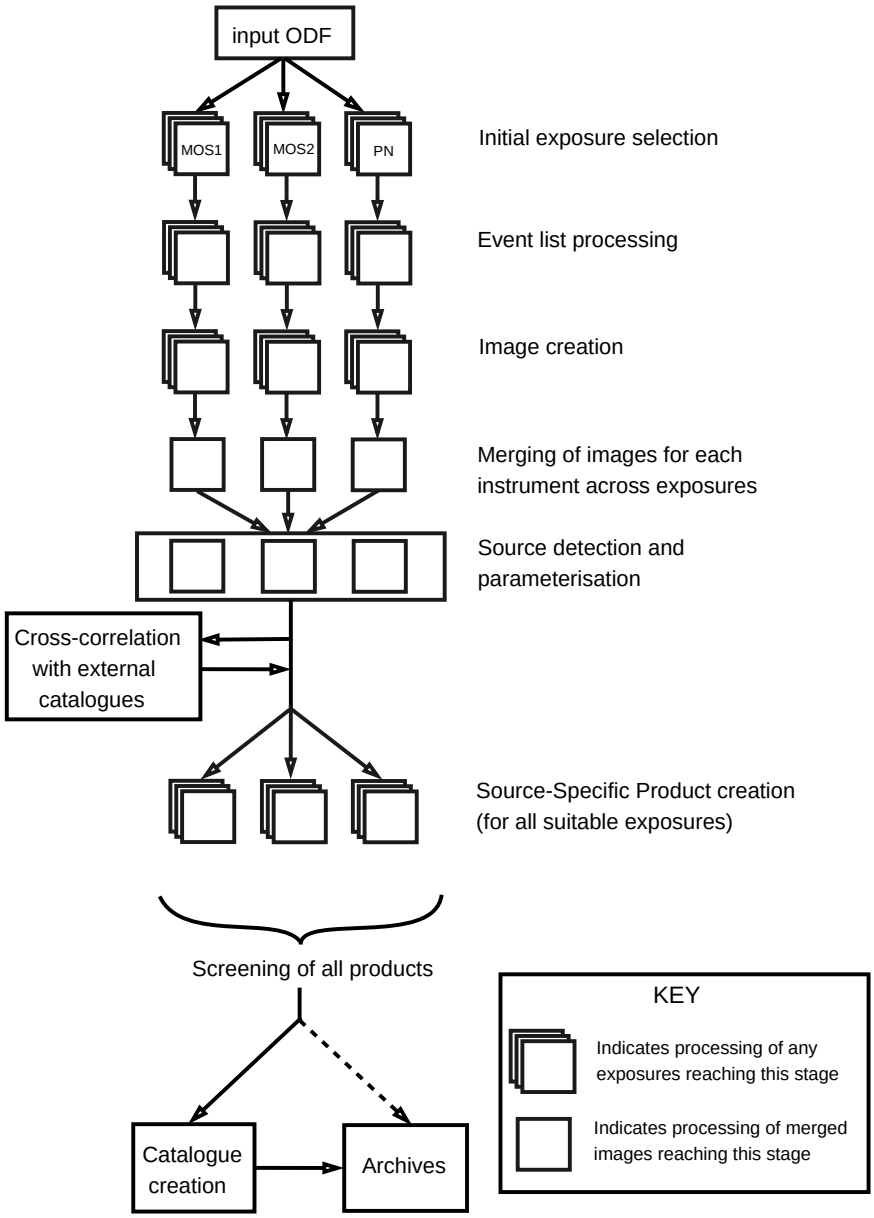

Figure 2.2: A simplified schematic of the data processing steps undertaken in the creation of the 2XMM catalog. Figure taken from Watson et al. (2009).

e.g., the variability analysis of a class of objects, the search for a rare population and characterization of the average properties of a source population etc. Thanks to the broad energy coverage and high effective area of the EPIC cameras on-board XMM-*Newton*, for AGNs studies, the 2XMM catalog provides the best samples.

2.3 Quality evaluation of the archival products

The 2XMM catalog data processing outlined above generates a number of additional data products most notably, time series, source and background spectra, images in the different energy bands and response files etc. for brighter objects with ≥500 net counts and a high detection likelihood ≥15 in the 0.2-12 keV band. These source-specific products are archived at the XMM-*Newton* Science Archive (XSA)[5], which is the repository of all XMM-*Newton* data.

The archival products created from any automated extraction procedure are subjected to limitations, examples being the source products suffering from problems such as low photon statistics, low number of bins, background subtraction problem and contamination of the source extraction region. Keeping in mind these limitations, we examined the quality of the archival products for a dozen of sources. The sources were arbitrarily selected with varying EPIC-PN net counts spanning a range of ∼1500 to 400000 in the 0.2–12 keV band. First, we collected the XMM-*Newton* observation data files (ODF) for these sources. Thereafter, we processed (i.e. performing the data processing steps outlined in Section 2.2) these ODF files using the XMM-*Newton* Science Analysis Software (SAS, ver. 7.1.0) and extracted source, background spectra and response matrices for each source.

We cross-compared these ODF extracted spectra (source and background) with the pipeline processed archival spectra retrieved from the XSA. In Fig. 2.3, the EPIC-PN ODF extracted spectra (red) are over-plotted with the pipeline processed archival spectra (black) for four objects namely NGC 4438 (z = 0.000237 and EPIC-PN net source counts in the 0.2–12 keV ∼1500), NGC3079 (z = 0.003723 and EPIC-PN 0.2–12 keV net source counts ∼1590), NGC 4261 (z = 0.007465 and EPIC-PN 0.2–12 keV net source counts ∼11500) and NGC 1068 (z = 0.003793 and EPIC-PN 0.2–12 keV net source counts ∼400200). The good agreement between the archival products and the extracted spectra for both source and background visible in Fig. 2.3 ensured us the goodness and reliable quality of the archival products, at least for sources with >1000 counts.

2.4 The sample

For our analysis of the properties of integrated spectrum of AGNs we selected 2646 point sources out of the 173066 unique point sources in the 2XMM catalog according to the following selection criteria: (i) high galactic latitude ($|BII| > 25$ degrees) in order to minimize contamination from galactic sources and (ii) sum of the EPIC-PN and EPIC-MOS 0.2–12 keV counts greater than 1000. We cross-correlated the list with the Nasa's Extragalactic Database[6] and obtained redshift information (necessary to derive the rest-frame physical properties) for 919 sources (∼35% of the sample).

For each object, source specific products described in Section 2.3 (i.e. the source and background spectra, images in the different energy bands and response files etc.) were retrieved from the XSA. The summary flags of all the 919 sources were carefully checked. To obtain the clean-

[5] http://xmm.esac.esa.int/xsa/
[6] http://ned.ipac.caltech.edu/

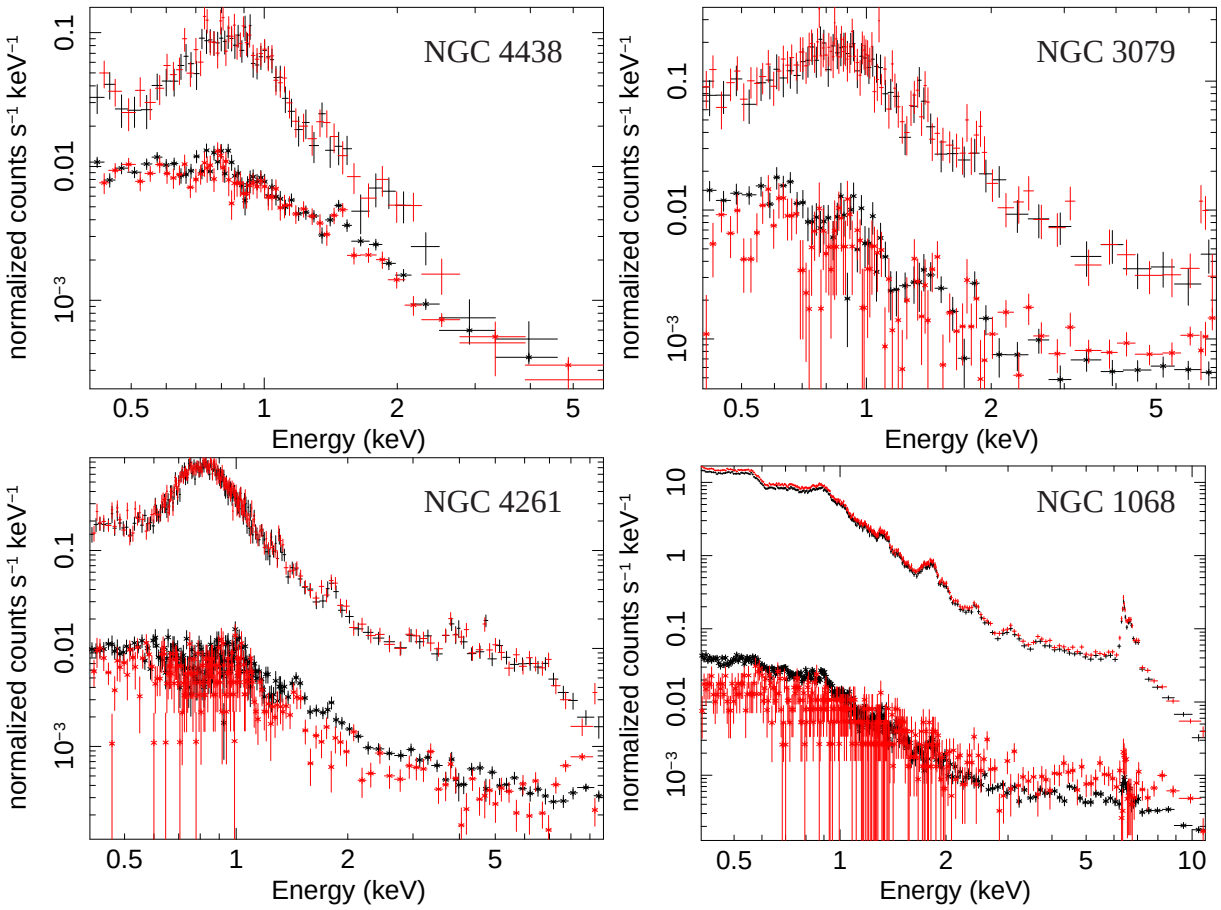

Figure 2.3: Comparison of the EPIC-PN spectra extracted from the raw observation data files (red) with the pipeline processed archival spectra (black) for four listed sources with varying EPIC-PN counts in the 0.2–12 keV band. Corresponding background spectra are also plotted in the respective colors.

est possible sample, we retained the sources with "0" summary flags[7] (i.e. the most reliable) and removed the remaining sources from the sample. We also used optical spectroscopic information for further screening of the sample and excluded all sources classified as HII regions, in groups/clusters and starburst/star forming galaxies (12 sources). In addition, we visually inspected the EPIC-PN images of the sources in order to check if there are additional sources contaminating the background spectrum. In a few images, background annulus was found to have additional sources as shown in Fig. 2.4. We excluded all the archival products of these crowded field images. The final sample consists of 507 point sources.

In the *top panels* of Fig. 2.5, the distributions of the EPIC-PN net counts (*left*) and flux (*right*) in the observed-frame 0.2–12 keV band are compared for the total sample of 2646 point sources selected from the 2XMM catalog (blue), the sample of 919 objects with redshift information available (red) and our final sample of 507 sources (green cross-hatched). It can be seen that the

[7] A source is assigned "0" summary flag when none of the automated or manual quality flags is set to True.

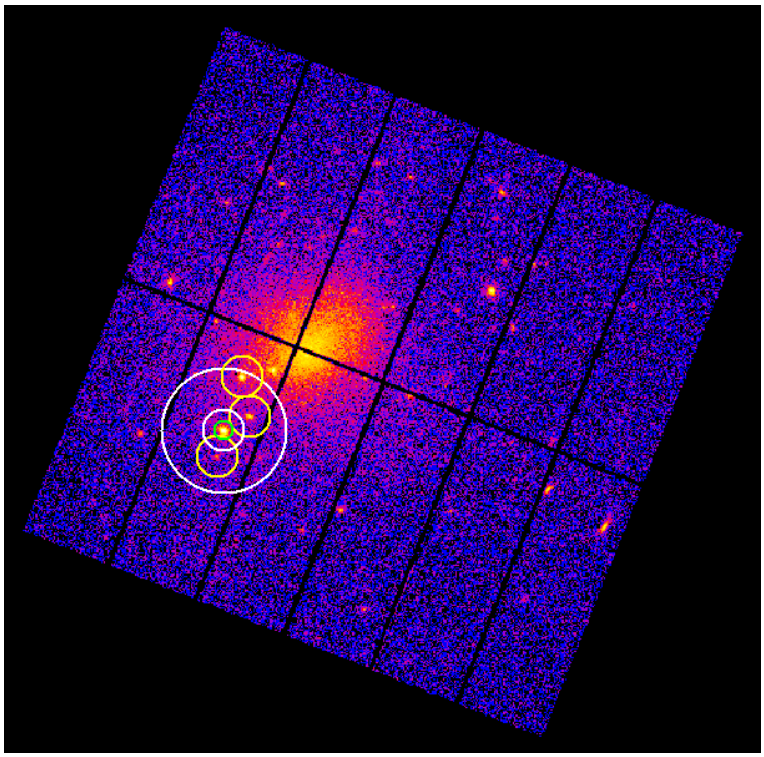

Figure 2.4: An example 2XMM EPIC-PN 0.2–12 keV image in which the background annulus (the region between the two white circles) is contaminated by 3 sources (marked in yellow). The small green circular region represents the main source region. The source and background spectra extracted from such images have not been used in the final sample.

919 sample is a fair representative of the total sample of 2646 objects in terms of the net counts and the flux. The 919 sample has comparatively more bright sources (∼25% of the sources with EPIC-PN net counts >4×10^3), while the 507 sample has only ∼10% sources in this counts range. A similar behavior is observed for the flux distributions. This in turn implies that our sample of 507 AGNs follows a well-defined selection criteria.

In the *bottom panels* of Fig. 2.5, the redshift (*left*) and the X-ray luminosity (*right*) distributions of the sample of 919 sources and of our final sample (507 sources) are over-plotted. We notice that our final sample of 507 sources can be considered a fair representative of the sample of 919 objects in terms of the redshift and X-ray luminosity with a note of the absence of low luminosity objects in the final sample. In the first part of Appendix Table A.3 we report the archival information (e.g. the source name as in the 2XMM catalog, redshift, EPIC-PN net source counts and flux in the observed-frame 0.2–12 keV band) for all the 507 AGNs.

In the following chapters we use this sample of 507 AGNs as a reference sample. However, to fulfill our specific aims, this sample has been further splitted into various sub-samples. We discuss this in the relevant chapters.

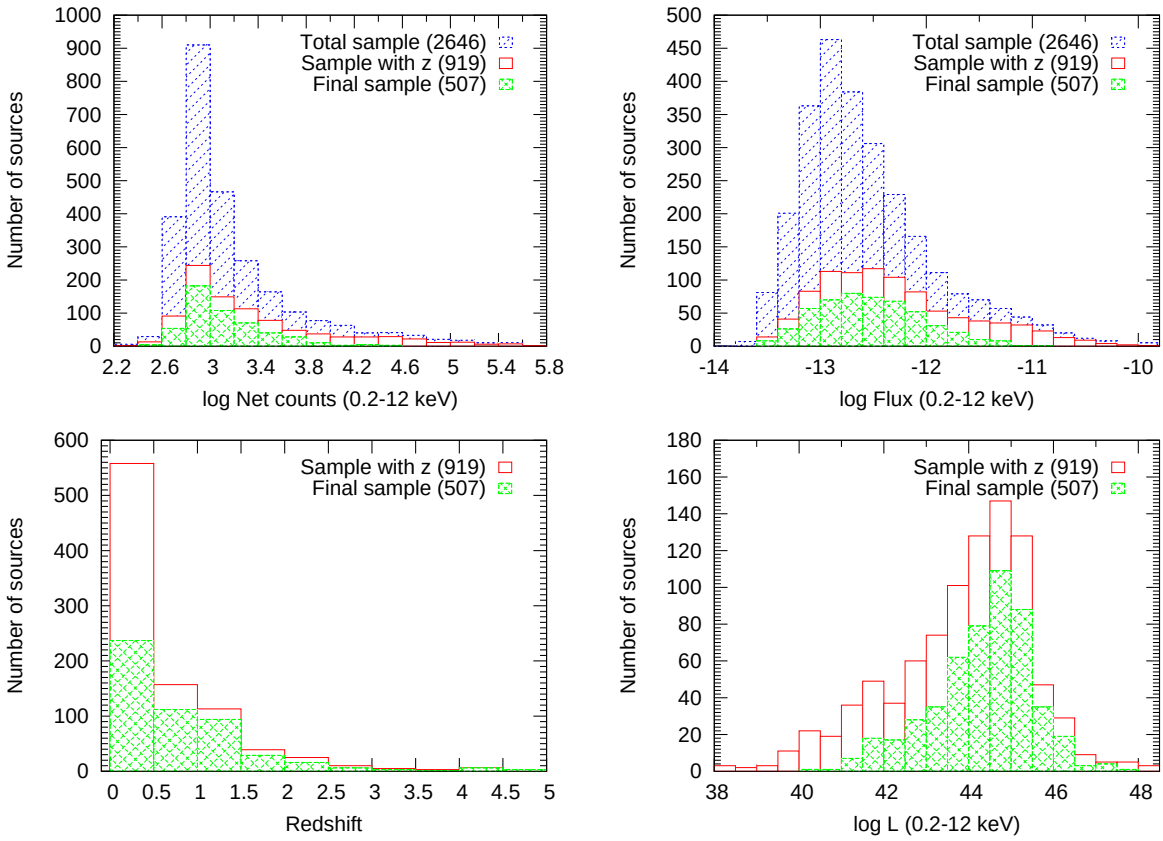

Figure 2.5: *Top panels:* comparison of the distributions of the EPIC-PN net counts (*left*) and flux (*right*) in the observed-frame 0.2–12 keV band for the total sample of 2646 point sources selected from the 2XMM catalog (blue), its sub-sample of 919 objects with redshift available (red) and our final sample of 507 sources (green cross-hatched). *Bottom panels:* the redshift (*left*) and the X-ray luminosity (*right*) distributions of the listed samples.

Chapter 3

Properties of the integrated spectrum of serendipitous 2XMM catalog sources

3.1 Rationale

As outlined extensively in the introduction, active galactic nuclei (AGNs) are believed to be powered by accretion onto supermassive black holes (SMBH) (Salpeter 1964; Lynden-Bell 1969; Rees 1984). Most of the accretion power is released in the innermost region around the central SMBH (Shakura & Sunyaev 1973; Pringle 1981), where the emerging spectrum is significantly affected by strong relativistic effects (Page & Thorne 1974; Cunningham 1975). The iron (Fe) Kα emission line is the most prominent spectral feature observed in the X-ray spectra of AGNs. The line profile serves as a powerful diagnostic tool for probing its origin and provides unique information on the dynamics of the emitting region (Fabian et al. 1989; Laor 1991).

The X-ray spectra of the distant AGNs are often photon starved. The low photon counting statistics in such AGNs spectra is a major constraint in characterizing the line properties, since an accurate modeling of the underlying continuum is essential to measure the line parameters. The stacking analysis, a powerful technique to improve the counting statistics, can be applied to gain an insight into the average properties of the faint AGNs. As discussed previously, several studies have been conducted to characterize the average Fe Kα emission in local and distant AGNs. However, the ubiquity of relativistically broadened Fe Kα emission in AGNs, redshift and luminosity dependence of the Fe Kα line strength are still unclear.

The conventional approach to improve the counting statistics in AGNs involves unfolding the instrumental response by appropriately modeling the continuum and then shifting and adding the individual spectra, which in turn, maximizes the signal-to-noise ratio around the iron line energy. However, the main drawback is a model dependent parametrization of the underlying continuum. We adopt an alternative approach, first implemented by Brusa et al. (2005), in which source spectra are stacked in narrow redshift intervals.

In this chapter we aim at characterizing the properties of the integrated spectrum of the 507 2XMM AGNs described in Section 2.4. These include the ubiquity of the Fe Kα emission in AGNs and the dependence of the spectral parameters on the X-ray luminosity and redshift (points

Table 3.1: Statistics of the sources

Redshift bin	Total sources	PN net counts (2–10 keV)	Total Lbins
0.0–0.2	130	78857	6
0.2–0.3	42	33896	2
0.3–0.4	37	15594	1
0.4–0.6	47	24349	2
0.6–0.8	60	35550	2
0.8–1.0	33	14502	2
1.0–1.3	60	30263	2
1.3–1.7	52	35735	2
1.7–2.1	12	5401	1
2.1–2.5	15	9352	1
2.5–3.0	6	5098	1
3.0–4.0	4	6717	1
4.0–5.0	9	12611	1

(i), (ii) and (iii) in Section 1.8). This chapter is organized as follows: Section 3.2 describes the steps taken for splitting the 507 AGNs sample in redshift and luminosity intervals. Section 3.3 outlines the computation and spectral analysis of the integrated spectrum in each redshift and its associated luminosity bins. Section 3.4 describes the results of simulations performed to assess the accuracy of the adopted stacking procedure. Section 3.5 presents and discusses the results of the spectral analysis. Section 3.6 summarizes the conclusions.

3.2 Splitting the sample in redshift and luminosity bins

First, we grouped the 507 2XMM sources according to their redshifts in 13 redshift bins in the range $0 < z < 5$. The choice of bin sizes is driven by a trade-off between the sum of net counts in each redshift bin and to avoid too wide redshift bin preventing the detection or smearing the narrow line feature. To avoid the contamination of the stacked spectrum by sources covering a too wide range of luminosities in a redshift bin, sources are further splitted into luminosity intervals. The choice of luminosity intervals associated to a redshift bin is driven by the number of sources in that redshift bin. For this reason, sources in all redshift bins at $z > 1.7$ are kept in only one luminosity interval. In all luminosity interval(s) of a redshift bin, the contribution of the single source counts to the total counts (0.2–12 keV) was checked before stacking spectra. The sources with more than 40% contribution were removed from the luminosity interval. The 0.2–12 keV flux (observed-frame) given in the 2XMM catalog was used to calculate the luminosity of the sources. In Table 3.1, we report for each redshift bin: the total number of sources, EPIC-PN counts in the 2–10 keV rest-frame and the total number of luminosity bins in which the sources were further splitted.

3.3 Computation and spectral fitting of the integrated spectrum

Individual source spectra were summed in the observed-frame to compute the integrated spectra in different redshift and luminosity bins over the range $0 < z < 5$. Appropriate background, response and ancillary files were created using the FTOOLS routines `mathpha`, `addrmf` and `addarf`, respectively. The response and ancillary files were weighted for the exposure time. The stacking procedure is described in Appendix Section A.2. We refer to these count-rate averaged X-ray spectra as the "real stacked spectra".

The real stacked spectra were rebinned to have at least 20 counts per bin and analyzed using XSPEC (version 12.6.0; Arnaud 1996). In all redshift and their associated luminosity bins, the real stacked spectra were initially fitted with a single absorbed power law in the rest-frame 2–10 keV band. In about half of the sample we found a significant excess above the power law continuum in the energy range from $6.4/(1 + z_{max})$ to $6.4/(1 + z_{min})$ keV, where z_{min} and z_{max} are the bin boundaries. To investigate the presence of a Fe emission line, we added a narrow redshifted Gaussian component (`mo wabs(pow+zgauss)`) with the line width fixed at $\sigma = 0.1$ keV and the redshift fixed at the median of the bin. We noticed that the fit improved in all luminosity bins, but with varying significance (see Table 3.2). An F-test has been performed to test the significance of the narrow redshifted Gaussian line component. Given the well-known limitations of the F-test in determining the precise significance of a spectral line (see Protassov et al. 2002), we ran simulations in order to quantify the Fe line significance in the real stacked spectra (see Section 3.4).

In all redshift and luminosity bins at $z < 1.7$, the peak energy of the Fe line was allowed to vary, whereas, at $z > 1.7$, the centroid of the Fe line was fixed at 6.4 keV to constrain the fit. Whenever the addition of the line component was not significant (its significance <90% according to an F-test), an estimate of the upper limit to the rest-frame equivalent width (EW) of the neutral Fe emission line was inferred. Errors on the Fe line EW were calculated based on the error in the line normalization considering the 90% confidence interval. The fitting results are summarized in Table 3.2.

Table 3.2 is arranged as follows: Column (1) median redshift of the bin; Col. (2) expected energy of the neutral Fe Kα line; Col. (3) observed-frame bin width at the 6.4 keV position, defined as $\Delta E = 6.4/1 + z_{min} - 6.4/1 + z_{max}$. Comparatively large bin widths in the redshift bin 0.0-0.2 are due to the variation in z_{min} and z_{max} introduced by splitting the sources in different luminosity bins; Col. (4) total number of stacked sources in different luminosity bins in each redshift bin (in parenthesis number of sources with significant Fe Kα line); Col. (5) total net counts in the rest-frame 2–10 keV band; Col. (6) rest-frame X-ray luminosity measured in the 2–10 keV band; Col. (7) power law photon index (Γ) quoted over the 2–10 keV band; errors are reported at the 90% confidence level for one interesting parameter; Col. (8) rest-frame equivalent width of the Fe Kα line; Col. (9) χ^2 and degrees of freedom using a single absorbed power law and a redshifted narrow Gaussian line; Col. (10) χ^2 and degrees of freedom using a single absorbed power law; Col. (11) the F-test probability of the line detection, for F-prob ≤90% the upper limits on the EW are quoted at the 90% confidence level.

3.3.1 Contribution from single sources

In redshift and luminosity bins where a significant Fe Kα line is detected in the real stacked spectrum, we performed spectral analysis of each source spectrum to check for the presence of a significant Fe Kα line. We first grouped each source spectrum to have minimum 20 counts per bin. As our main interest is to identify spectra with significant Fe Kα line, we restricted our spectral analysis in the 2–10 keV rest-frame energy range. For simplicity we adopt the same continuum model for all spectra as for the real stacked spectrum. We then added a narrow (σ = 0.1keV) redshifted Gaussian line with the redshift fixed for each source. We performed an F-test to quantify the significance of the Fe Kα line in each spectrum. We considered significant Fe Kα detection in the spectrum if the F-prob of the line detection was $\geq$90%. The number of sources found to have significant Fe Kα line are quoted in parenthesis in Table 3.2.

We then investigated the Fe Kα contribution from spectra with and without significant Fe Kα lines by creating stacked spectra of both subsamples. These stacked spectra were analyzed with the same models as that used for the real stacked spectra and fit parameters were derived. The stacked spectra of sources without significant Fe Kα line detection show the presence of Fe Kα line with varying significance depending on the redshift and luminosity bin. Typical Fe Kα EWs of these spectra span a range from $\sim$200 eV in the lowest redshift bin to $\sim$100 eV in the redshift bin 0.6–0.8. In the *top panels* of Figs. 3.1 and 3.2, we show spectral fits with respect to a single absorbed power law to three stacked spectra, from *top* to *bottom*, sources with significant Fe Kα line detection, real stacked spectra and sources with undetected Fe Kα line. In the *bottom panels* Data/Model ratios are shown for the real stacked spectra.

Table 3.2: Results of spectral fitting in different redshift bins.

z_{median} (1)	E(Kα) (keV) (2)	Binwidth (keV) (3)	Total sources (4)	Spectral counts (5)	log L_X(2–10 keV) erg s^{-1} (6)	Γ (7)	Eqw (eV) (8)	χ^2/dof wabs(pow+zgauss) (9)	χ^2/dof wabs(pow) (10)	F-prob (11)
zbin: 0.0–0.2										
0.02	6.26	0.21	20(8)	10440	$41.58^{+0.05}_{-0.11}$	$0.93^{+0.08}_{-0.07}$	398^{+54}_{-53}	491.9/435	642.5/437	>99.999
0.03	6.22	0.28	20(9)	8421	$41.81^{+0.04}_{-0.14}$	$1.04^{+0.06}_{-0.05}$	455^{+65}_{-66}	420.8/351	544.9/353	>99.999
0.06	6.01	0.83	23(4)	9433	$42.43^{+0.05}_{-0.12}$	$1.06^{+0.09}_{-0.08}$	163^{+54}_{-52}	373.4/385	399.3/387	>99.999
0.09	5.89	0.81	21(6)	13986	$42.83^{+0.05}_{-0.10}$	$1.52^{+0.10}_{-0.09}$	105^{+66}_{-31}	508.9/518	527.7/520	99.991
0.12	5.71	0.75	22(3)	11932	$43.28^{+0.05}_{-0.09}$	$1.20^{+0.08}_{-0.08}$	105^{+45}_{-46}	474.1/472	488.3/474	99.906
0.16	5.51	0.67	24(6)	24645	$43.94^{+0.03}_{-0.06}$	$1.37^{+0.05}_{-0.04}$	75^{+30}_{-29}	712.9/737	729.3/739	99.976
zbin: 0.2–0.3										
0.25	5.12	0.32	21(2)	6415	$43.14^{+0.05}_{-0.31}$	$1.88^{+0.12}_{-0.07}$	201^{+110}_{-109}	259.5/260	268.3/262	98.717
0.24	5.14	0.34	21(2)	27481	$44.18^{+0.03}_{-0.06}$	$1.72^{+0.03}_{-0.02}$	79^{+31}_{-30}	728.8/708	746.2/710	99.976
zbin: 0.3–0.4										
0.34	4.79	0.34	37(5)	15594	$43.76^{+0.03}_{-0.09}$	$1.82^{+0.05}_{-0.03}$	69^{+49}_{-49}	439.6/477	444.8/479	94.026
zbin: 0.4–0.6										
0.47	4.37	0.54	23(2)	7099	$43.59^{+0.04}_{-0.17}$	$1.71^{+0.08}_{-0.06}$	144^{+95}_{-93}	281.5/274	287.7/276	94.933
0.51	4.24	0.48	24	17250	$44.41^{+0.04}_{-0.06}$	$1.74^{+0.04}_{-0.06}$	<98	475.3/485	479.4/487	87.255
zbin: 0.6–0.8										
0.68	3.80	0.40	30(4)	9296	$43.88^{+0.04}_{-0.13}$	$1.90^{+0.07}_{-0.07}$	163^{+87}_{-96}	297.8/330	305.7/332	98.672
0.68	3.81	0.40	30(3)	26254	$44.67^{+0.02}_{-0.05}$	$1.83^{+0.03}_{-0.03}$	93^{+39}_{-39}	602.3/561	616.9/563	99.881
zbin: 0.8–1.0										
0.89	3.39	0.33	17	7142	$44.17^{+0.03}_{-0.12}$	$1.90^{+0.09}_{-0.07}$	<223	254.1/262	258.4/264	88.928
0.91	3.36	0.32	16	7360	$44.69^{+0.03}_{-0.10}$	$1.88^{+0.06}_{-0.06}$	<135	263.8/264	265.1/266	47.559
zbin: 1.0–1.3										
1.16	2.97	0.38	30	12833	$44.45^{+0.02}_{-0.08}$	$2.06^{+0.08}_{-0.05}$	<183	325.9/354	329.8/356	88.076
1.18	2.94	0.36	30	17430	$45.02^{+0.02}_{-0.05}$	$1.85^{+0.05}_{-0.04}$	<51	423.0/417	423.0/418	5.595
zbin: 1.3–1.7										
1.44	2.63	0.38	27	12255	$44.51^{+0.04}_{-0.07}$	$1.99^{+0.13}_{-0.10}$	<174	358.9/352	361.5/354	71.753
1.46	2.60	0.38	25	23180	$45.31^{+0.02}_{-0.04}$	$1.89^{+0.07}_{-0.04}$	<110	468.6/441	473.4/443	89.606
zbin: 1.7–2.1										
1.89	2.22	0.23	12	5401	$45.03^{+0.04}_{-0.10}$	$1.69^{+0.17}_{-0.08}$	<193	199.1/200	201.9/201	90.608
zbin: 2.1–2.5										
2.22	1.99	0.18	15	9352	$45.38^{+0.04}_{-0.05}$	$1.92^{+0.14}_{-0.12}$	<48	291.2/279	291.2/280	0.000
zbin: 2.5–3.0										
2.88	1.65	0.16	6	5098	$45.56^{+0.04}_{-0.06}$	$2.00^{+0.20}_{-0.13}$	<115	177.5/190	178.0/191	50.559
zbin: 3.0–4.0										
3.31	1.49	0.25	4	6717	$46.18^{+0.04}_{-0.05}$	$1.66^{+0.16}_{-0.14}$	<106	224.9/222	225.6/223	59.089
zbin: 4.0–5.0										
4.31	1.21	0.14	9	12611	$46.32^{+0.03}_{-0.03}$	$1.76^{+0.13}_{-0.11}$	<83	275.2/284	276.5/285	74.598

See Section 3.3 for description of the columns.

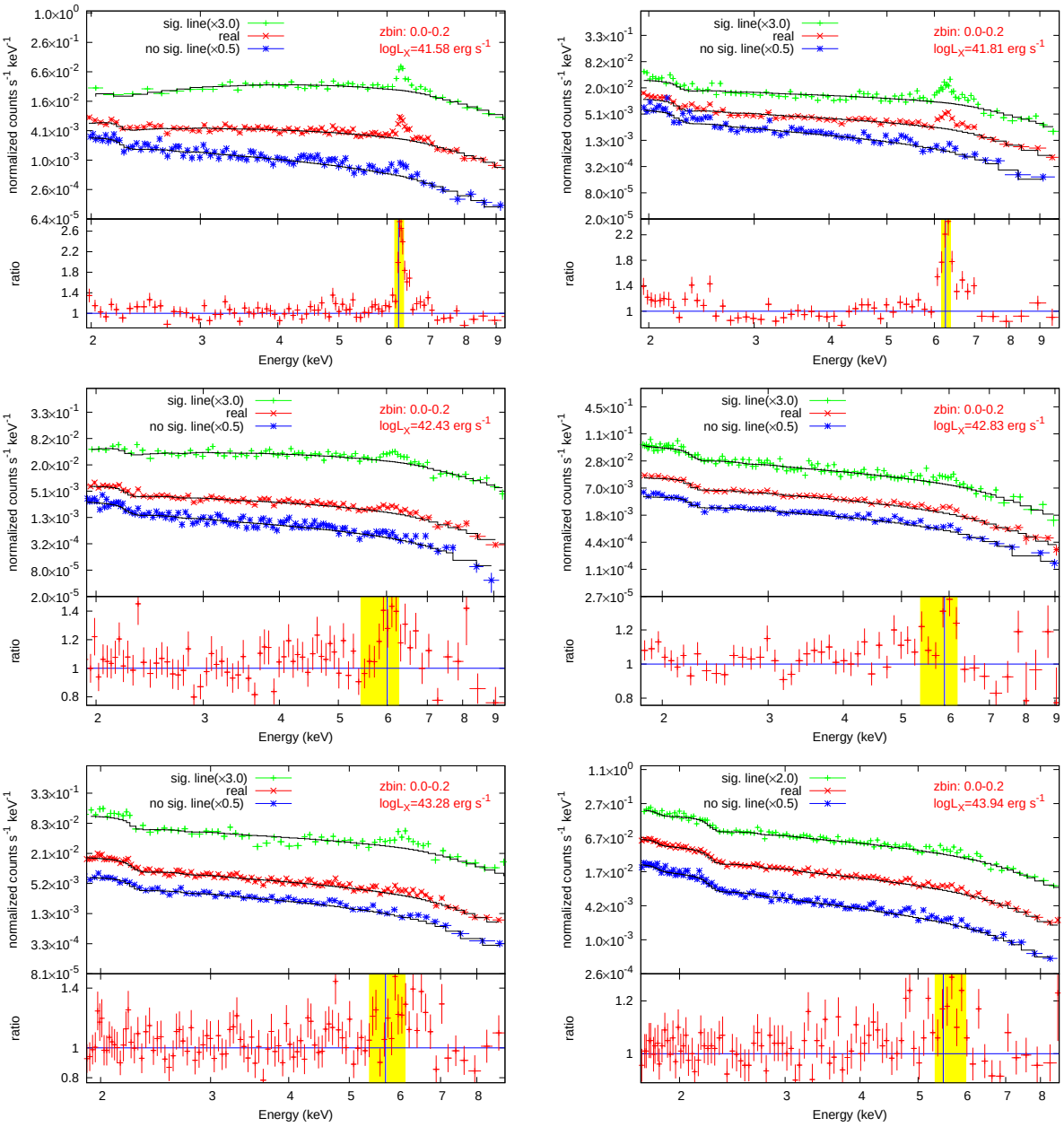

Figure 3.1: *Top panels* in each figure show spectral fits (`mo wabs(pow)`) to three stacked spectra in the quoted redshift bin, from *top* to *bottom*, sources with significant Fe Kα line detection, real stacked spectra and sources with undetected Fe Kα line. For visual clarity, the stacked spectra of sources with and without significant Fe Kα line detection have been rescaled by the factor listed in parenthesis. In the *bottom panels* Data/Model ratios are shown for the real stacked spectra. The vertical line is drawn at the expected position for the redshifted 6.4 keV Fe Kα line, while the shaded region encompasses the bin width reported in Table 2. The average rest-frame luminosities (2–10 keV) obtained for the best fit model (a single absorbed power law and a narrow redshifted Gaussian line) are also quoted for the real stacked spectra.

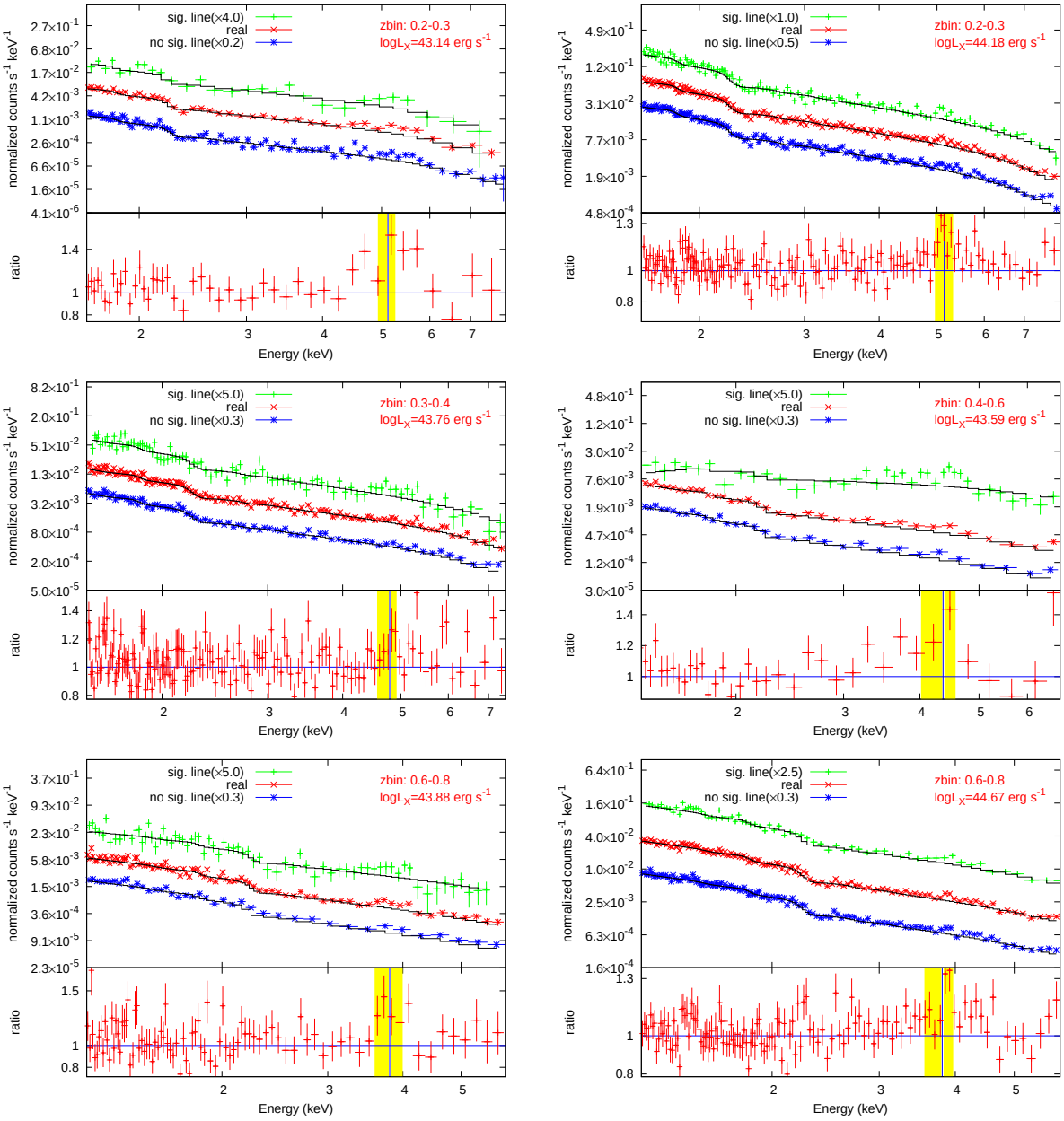

Figure 3.2: Representation of the data in this figure is the same as in Figure 3.1.

3.4 Simulations

We performed extensive simulations to assess the accuracy of the stacking procedure. We created "simulated stacked spectra" in redshift and luminosity bins where a significant narrow Fe Kα line (the F-prob of the line detection >90%) is detected in the real stacked spectrum (see Table 3.2). These include six luminosity bins in the redshift bin 0.0–0.2, two luminosity bins in the redshift

bin 0.2–0.3, one luminosity bin in the redshift bin 0.3–0.4, one luminosity bin in the redshift bin 0.4–0.6 and two luminosity bins in the redshift bin 0.6–0.8.

As detailed in Section 3.3.1, in each of these bins, we identified sources with and without significant Fe Kα line by analyzing each source spectrum in the rest-frame 2–10 keV band. We also constructed the stacked spectra of these two source types. To create the simulated stacked spectrum we considered separately the contribution from sources with and without significant Fe Kα line. For the sources with significant Fe Kα line, the best fit parameters retrieved from the individual spectral analysis were given as input parameters. For the sources with undetected Fe Kα line, the average values measured from their stacked spectrum (blue spectrum in Figs. 3.1 and 3.2) were used as input parameters. We produced 1000 simulated stacked spectra in all the above mentioned redshift and luminosity bins. Identical response and effective area files were used for the real and simulated stacked spectra.

In Fig. 3.3, the spectral profiles of the simulated (black) and real (red) stacked spectrum are compared in the six luminosity bins in the redshift interval 0.0–0.2. A similar comparison in the other selected redshifts and luminosity intervals is shown in Fig. 3.4. In all cases, a very good agreement between both the spectral profiles is clearly evident.

All the simulated stacked spectra were analyzed in `XSPEC` using a model consisting of an absorbed power law and a redshifted Gaussian line (`mo wabs(pow+zgauss)`). The line width was fixed to 0.1 keV, while the redshift was fixed to the median redshift of the bin. The other fit parameters were allowed to vary. Thereafter, histograms of the spectral fit parameters (e.g. the power law photon index, the X-ray luminosity and the Fe Kα line EW etc.) were produced and fitted with a Gaussian function to derive the mean and standard deviations of their distributions.

In Fig. 3.5, histograms of the simulated stacked spectrum fit parameters overlaid with the fitted Gaussian function are shown in the six luminosity bins in the redshift range 0.0–0.2. The *left panels* in each row display the power law photon index distributions, while the *central panels* are the X-ray luminosity distributions and the *right panels* show the narrow Fe Kα line equivalent width (EW) distributions. A similar set of histograms in the other selected redshifts and luminosity intervals is plotted in Fig. 3.6.

Finally, we compared the spectral parameters of the simulated stacked spectra with those measured from the real stacked spectra. Figure 3.7 illustrates the comparison of the power law photon indices, whereas Figs. 3.8 and 3.9 show the comparisons of the 2–10 keV X-ray luminosities and the narrow Fe Kα line EWs, respectively. In each figure, the red point represents the measurement from the real stacked spectrum and the black point denotes the value from the simulated stacked spectrum. We observe that, in all cases, the parameters of the simulated stacked spectra are statistically consistent with those obtained from the real stacked spectra. This in turn quantifies that the fit parameters derived from the spectral analysis of the real stacked spectrum represent the average of the parameters of the individual spectra comprising the real stacked spectrum, thereby attesting the accuracy of our stacking procedure.

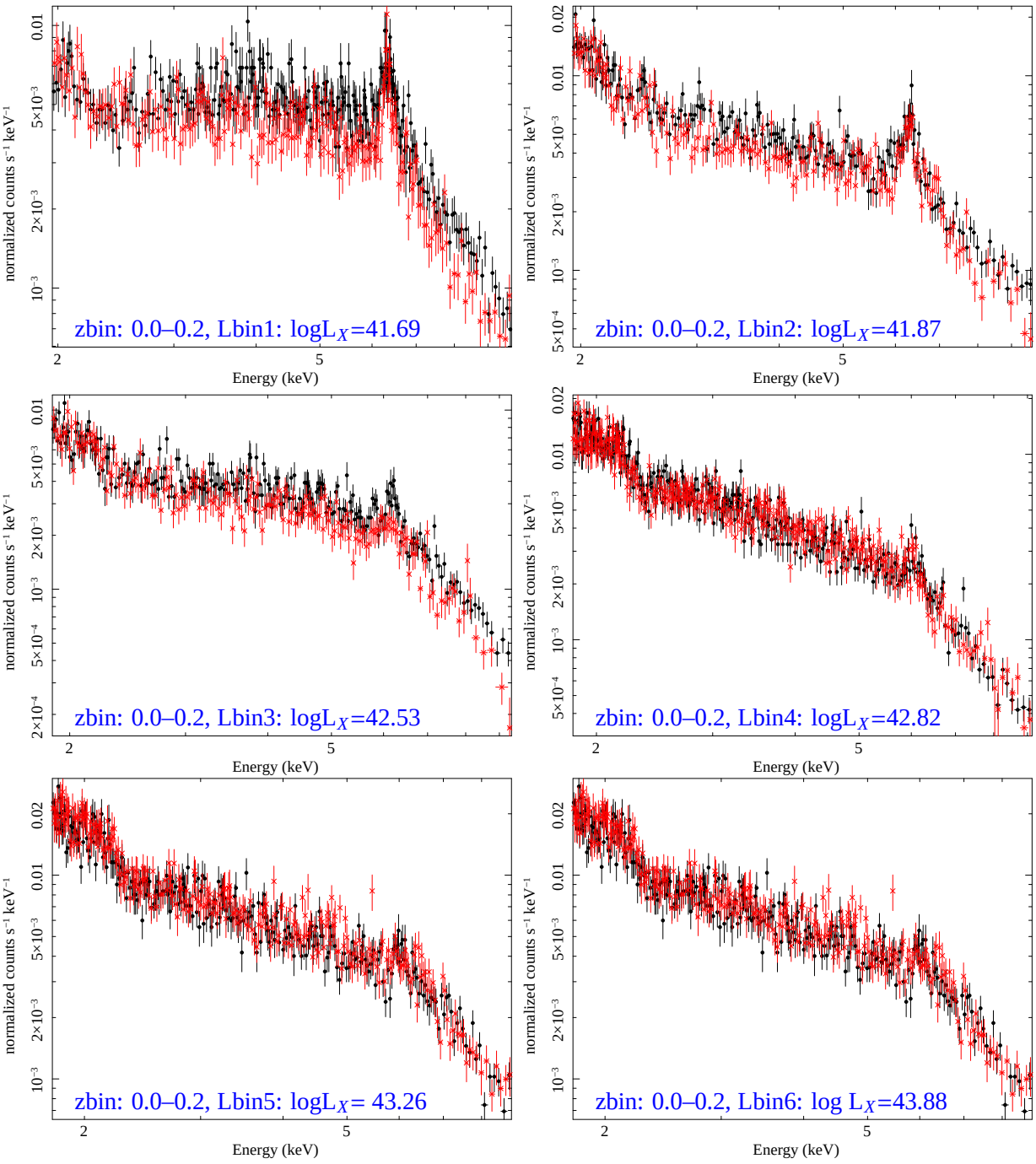

Figure 3.3: Comparison of one simulated stacked spectrum (black) with the real stacked spectrum (red) in the six quoted luminosity bins in the redshift bin 0.0-0.2. The average 2–10 keV X-ray luminosity obtained from the spectral analysis of the simulated stacked spectrum is also reported.

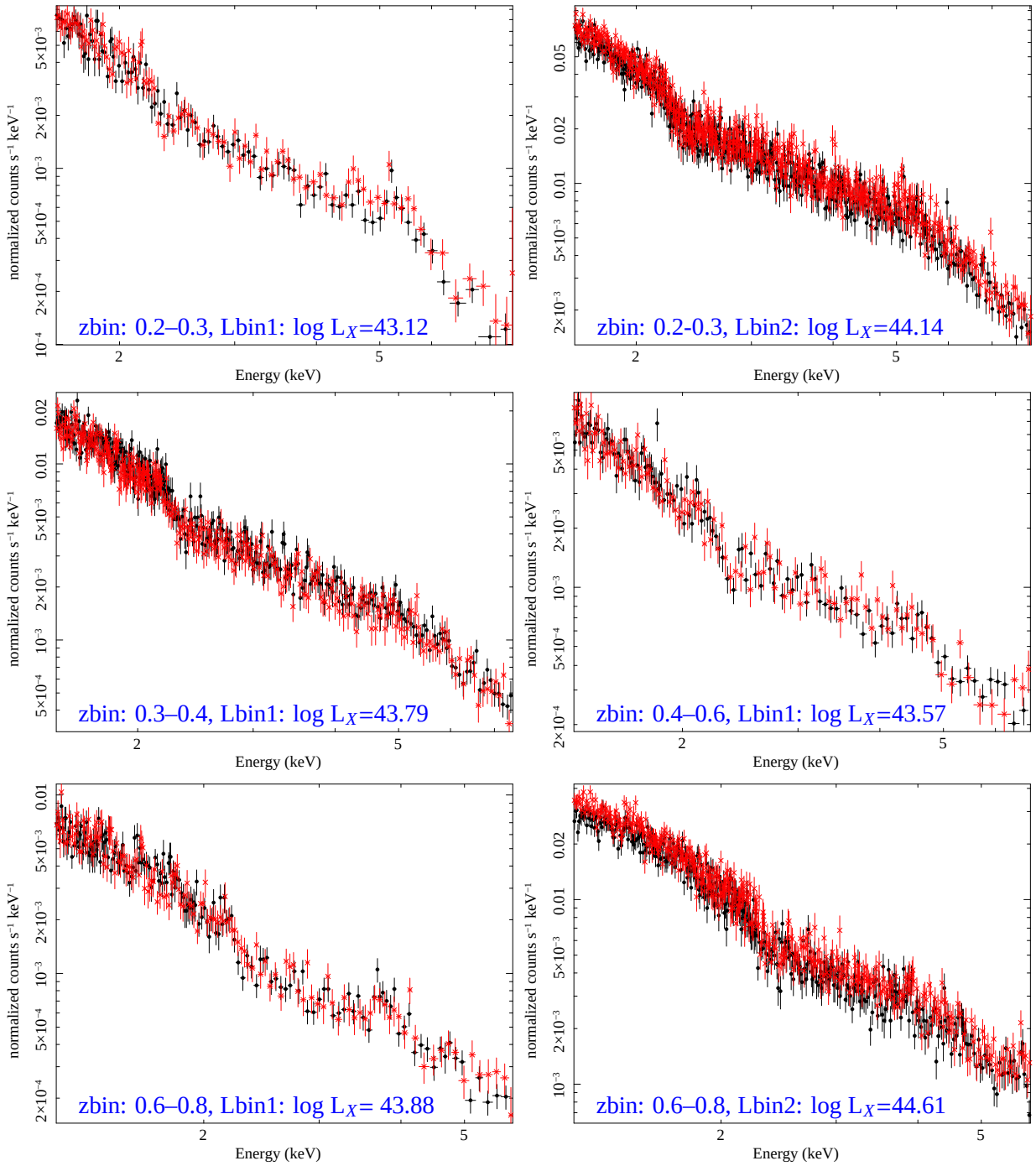

Figure 3.4: Comparison of one simulated stacked spectrum (black) with the real stacked spectrum (red) in the quoted redshift bins. The average 2–10 keV X-ray luminosity obtained from the spectral analysis of the simulated stacked spectrum is also reported.

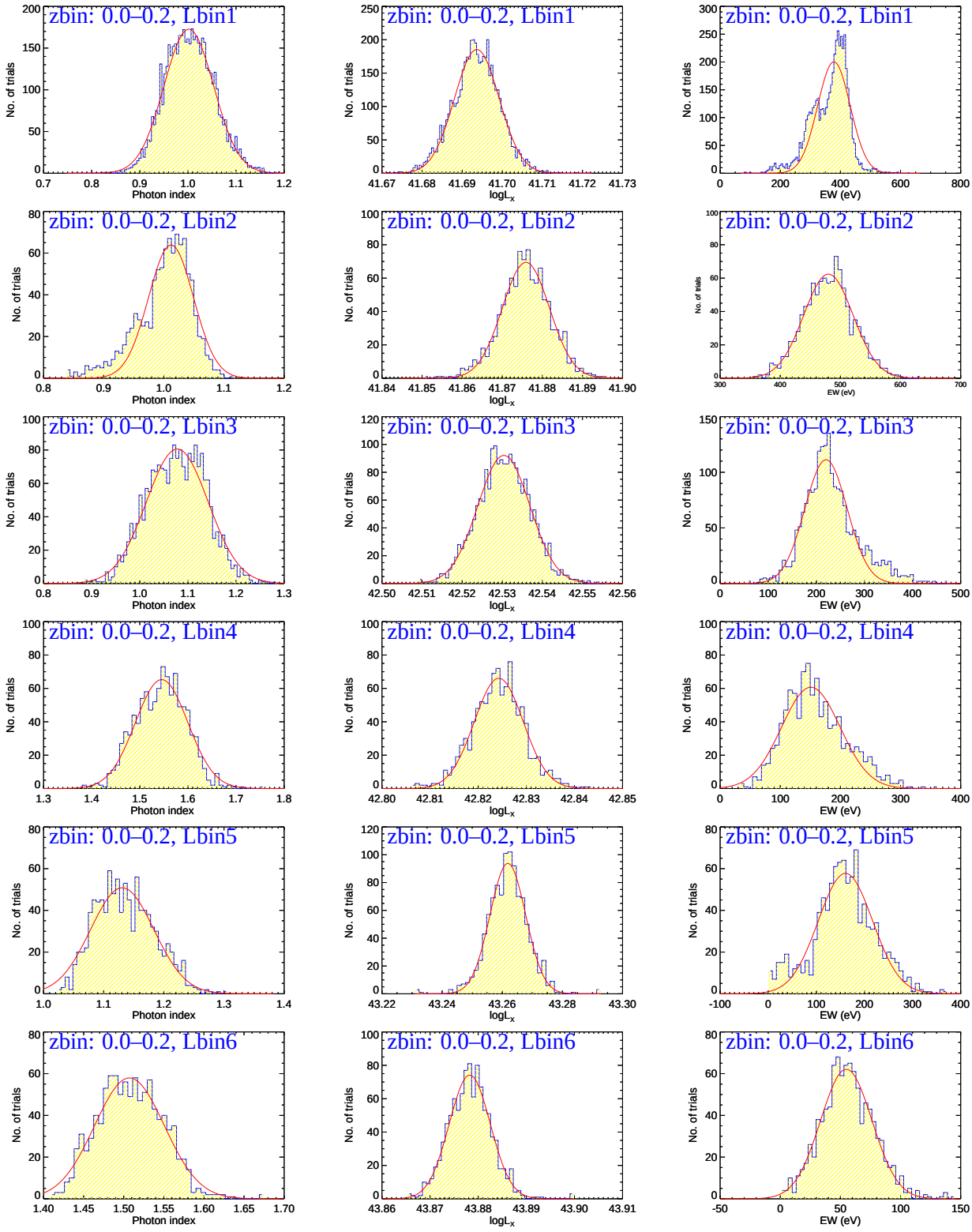

Figure 3.5: Histograms of the simulated stacked spectrum fit parameters overlaid with the fitted Gaussian function in the six luminosity bins in the redshift range 0.0–0.2. The *left panels* in each row display the power law photon index distributions, while the *central panels* are the X-ray luminosity distributions and the *right panels* show the narrow Fe Kα line equivalent width (EW) distributions.

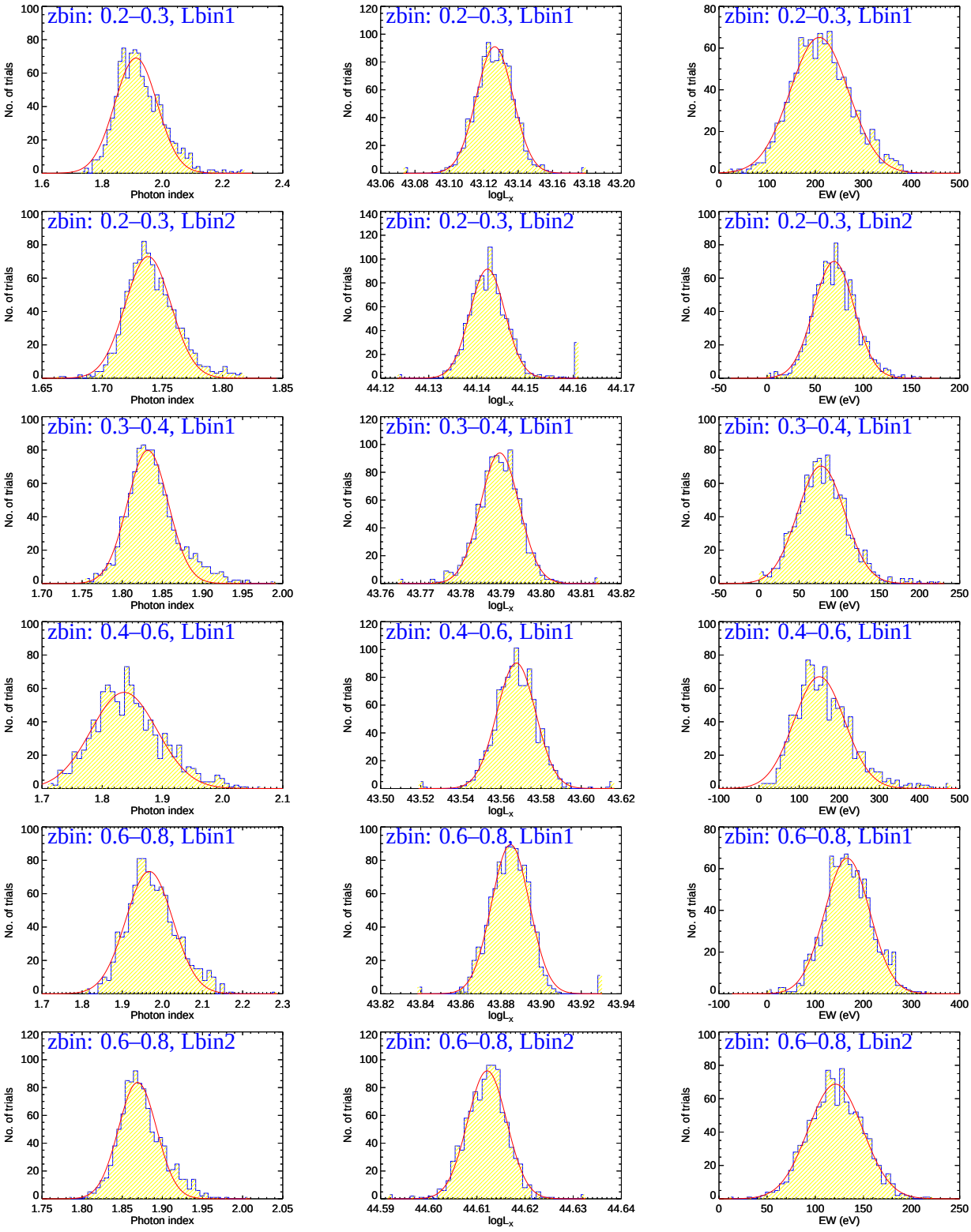

Figure 3.6: Histograms of the simulated stacked spectrum fit parameters overlaid with the fitted Gaussian function in the quoted redshift and luminosity bin(s). The *left panels* in each row display the power law photon index distributions, while the *central panels* are the X-ray luminosity distributions and the *right panels* show the narrow Fe Kα line equivalent width (EW) distributions.

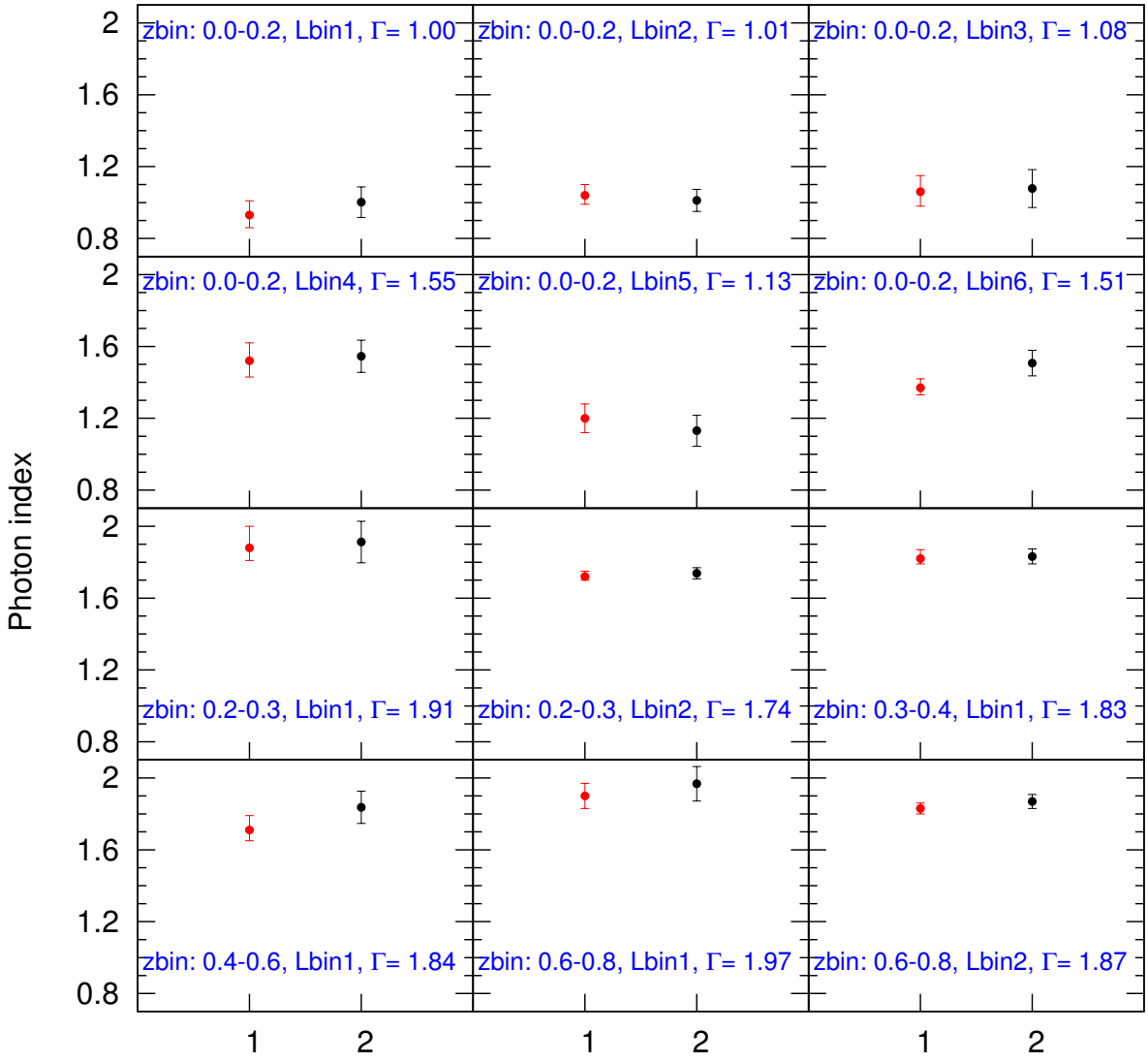

Figure 3.7: Comparison of the power law photon indices (Γ) of the real (red) and simulated (black) stacked spectra in the quoted redshift and luminosity bin(s). The average Γ value determined from the simulated stacked spectra is also reported. The numeric X-axis values have been arbitrarily selected. The number 1 is used for the real, while the number 2 is adopted for the simulations.

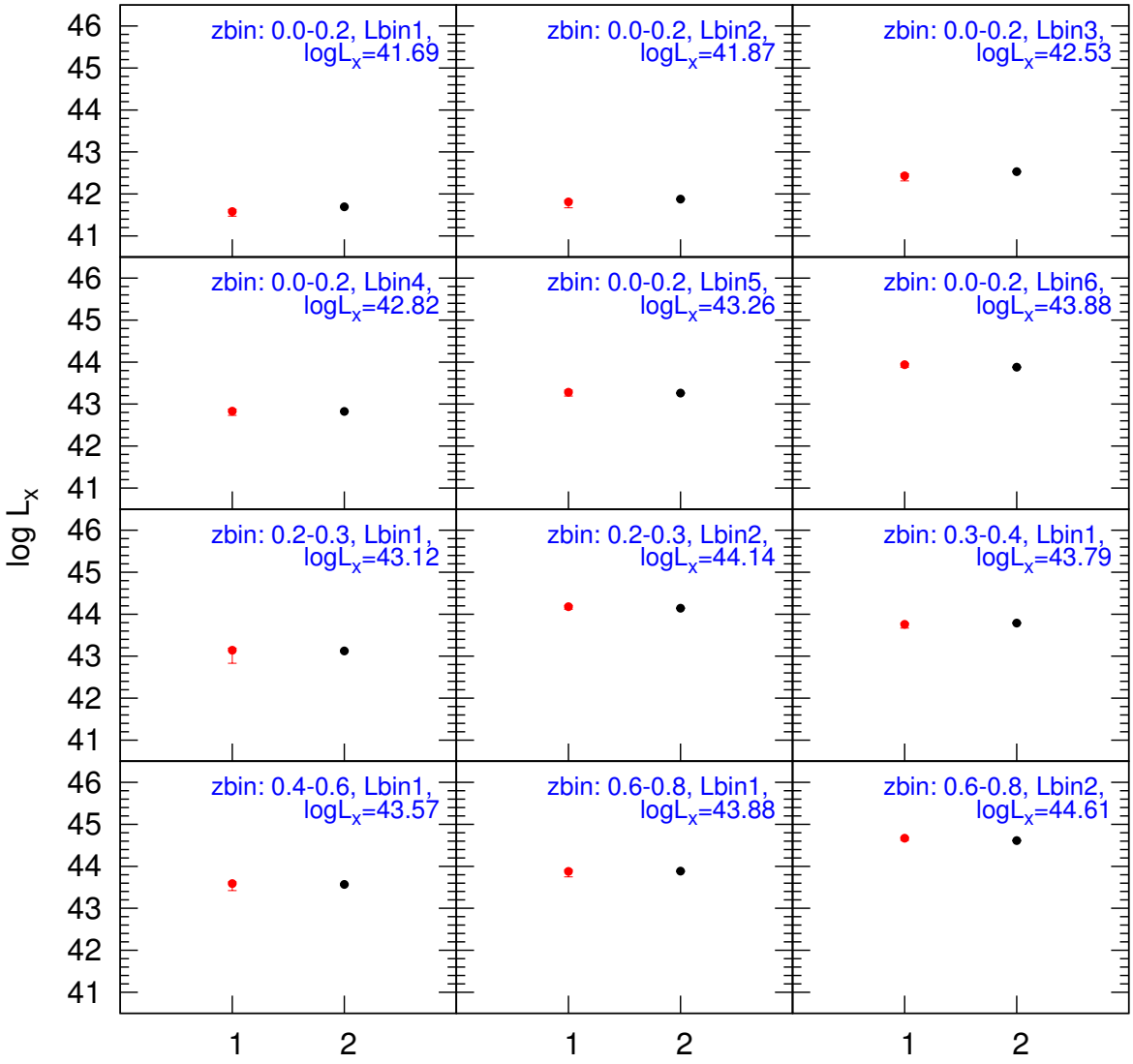

Figure 3.8: Comparison of the 2–10 keV X-ray luminosities of the real (red) and simulated (black) stacked spectra in the quoted redshift and luminosity bin(s). The average X-ray luminosity determined from the simulated stacked spectra is also reported. The numeric X-axis values have been arbitrarily selected. The number 1 is used for the real, while the number 2 is adopted for the simulations.

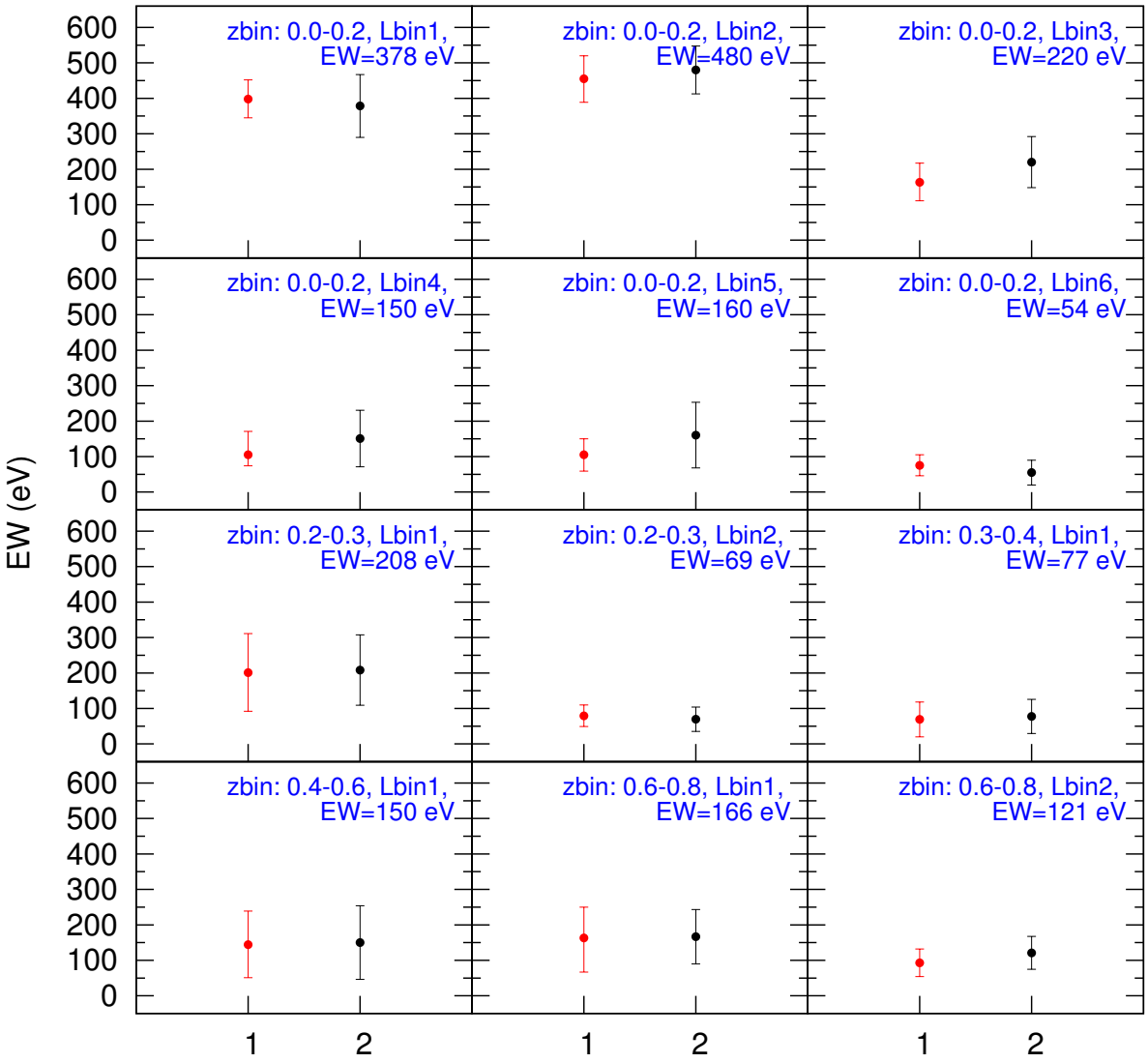

Figure 3.9: Comparison of the narrow Fe Kα lines EWs in the real (red) and simulated (black) stacked spectra in the quoted redshift and luminosity bin(s). The average EW determined from the simulated stacked spectra is also reported. The numeric X-axis values have been arbitrarily selected. The number 1 is used for the real, while the number 2 is adopted for the simulations.

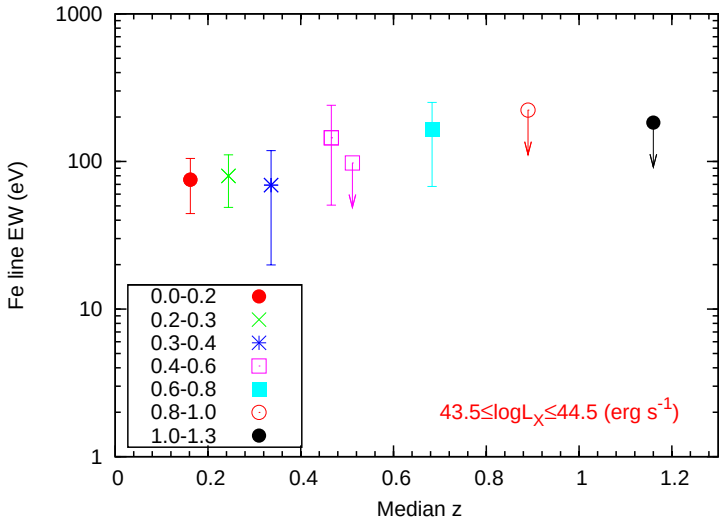

Figure 3.10: Rest-frame equivalent width as a function of redshift.

3.5 Results and Discussion

Here we discuss the results of our work in different redshift and luminosity bins. At low redshifts ($z \leq 0.4$) F-test probability of the Fe Kα line detection is greater than 90% in all luminosity bins. In the redshift range $0.4 < z \leq 0.8$ the average F-test probability of the Fe Kα line detection is ~95% in the lowest luminosity bin. An upper limit on the Fe Kα EW was derived for the non-significant line detections in all redshift and luminosity bins at $z > 0.8$.

One key advantage of our sample with respect to previous published works is that it includes higher statistics covering a wide range of luminosities at various redshifts. We can therefore address the separate redshift and luminosity dependences of the Fe line strength.

3.5.1 Evolution of the Fe line equivalent width with redshift

First, we searched for a dependence of the Fe Kα line intensity on cosmic time (redshift). We selected the narrow luminosity range of $43.5 \leq \log L_X \leq 44.5$ to cover a redshift range as wide as possible for an almost constant luminosity. This sample contains 206 sources grouped in 7 redshift bins in the range $0 < z < 1.3$ and an average luminosity of $\log L_X$(2-10 keV) = 44.04 ± 0.30 (rms dispersion). We find that the intensity of the Fe Kα line does not change significantly up to $z \sim 0.8$ as displayed in Figure 3.10, where the measured EWs with their associated errors and upper limits are plotted. The upper limits at $z > 0.8$ are also consistent with a non evolution. The non evolution of the Fe Kα line intensity can be interpreted as constant Fe abundance with redshift (Brusa et al. 2005). Studies of quasar elemental abundances (derived from broad optical emission lines) also reported a similar (non evolutionary) trend of metallicity with redshift up to $z \sim 4.5$ (Hamann et al. 2007). In contrast, Balestra et al. (2007) found significant evidence of a decrease in the average Fe abundance of the intra-cluster medium as a function of redshift, at least up to $z \simeq 0.5$. The comparison of these two results implies a different

evolution of the Fe abundance with redshift in these two very different systems (AGNs and ICM) and/or very different scales (pc versus Mpc).

3.5.2 The IT effect

We then looked for a dependence of the Fe Kα line strength on the X-ray luminosity. Figure 3.11 shows the relation between the average rest-frame EW and 2–10 keV luminosity in all redshift and their associated luminosity bins. The weakening of the line strength with increasing luminosity is clearly present. To derive the relation between the two parameters we followed the method of (Guainazzi et al. 2006b). Their method can be summarized as follows. First, a set of Monte-Carlo simulated data is derived from the EWs (both upper limits and measurements with their associated symmetric errors) according to the following rules: (i) each measured EW was substituted by a random Gaussian distribution, whose mean is the best fit value and whose standard deviation is its statistical uncertainty; (ii) each upper limit (U) was substituted by a random uniform distribution in the interval [0,U]. Then, ordinary least squares fits were performed on each Monte-Carlo simulated data set. The mean of the slopes and the intercepts derived from the fits of each data set are taken as the "best fit parameters of the linear relation". We obtained the following best fit relation:

$$\log(EW_{Fe}) = (1.66 \pm 0.09) + (-0.43 \pm 0.07)\log(L_{X,44}) \tag{3.1}$$

where EW_{Fe} is the equivalent width of the narrow Fe Kα line in eV and $L_{X,44}$ is the 2–10 keV X-ray luminosity in units of 10^{44} erg s^{-1}. To test the significance of this anti-correlation, we calculated the Spearman's rank coefficient (R_S) for each Monte Carlo simulated data set. The mean value is taken as the R_S of Equation 3.1. The R_S for this correlation is -0.74, corresponding to a Null Hypothesis Probability (NHP) of 2.95×10^{-4}.

Our data therefore strongly imply that the Fe Kα line strength in the selected samples decreases as a function of increasing luminosity in all redshift bins confirming the IT effect. In the previous Section 3.5.1, we explored the redshift dependence of the Fe Kα line intensity. The observed non evolutionary behavior assured us that no additional redshift effects are introduced in the IT relation given by Equation 3.1, which includes different luminosities and therefore on average different redshifts. This indicates that the driver of the observed IT correlation is luminosity and not redshift.

However, the slope of the EW_{Fe} versus L_X relation we obtained is steeper than the value reported in previous studies (-0.20 ± 0.03 (Iwasawa & Taniguchi 1993); -0.17 ± 0.08 (Page et al. 2004); -0.17 ± 0.03 (Bianchi et al. 2007)). The normalization of our EW_{Fe} versus L_X relation is statistically consistent with that reported by Bianchi et al. (2007). To check whether this discrepancy in the slope is due to the 2 extreme points at $L_X < 10^{42}$ erg s^{-1}, we removed these points and subsequently performed the linear fits. We still obtained a slope of -0.43 ± 0.09 with $R_S = -0.67$ and NHP $= 3.24 \times 10^{-3}$.

This discrepancy in the slope can possibly be attributed to the difference in composition of the samples. Indeed, the sample in Bianchi et al. (2007) consists of 157 local unobscured radio quiet AGNs (almost 90% within $z < 1$), whereas our sample comprises a mixture of 507 obscured and

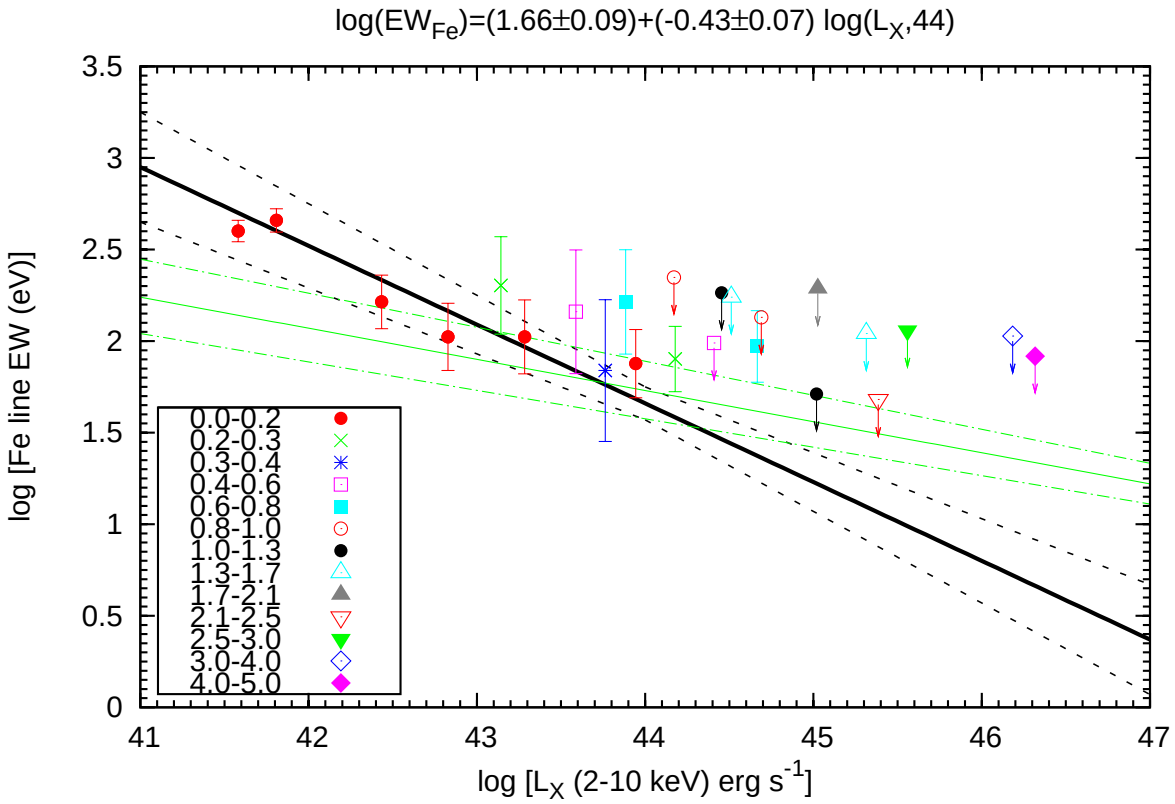

Figure 3.11: Rest-frame equivalent width of the narrow Fe Kα line (σ = 0.1 keV) in different redshift intervals plotted against the X-ray luminosity in the 2–10 keV band. The solid black line indicates the best fit to all the detections including upper limits. The fit relation is reported on the top. The solid green line represents the best fit relation reported by Bianchi et al. (2007). The combined error range on the slope and normalization of the best fit is also shown by dotted lines in the respective colors.

unobscured sources over a broader z range (69% at $z < 1$ and 31% at $z > 1$). The difference in the slope we obtain for the whole sample can also be driven by the upper limits in the highest redshift bins which are not sampled by Bianchi et al. (2007). When all bins in the redshift range $0 < z < 0.8$ are considered (see Figure 3.12), the inverse correlation between the EW and X-ray luminosity becomes

$$\log(EW_{Fe}) = (1.85 \pm 0.11) + (-0.32 \pm 0.07)\log(L_{X,44}) \tag{3.2}$$

with $R_S = -0.64$ and NHP= 3.63×10^{-2}. The slope of the anticorrelation is statistically consistent in Equation 3.1 and 3.2. However, the best fit value is flatter in Equation 3.2. This in turn supports the hypothesis that upper limits are an important factor in the calculation of the fit relation.

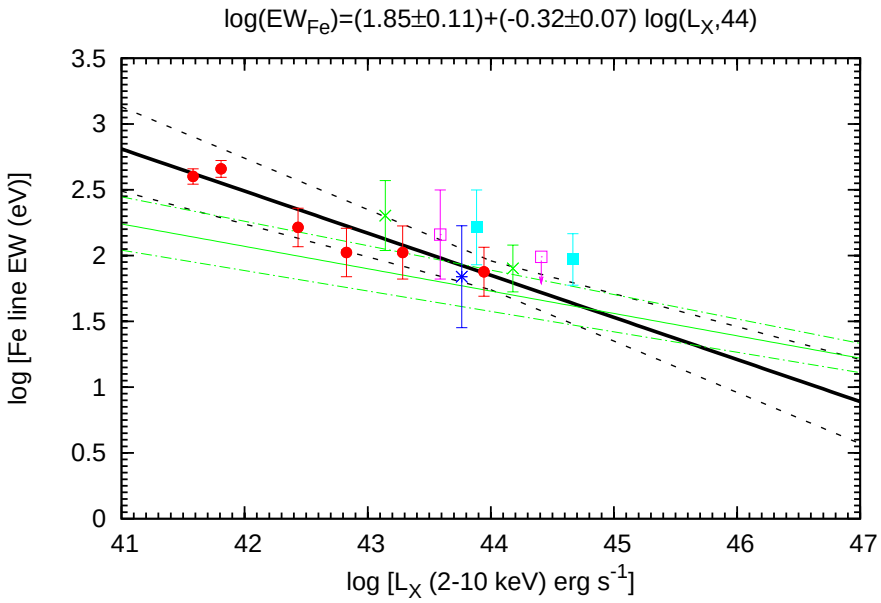

Figure 3.12: Rest-frame equivalent width of the narrow Fe Kα line in the redshift interval $0 < z < 0.8$ plotted against the X-ray luminosity in the 2–10 keV band. (Symbols, line styles and colors same as in Figure 3.11).

The physical origin of the IT effect is related to where the line is originated. Several studies have confirmed that the narrow neutral Fe Kα line is a ubiquitous component in AGNs X-ray spectra (Page et al. 2004; Yaqoob & Padmanabhan 2004; Corral et al. 2008). The measured widths vary substantially from source to source and cover a wide range from 1000 to 15000 km s^{-1} (Yaqoob & Padmanabhan 2004), thus being consistent either with an origin from the broad line region (BLR) or the torus (obscuring circumnuclear matter) envisaged in orientation-dependent unification scheme for AGNs (Urry & Padovani 1995). The original IT effect (Iwasawa & Taniguchi 1993) was attributed to a decrease in the covering factor of the BLR with increasing X-ray luminosity. However, recent studies report that no strong correlation exists between the Fe Kα core width and prominent BLR Hβ λ4861 line width (Nandra 2006). There is a similar lack of correlation between the EWs of the Fe Kα and CIV λ1549 lines (Wu et al. 2009a). This implies that the Fe Kα line is unlikely to be produced in the BLR.

Based on previous studies, the abundance effect and black hole mass can be ruled out as the primary physical parameters driving the correlation (Page et al. 2004; Zhou & Wang 2005; Nandra 2006; Bianchi et al. 2007). The absence of evolution of the Fe Kα EW with redshift (see Section 3.5.1) further confirms this hypothesis. Assuming that the line is originated in the torus, the luminosity dependent covering factor of the torus turns out to be the most likely explanation for the IT effect (Page et al. 2004; Bianchi et al. 2007). A lower covering factor signifies that the torus obscures a smaller solid angle around the nucleus, and hence less Fe K-edge photons are captured and generate less Fe Kα photons, leading to a reduction in the EW. In this way,

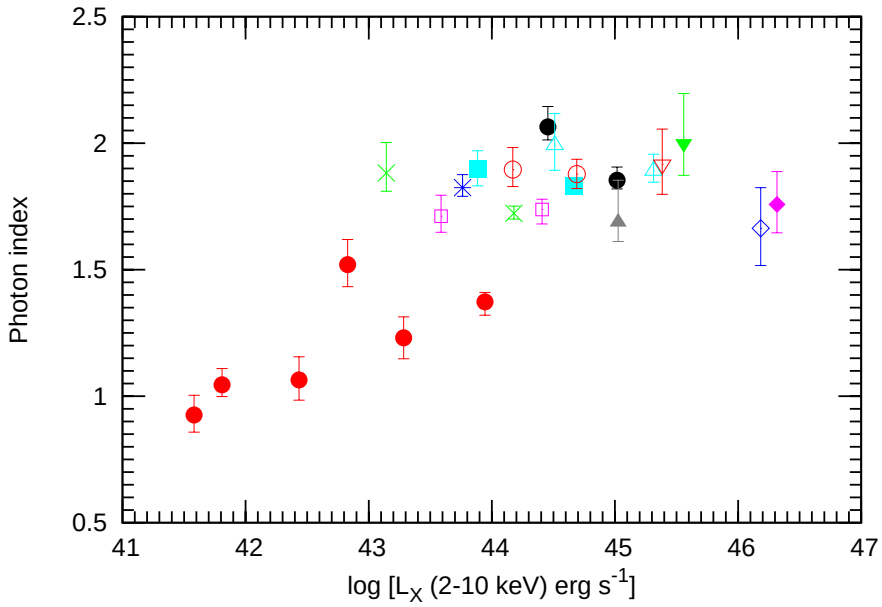

Figure 3.13: The variation of the power law photon index as a function of the rest-frame 2–10 keV luminosity is illustrated. Symbols reflect different redshift bins as in Figure 3.11.

an increase in luminosity and a subsequent decrease in the covering factor could explain the observed anticorrelation of the EW and X-ray luminosity.

An immediate implication of the luminosity dependent covering factor of the torus is the variation in the underlying continuum with luminosity as high covering factor at low luminosities would cause spectral hardening by suppressing the soft part of the spectrum. To confirm this argument, we investigated the dependence of the power law photon index (characterizing the underlying continuum) on the X-ray luminosity in different redshift bins. In order to avoid the complexity of the AGNs spectra at energies below 2 keV, we performed spectral analysis in the 2–10 keV rest-frame band. Figure 3.13 illustrates the variation of the power law photon index (Γ) with the 2–10 keV luminosity in different redshift intervals. We found that the Γ in our stacked spectra sample is hard at low X-ray luminosities ($L_X < 10^{43}$ erg s^{-1}) sampled mostly in the redshift bin 0.0–0.2. A hard Γ is indeed expected in the case of increasing absorption at these luminosities due to a high covering factor. The trend also reflects the decrease of the fraction of the absorbed sources with the X-ray luminosity revealed from extensive works in hard X-ray surveys studies (Ueda et al. 2003; La Franca et al. 2005; Hasinger 2008).

3.6 Conclusions

We have compiled a large sample of 507 sources selected from the 2XMM catalog covering the redshift range $0 < z < 5$ and nearly 6 orders of magnitude in the X-ray luminosity. To improve the signal-to-noise ratio and investigate the average X-ray spectral properties of the

sources, we computed the integrated spectra in narrow intervals of redshift and luminosity. We performed simulations to assess the accuracy of the stacking procedure. The main results can be summarized as follows.

- We confirm that the narrow Fe Kα line is an almost ubiquitous feature in the X-ray spectra of AGNs.
- In the integrated spectra spanning redshift range $0 < z < 1.3$ at nearly constant luminosity we detect no strong trend in the Fe Kα line EW with redshift.
- We find a significant anticorrelation between the Fe Kα EW and 2–10 keV rest-frame luminosity across a wide redshift range not probed in prior studies. The slope of the anticorrelation we obtained is steeper than the value reported in previous studies, likely due to the difference in composition of the samples. The exact physical cause of the IT effect is unknown, one promising explanation is a decline in the covering factor of the putative molecular torus as the luminosity increases.
- We find a hardening of the spectral indices at low luminosities in the redshift bin 0.0–0.2. This can be linked to the dependence of obscuration with luminosity.

Chapter 4

Rest-frame stacking of 2XMM catalog sources: Properties of the Fe Kα line

4.1 Rationale

Fluorescent Fe Kα lines in active galactic nuclei (AGNs) are a potentially unique tool to probe the innermost regions around a black hole. The line properties, such as the peak energy, intensity and profile carry important diagnostic information about the dynamics and physics of the region where the emission originates. The measured line energy can be used to infer the ionization state of the line emitting matter, whereas the line equivalent width (EW) indicates the amount of fluorescing material (Fabian et al. 2000).

The line profile is determined by several physical parameters. The Fe Kα line in AGNs is assumed to be produced through X-ray irradiation of optically thick matter, such as the molecular torus and/or the accretion disk (Guilbert & Rees 1988; Lightman & White 1988; George & Fabian 1991; Matt et al. 1991). If the Fe Kα line arises in distant material like the molecular torus envisaged in orientation–dependent unification scheme for AGNs (Antonucci 1993), the resulting emission line profile is narrow. In contrast, the Fe Kα line originating in the inner accretion disk is distorted by Doppler and gravitational effects and becomes asymmetric (Fabian et al. 1989; Laor 1991). Hence, relativistic lines offer a robust way to measure accretion disk properties, such as the radial extent, the emissivity profile, the inclination angle of the disk to the observer's line of sight and the black hole spin (for the reviews see Reynolds & Nowak 2003; Fabian & Miniutti 2005; Miller 2007; Turner & Miller 2009).

The last decade has witnessed a significant improvement in our knowledge of the narrow Fe Kα line properties in AGNs. Based on data collected with high-sensitivity X-ray satellites XMM-*Newton*, *Chandra* and *Suzaku* the ubiquitous presence of a neutral, narrow Fe Kα line in AGNs spectra has been established (Yaqoob & Padmanabhan 2004; Guainazzi et al. 2006a; Reeves et al. 2006; Nandra et al. 2007). The behavior of the Fe Kα line as a function of the X-luminosity and redshift has also been examined. Compelling evidence of the inverse correlation between the neutral, narrow Fe Kα line EW and X-ray luminosity, known as the X-ray Baldwin effect (Iwasawa-Taniguci effect), has been reported (Iwasawa & Taniguchi 1993; Nandra et al.

1997; Page et al. 2004; Bianchi et al. 2007; Chaudhary et al. 2010; Shu et al. 2010). However, the EW is observed to be independent of the redshift (Brusa et al. 2005; Chaudhary et al. 2010).

While the presence of a narrow line component is confirmed by all independent analyses, the evidence of the presence of a broad line is more debated. The complex nature of AGNs spectra, and, in particular, the degeneracy between the spectral parameters and the dependence of the line EW and shape over the fitted (absorbed) continuum, hampered so far a comprehensive interpretation of the physics behind the observed features. As an example, it has also been proposed that the observed red-wing can also be ascribed to complex (clumpy) absorption at least for MCG–6-30-15 (Miller et al. 2009). It is therefore critical to have multiple independent procedures to determine the Fe line parameters.

In this chapter we study a small but well-defined sample of AGNs taken from our parent sample of 507 sources and concentrate on the mean properties of the Fe K line in the rest-frame using two different procedures. This chapter is organized as follows: Section 4.2 describes the selection criteria and properties of the sample. Section 4.3 outlines the rest-frame stacking procedures. The results of the spectral analysis are presented in Section 4.4 and are discussed in Section 4.5. The conclusions are summarized in Section 4.6.

4.2 The sample

We start with our reference sample of 507 AGNs at high galactic latitude ($|BII| > 25$ degrees), with the sum of the EPIC-PN and EPIC-MOS 0.2–12 keV counts greater than 1000 and covering the redshift range $0 < z < 5$ (See Chapter 2 for all the details on the selection of the sample).

An essential requirement of the conventional rest-frame stacking analysis is the spectrum unfolding by appropriately modeling the underlying continuum. Therefore, to carry out a reliable spectral analysis of each spectrum, we refined the sample of 507 AGNs by considering only the AGNs with the EPIC-PN net 2–10 keV rest-frame counts ≥200 (~73% of the reference sample). As our main interest is in the Fe K region of the spectrum, we analyzed each source spectrum in the rest-frame 2–10 keV energy range, excluding the 5.5–7.0 keV Fe band[1] using `XSPEC` (ver. 12.6.0; Arnaud 1996). We fitted the data with an absorbed power law[2]. Only the EPIC-PN data has been used in this work. In the second part of Appendix Table A.3 we list a few parameters namely the EPIC-PN net counts, power law photon index (Γ) and X-ray luminosity derived from the spectral analysis in rest-frame 2–10 keV range.

From the original sample of 507 sources, we further selected a sample of 248 AGNs having their power law photon indices as derived from the above mentioned fits in the range $1.5 \leq \Gamma \leq 2.2$. The imposed threshold on Γ ensured that our results are stable against the continuum normalization and the contribution of the highly obscured AGNs with prominent Fe K lines is minimum. The *top row* in Fig. 4.1 shows the distributions of the EPIC-PN net counts (*left*) and

[1] Spectral fits excluding 5–7 keV and 6–7 keV have also been performed. This did not change the results.

[2] We also tested a model with a neutral reflection component (`pexrav` in `XSPEC`, see Magdziarz & Zdziarski 1995). However, our choice of the spectral energy range (2–10 keV) and the limited statistics in the majority of spectra (see Fig. 4.1 for sample properties) restrained a full parametrization of the reflected continuum. We therefore adopted a simple absorbed power law continuum for all sources.

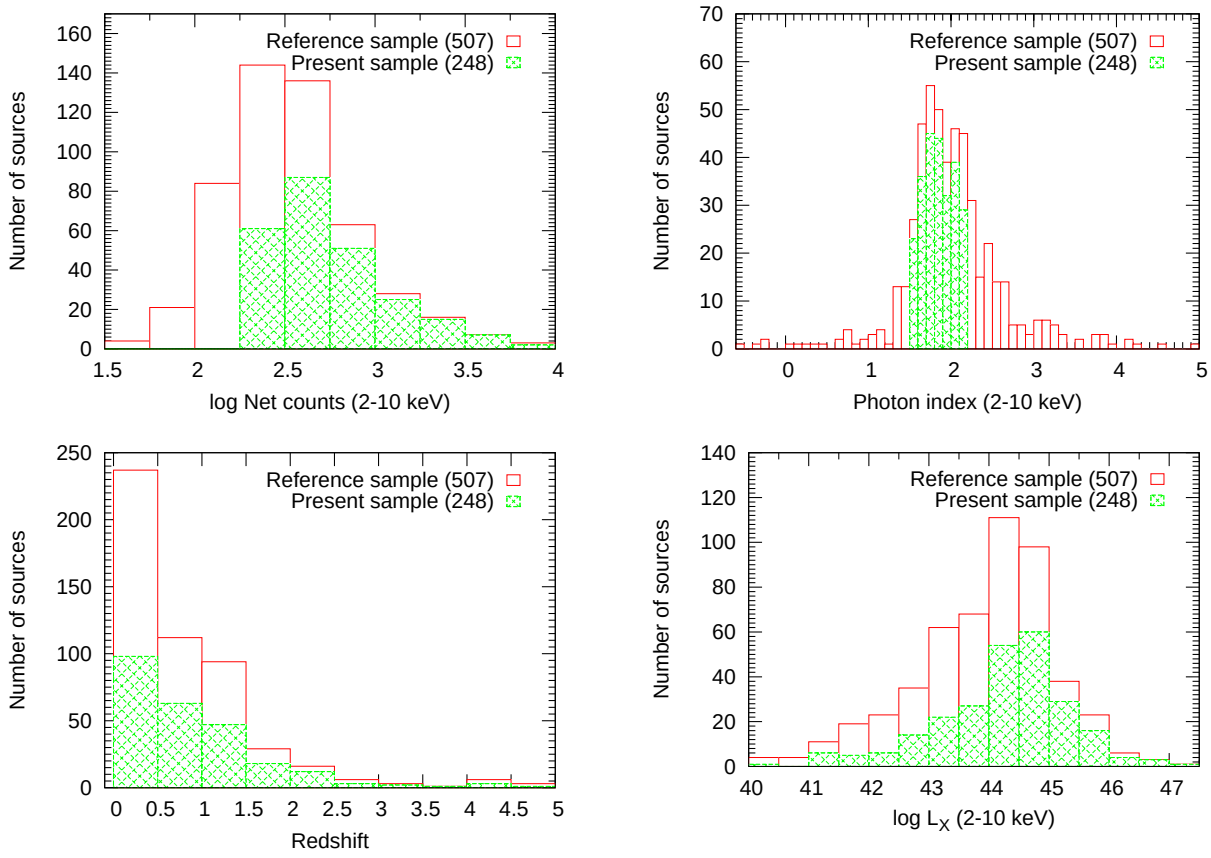

Figure 4.1: *Top:* distributions of the EPIC-PN net counts (*left*) and 2–10 keV power law photon indices (*right*) of the 248 sources selected for our study (green cross-hatched) compared with the reference sample (red solid line). *Bottom:* redshift (*left*) and rest-frame 2–10 keV luminosity, no absorption correction (*right*) distributions of these two samples. The total number of sources in each sample is also reported.

power law photon indices in the rest-frame 2–10 keV band (*right*) of the 248 sources used in this work (green cross-hatched) compared to the reference sample (red solid line). The *bottom row* shows overlaid histograms of redshifts (*left*) and 2–10 keV luminosities, not corrected for absorption (*right*) for these two samples. We note that the selected subsample of 248 AGNs can be considered a fair representative of the reference sample in terms of the X-ray luminosity and redshift.

4.3 Rest-frame stacking procedures

4.3.1 Stacked ratio

A commonly employed method to study the average Fe K line properties is to derive the average of the ratio between the data and a simple continuum model for each source under study (e.g. Nandra et al. 1997; Guainazzi et al. 2006a). However, several key factors should be considered in the stacking analysis when the sample sources have a wide redshift distribution. These include different redshift of each source and thus a different observed line energy, the energy dependent detector response is also different for each source.

Taking into account all these factors we adopted the following procedure for constructing an average ratio profile for our AGNs sample.

- For each source, we determined the observed-frame energy range corresponding to the rest-frame 2–10 keV band and the associated ungrouped channel information from the respective response files. Each spectrum, in the rest-frame 2–10 keV band, was then grouped in predefined bins of widths equal to $0.25/(1+z)$ up to 8 keV and $1/(1+z)$ in the 8–10 keV using the `FTOOLS` routine `grppha`, which corresponds to a rest-frame sampling of 0.25 keV and 1 keV in the 2–8 keV and 8–10 keV, respectively. Thus, we had 26 energy bins in each spectrum. For illustration purposes, six redshift corrected source spectra grouped in 26 predefined energy bins in the 2–10 keV range are presented in Fig. 4.2.

- Given the limiting counting statistics and the choice of predefined binning we could not assure a minimum of 20 counts per bin. We therefore analyzed the binned, background-subtracted, 2–10 keV rest-frame spectra with an absorbed power law using the Cash statistic (Cash 1979) implemented in `XSPEC`. The best fit parameters (N_H and Γ etc. with errors) and ratio with respect to the best fit continuum model were saved.

- These ratios were then summed and averaged for all the sources in each rest-frame energy bin. First, we derived the mean and standard deviation of the ratios in each energy bin. We then removed in each energy bin all the ratios deviating more than 3 times the standard deviation from the average value (3–sigma clipping). Figure 4.3 shows the resulting averaged ratio (red) comprising $\geq$95% of ratios in each energy bin compared with the mean ratio for the whole sample of the 248 sources (blue). We find that the two ratio profiles are consistent within the errors as expected. We note that the 3–sigma clipped averaged ratio (red) is comparatively lower at high energies (>7 keV) as the contribution of the ratios deviating significantly from the average value in these bins is removed.

- The averaged ratio cannot be fitted directly in `XSPEC` and it must be converted to a flux spectrum taking into account the average underlying continuum, we therefore converted the averaged ratio created by applying 3–sigma clipping (red points in Fig. 4.3) to a flux spectrum by multiplying the averaged ratio in each energy bin by the $E^{-\Gamma}$ factor, where E is the central rest-frame energy of the bin and Γ(=1.8) is the mean slope of our sample. We refer to this flux spectrum as the "averaged ratio flux spectrum".

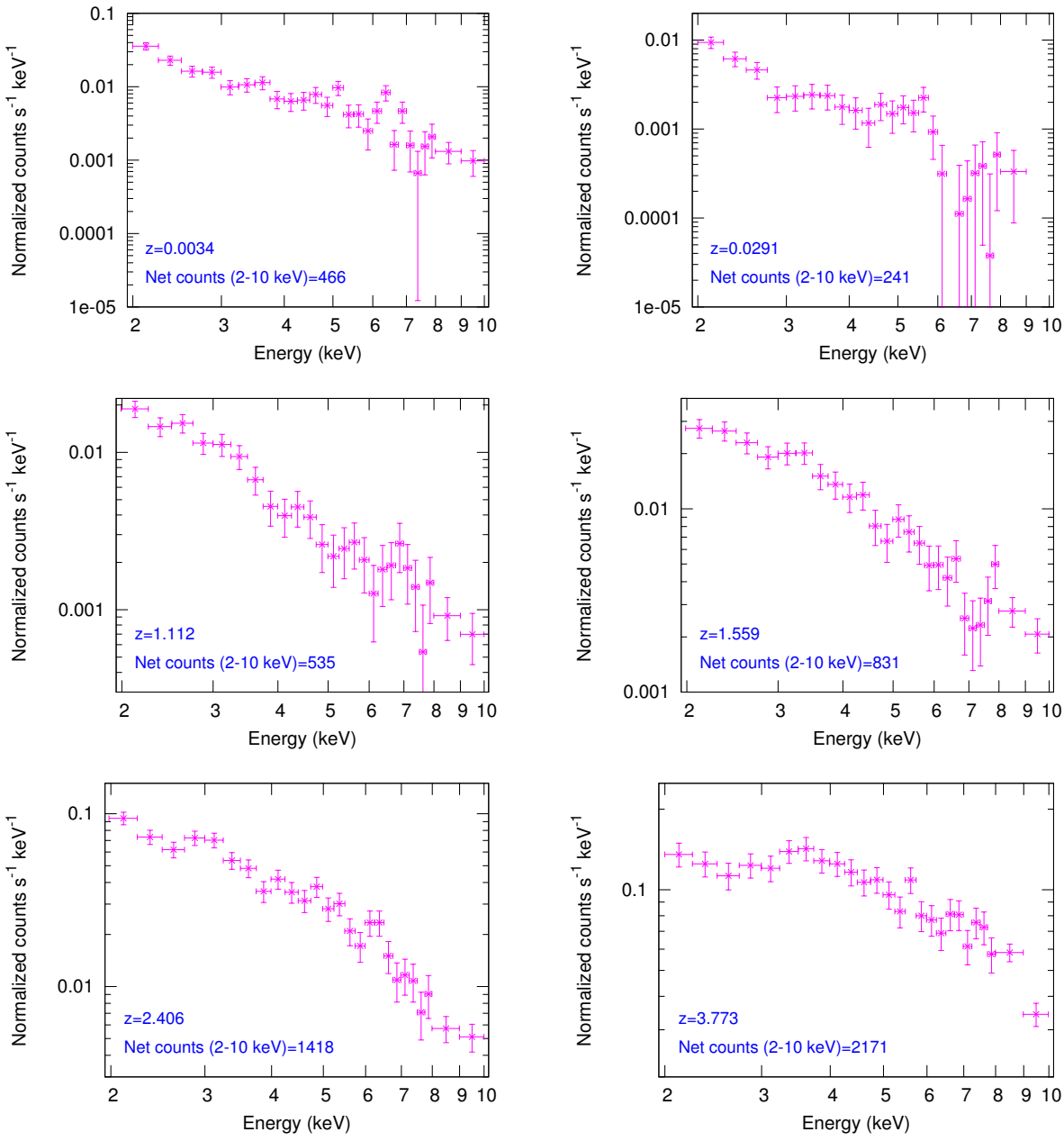

Figure 4.2: Six redshift corrected source spectra grouped in 26 predefined energy bins in the 2–10 keV band. The labels represent the redshift and the EPIC-PN 2–10 net counts for each source.

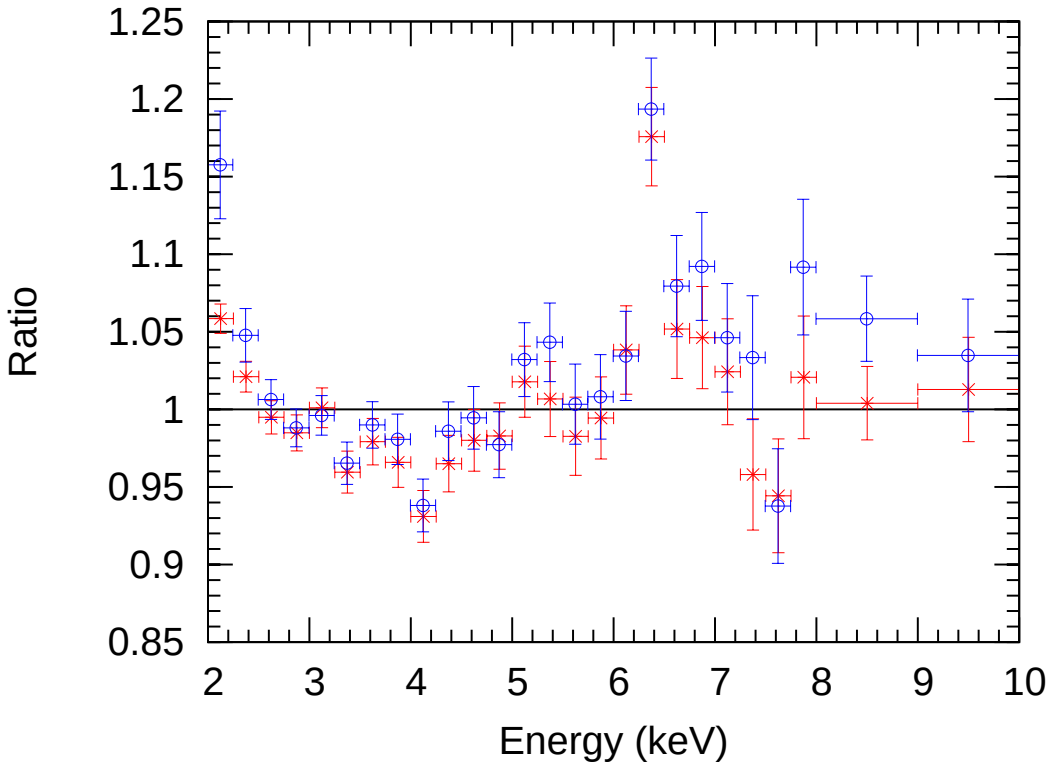

Figure 4.3: Comparison of the mean ratio profiles: the whole sample comprising 248 sources (blue) and after applying 3–sigma clipping on the ratios in each energy bin (red).

4.3.2 Stacked spectrum

We followed the averaging procedure of Iwasawa et al. (2011) for constructing an "averaged X-ray spectrum". The advantage of this procedure is that it is independent of the continuum modeling and statistics used in the spectral analysis. In this procedure original data, in units of counts s^{-1} keV^{-1}, of each spectrum were saved after loading the spectrum grouped as described above. We also created the ascii tables of the ancillary response matrices (.arf) with the same binning as of the spectrum. The data were then divided by the average effective area in each energy bin, and thereafter normalized to the 3–5 keV continuum to ensure that the average spectrum is not dominated by the brightest objects. The final "averaged X-ray spectrum" is constructed by summing the normalized counts of all the different sources in each rest-frame energy bin and averaging for the total number of sources. A special effort is made to evaluate calibration issues and uncertainties (see Iwasawa et al. (2011) for further details). The total number of the 2–10 keV counts for the 248 sources is ~198000.

The ratio of the "averaged X-ray spectrum" with respect to a power law (green) over-plotted with the mean ratio profile created using 3–sigma clipping (red) is shown in Fig. 4.4. We notice that the two ratio profiles are fully consistent within the statistical errors. Spectral fitting of the "averaged X-ray spectrum" is addressed in more detail in Section 4.4.2.

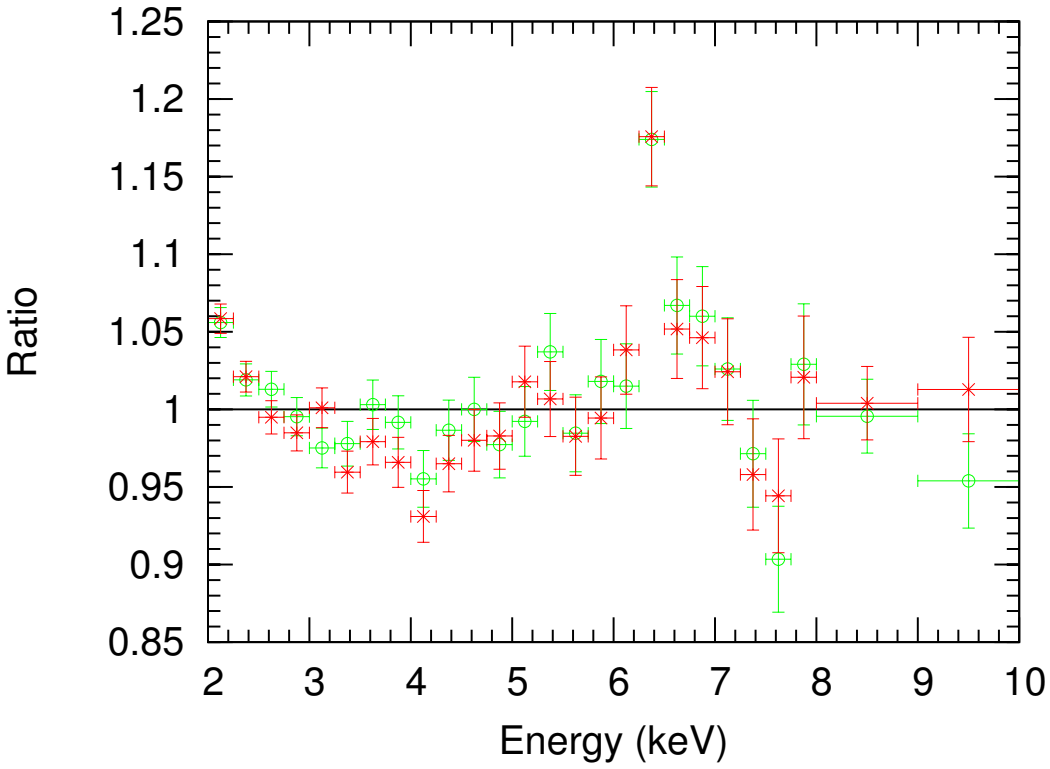

Figure 4.4: Ratio of the "averaged X-ray spectrum" with respect to a power law (green) overlaid with the mean ratio profile of the 248 sources created using 3–sigma clipping (red).

4.3.3 Simulations

To identify the artifacts possibly introduced by the stacking method, we carried out simulations using XSPEC. First, we created 100 simulated "ungrouped" line less spectra for each of the 248 sources using their best spectral fit parameters (e.g, N_H, Γ and power law normalization etc.). Identical response and effective area files were used for the real and simulated spectra.

We then applied the same procedure detailed in Section 4.3.1 to these simulated spectra and computed the mean ratio profile of the 248 simulated spectra for each realization. Thus, we have 100 realizations of the underlying continuum represented by the mean ratio of each realization. We then computed the distribution of these simulated continua. The averaged ratio profile of the 248 spectra (red), mean simulated continuum (black) and its 1σ (green dotted line) and 3σ (blue solid line) deviations in each energy bin are shown in Fig. 4.5.

We note that some apparent deviations (e.g. upward turn at energies below 2.5 keV) present in the averaged ratio profile is also evident in the averaged simulated continuum. This in turn, confirms that simulations can identify very small systematic effects of the order of 5% and the significance of any spectral feature can be deduced with a reliable accuracy. We have investigated the possible reasons for this curvature at energies below 2.5 keV. This effect can be attributed to a combination of the boundary effect (due to our spectral energy range selection) and counting

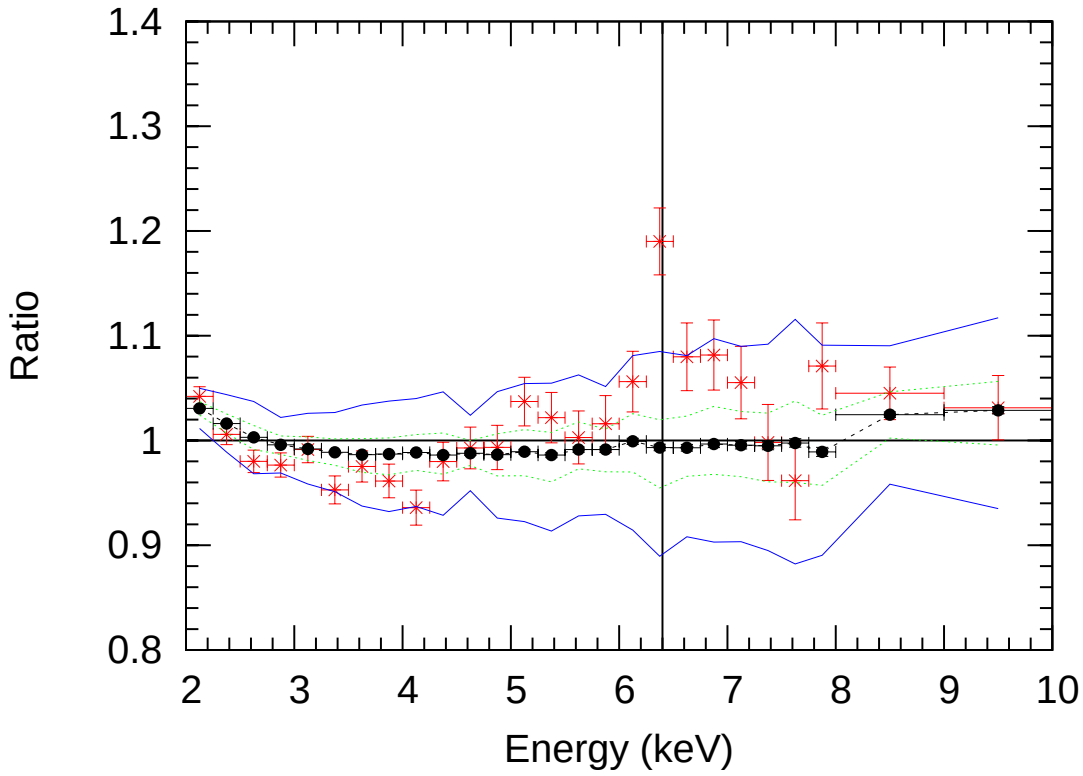

Figure 4.5: Averaged ratio of the 248 spectra after applying 3–sigma clipping (red), mean simulated continuum (black) along with its 1σ (green dotted line) and 3σ (blue solid line) confidence limits. The solid vertical line is drawn at 6.4 keV.

statistics. Indeed, when the averaged ratio profile and the averaged simulated continuum are computed for the sources with net counts >500, we do not find any curvature.

4.4 Results

4.4.1 "Averaged ratio flux spectrum" fitting

We performed a detailed spectral analysis of the "averaged ratio flux spectrum" constructed from the averaged ratio profile as described in Section 4.3.1. All the fit results are shown in Fig. 4.6. We used the `FTOOLS` routine `flx2xsp` to convert the ascii file of the "averaged ratio flux spectrum" to the fits format. To assess the improvement in the spectral fitting on including an additional spectral feature in the fit, we adopt the $\Delta\chi^2$ criterion (e.g. $\Delta\chi^2$ = 2.7 corresponds to 90% significance for the addition of one interesting parameter and $\Delta\chi^2$ = 4.6 corresponds to 90% significance for two additional interesting parameters). Throughout the spectral analysis, errors and upper limits are quoted at the 68% confidence level for one parameter of interest. The errors in the Fe line EW are calculated using `XSPEC` *eqw with err option*.

We first carried out the spectral analysis in the 2–10 keV energy range using various models consisting of simple/complex continuum and one/two Fe Kα lines. However, in all the attempted fits, we noticed the presence of significant residuals of the order of 5% in the 2–3 keV band that can be ascribed to the systematic effect identified by our simulations discussed in Section 4.3.3. Moreover, the 2–3 keV excess resulted in high χ^2 values (e.g. $\chi^2 > 2$) in most of the models explored. Therefore, to obtain more reliable spectral fits, we restricted the spectral analysis of the averaged ratio flux spectrum in the 3–10 keV band.

We then concentrated on the characterization of the narrow Fe K line. To parametrize the narrow core we used a power law plus a narrow Gaussian line with the energy and width fixed at 6.4 keV and 0.01 keV, respectively. The line normalization was allowed to vary. This line model yielded an acceptable fit ($\chi^2/dof = 31.3/19$) and the narrow line is detected at >99.995% significance level ($\Delta\chi^2 \sim 30$ for one additional parameter), with an EW of 45 ± 13 eV. We note that the residuals show excess emission of the order of a few per cent in the 6–7 keV energy range.

To search for the presence of a broad component we replaced the narrow feature with a broad Gaussian by leaving the line width free to vary. The fit was considerably better than a single narrow Gaussian emission line model ($\chi^2/dof = 25.6/18$), with resulting values of the broad line EW of 75 ± 40 eV and a measured width of $\sigma = 0.15^{+0.06}_{-0.04}$ keV. However, we see excess emission around 6.7 keV possibly indicating that the model with a single line component does not fully describe the data. This hypothesis is further supported by the observed improvement in the goodness of fit as a single Fe K line with free width is partially modeling the broad feature.

We next fitted the data with a simple power law and a physically motivated broad line with an emission profile from an accretion disk around a Schwarzschild black hole (`diskline`, Fabian et al. 1989). We fixed several `diskline` parameters; the peak energy, E_{Disk}, at 6.4 keV, the inner disk radius, R_{in}, outer disk radius, R_{out}, at 6 and 100 R_g, respectively, where R_g is the gravitational radius and the emissivity index, β, at −2.5. The free parameters were the disk inclination, i, and normalization. The fit was statistically worse ($\chi^2/dof = 41.6/18$) as compared to the previous ones, which can be attributed to the presence of significant residuals peaking at 6.4 keV. The errors in the fit parameters except the `diskline` EW (128 ± 41 eV) could not be inferred due to the poor fit. Thus, we concluded that a line model consisting of two components should be used to model the Fe K band in our data.

We therefore tested a two component line model consisting of two Gaussians to account for the narrow core and the broad component. The fixed parameters for the narrow component were the same as those in the single narrow Gaussian line fit mentioned above. The line energy of the broad feature was fixed at 6.4 keV, while the broad line width and normalizations of both the lines were free parameters. With an improvement in goodness of fit ($\chi^2/dof = 22.8/17$), the fit with two line components gives narrow and broad line EWs of 28 ± 20 eV and 73 ± 43 eV, respectively. Using a simple power law continuum parametrization, a broad Gaussian Fe Kα line is detected at ∼95% significance ($\Delta\chi^2 \sim 9$ for two additional parameters), with the width of $\sigma = 0.40^{+0.25}_{-0.14}$ keV. On modeling the broad feature with a `diskline` with fit parameters of a single `diskline` fit, we achieved a similar quality fit ($\chi^2/dof = 22.7/17$). The measured EWs of the narrow and diskline components are 39 ± 14 eV and 102^{+49}_{-55} eV, respectively, while the disk inclination is $44.6^{+3.0}_{-8.4}$ degrees. Figure 4.7 plots contours (at 68%, 90% and 99% confidence

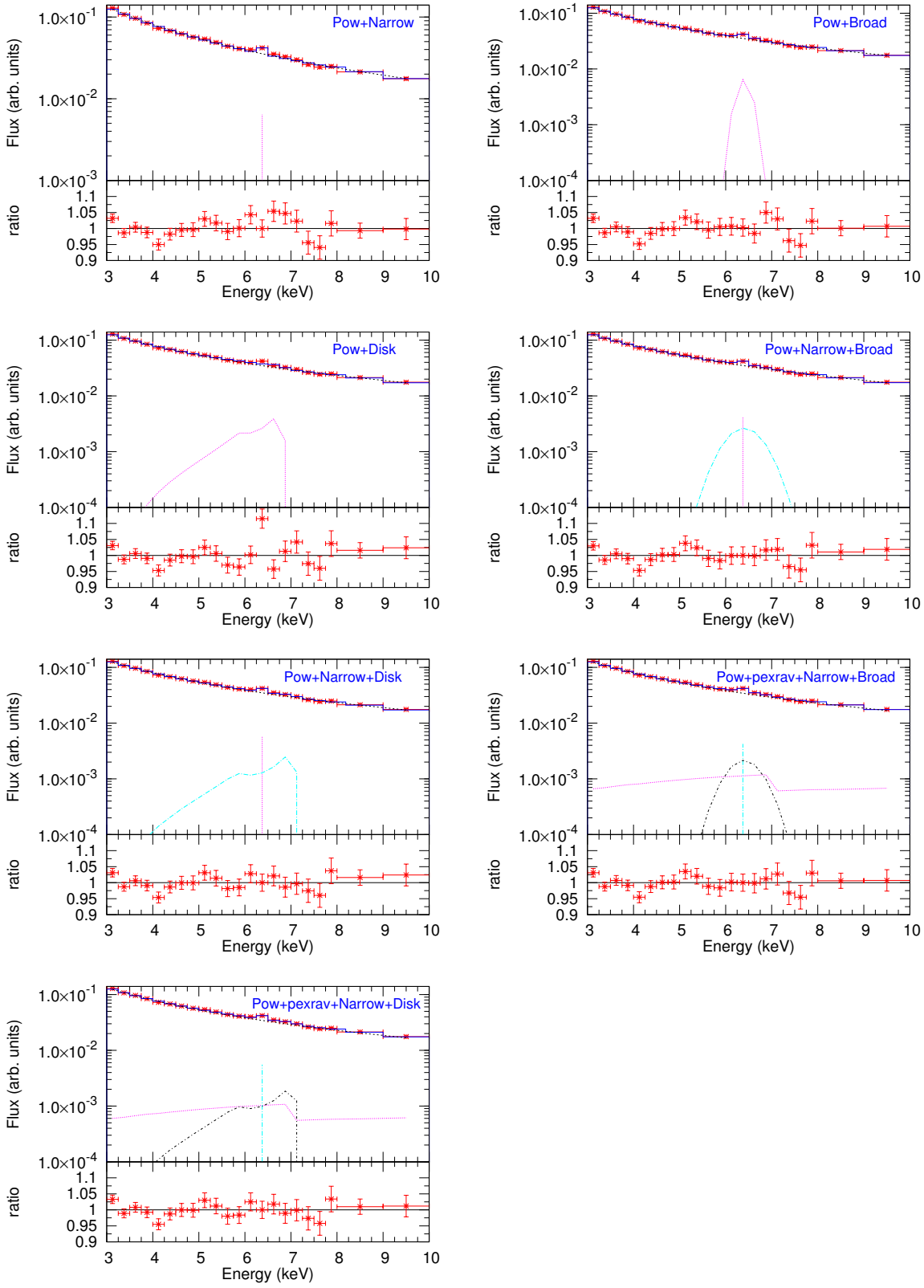

Figure 4.6: *Top panels* in each figure show spectral fit to the "averaged ratio flux spectrum" using the quoted model. In the *bottom panels* ratio with respect to the quoted model is shown. The model components are also displayed.

interval) of the diskline versus narrow component intensities together with the best fit values derived for this fit (mo pow+gaussian+diskline) to the "averaged ratio flux spectrum". We also checked the variation in the diskline EW by fixing the outer disk radius, R_{out} to 1000 R_g as well to the maximum value of 10^7 R_g allowed by the diskline model. The measured diskline EW is found to be within the 2 eV difference of the previous value.

Given the robust detection of the narrow Fe Kα line in the "averaged ratio flux spectrum", a signature of reprocessing in cold, distant material, we added a neutral reflection component using the pexrav in XSPEC (Magdziarz & Zdziarski 1995). The pexrav model computes the spectrum resulting from an exponentially cutoff power law continuum incident on a slab of optically thick, neutral material, accounting for the Compton reflection and bound-free absorption. However, the pexrav does not include any fluorescence emission lines. We use the pexrav to parametrize the reflected continuum only, as the illuminating primary continuum is separately modeled. In this model, the pexrav continuum shape was tied to the mean photon index of the illuminating continuum, Γ (fixed at 1.8), abundances were assumed to be Solar, the inclination of the reflector to the observer's line of sight, $cosi$, and the cutoff energy, $foldE$, were fixed at 0.90 and 200 keV, respectively. The solid angle of the reflector $\Omega/2\pi$ was fixed to 1. The reflection fraction of the distant neutral reflector, R_{Dist}, is derived from the ratio of the reflection component normalization to the power law normalization. The errors in the R_{Dist} are propagated using the standard error propagation formula (Bevington 1969). To account for both the line features we first used two Gaussian lines with parameters set as in the power law continuum modeling.

Overall, the fit statistic is good (χ^2/dof = 21.6/17) with R_{Dist} = 0.27 ± 0.17 and the narrow line EW of 28 ± 20 eV. With this continuum parametrization, the detection significance of the broad Gaussian line with $\sigma = 0.37^{+0.31}_{-0.20}$ is marginal ($\Delta\chi^2 \sim 4$ for two additional parameters). We therefore inferred an upper limit of 105 eV for the broad line EW. When the broad component is modeled by a diskline profile, the fit statistic is similar to the previous fit, with (χ^2/dof = 21.5/17) and the EWs of the narrow and diskline are 37 ± 14 eV and <137 eV, respectively. The fit results are summarized in Table 4.1. The observed variation in the broad line detection significance as a function of the adopted continuum parametrization is noticeable.

4.4.2 "Averaged X-ray spectrum" fitting

We have also carried out a detailed spectral analysis of the "averaged X-ray spectrum" in the 3–10 keV energy range using the four models discussed above with 2 line components. The spectral fits are displayed in Fig. 4.9. We mention that in the "averaged X-ray spectrum" fitting, the free and fixed parameters of the two lines (parametrized by either Gaussians or a narrow and a diskline) are set in accordance with those in the "averaged ratio flux spectrum" fitting. First, the underlying continuum was modeled with a power law and two Gaussian lines representing the narrow and broad features were included. The fit statistic was reasonably good (χ^2/dof = 20.6/17) with the power law photon index, Γ, of 1.64 ± 0.03 and narrow line EW of 28 ± 10 eV, while the broad line EW is 92 ± 35 eV. The broad Gaussian line is detected at the ~99% confidence level ($\Delta\chi^2$ = 11 for two additional parameters), being in an excellent agreement to the corresponding fit of the "averaged ratio flux spectrum". When the broad feature is modeled by a diskline, the fit statistic is excellent (χ^2/dof = 17.4/17) and we recovered the narrow line

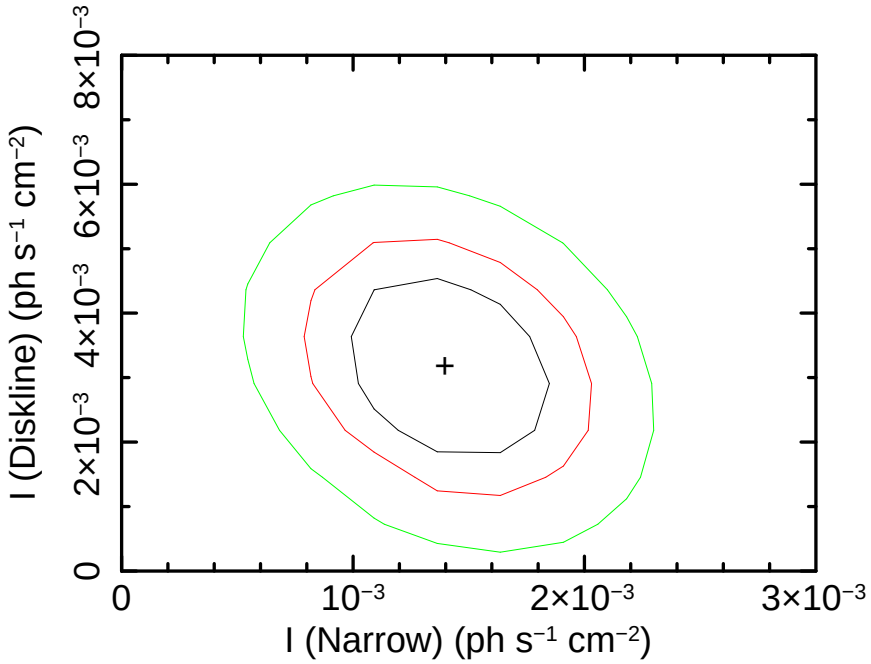

Figure 4.7: Contour plots (68%, 90% and 99%) of the `diskline` versus narrow component intensities for the "averaged ratio flux spectrum". A simple power law is used to model the underlying continuum. The cross indicates the best fit values.

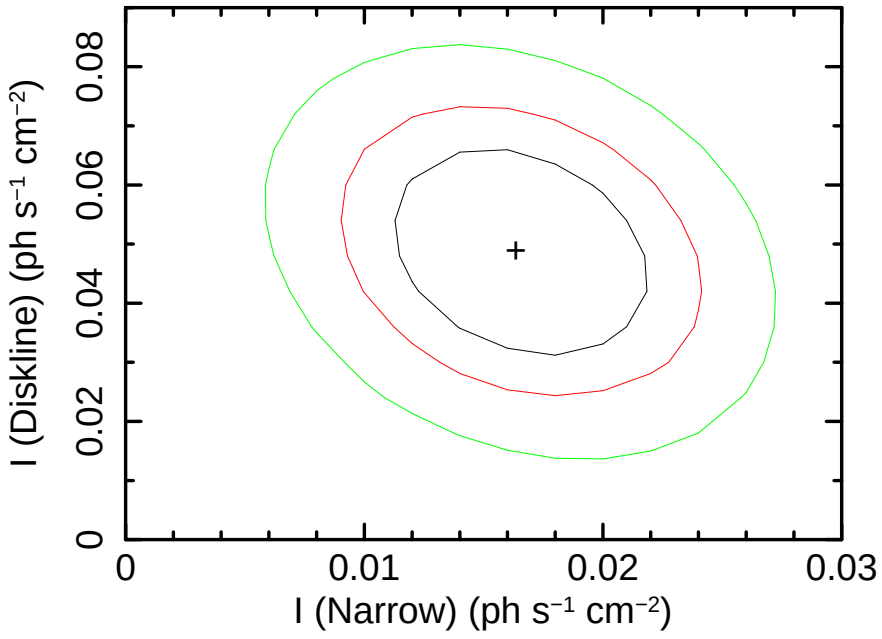

Figure 4.8: Contour plots (68%, 90% and 99%) of the `diskline` versus narrow component intensities for the "averaged X-ray spectrum". A simple power law is used to model the underlying continuum. The cross indicates the best fit values.

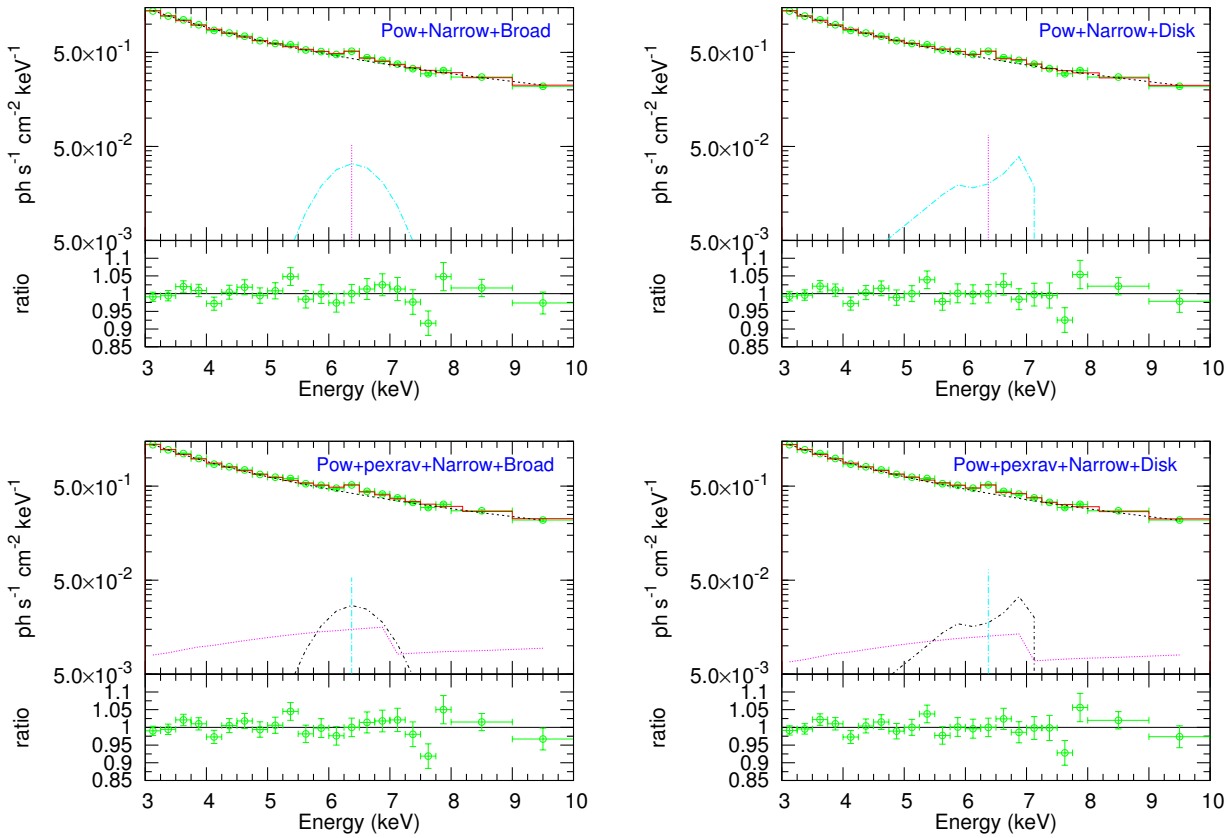

Figure 4.9: *Top panels* in each figure show spectral fit to the "averaged X-ray spectrum" using the quoted model. In the *bottom panels* ratio with respect to the quoted model is shown. The model components are also displayed.

EW = 37 ± 8 eV, diskline EW = 128 ± 36 eV and the disk inclination i = 44.4 ± 2.4 degrees. The `diskline` is detected at a robust significance level ($\Delta\chi^2 \sim 14$ for two additional parameters). Figure 4.8 shows contours (at 68%, 90% and 99% confidence interval) of the `diskline` versus narrow component intensities together with the best fit values derived for this fit (`mo pow+gaussian+diskline`) to the "averaged X-ray spectrum".

The additional spectral fits with a simple power law and the reflection component (modeled with `pexrav`), and two line components also give fit parameters fully consistent with those measured in the "averaged ratio flux spectrum" fitting, as shown in Table 4.2. Also in this case, a strong dependence of the broad line significance on the adopted continuum parametrization is present.

4.4.3 Complex fits

We next examine the implications of using a self-consistent reflection spectrum on the broad line detection significance and its measured parameters. We employed the neutral reflection model of Nandra et al. (2007). This model, known as `pexmon`, enables modeling of the iron lines and Compton reflection continuum in a self-consistent manner. In addition, the model includes a neutral Fe Kβ line (7.05 keV) with a flux of 11.3% of the Fe Kα line, a Ni Kα with 5% of the flux and the Fe Kα Compton shoulder.

Fitting the "averaged ratio flux spectrum" with a power law and a distant neutral reflector (`pexmon`) yielded an acceptable fit ($\chi^2/dof = 33.6/20$). However, the fit leaves residuals around the Fe core indicative of the presence of a broad component. When this residual feature is modeled with a `diskline` with parameters shown in Table 4.3, the fit improves significantly ($\Delta\chi^2 \sim 11.0$). The disk inclination is constrained to be $37.9^{+7.6}_{-2.8}$ degrees, while the `diskline` EW is 89^{+50}_{-38} eV. We determined the reflection fraction $R_{Dist} = 0.28 \pm 0.06$ for the reflector. The *top panel* of Fig.4.10 shows the spectral fit (`mo pow+pexmon+diskline`) to the "averaged ratio flux spectrum". The residuals (with the `pexmon` and `diskline` normalizations set to zero for the sake of illustration) are shown in the *bottom panel*.

The broad residual feature was also parametrized using an emission line profile from an accretion disk around a maximally rotating black hole (`laor`, Laor 1991). The peak energy, E_{Disk} was fixed at 6.4 keV, while the inner disk radius, R_{in} and outer disk radius, R_{out}, were kept at the default values of 1.24 and 400 R_g, respectively, where R_g is the gravitational radius. The emissivity index, β, was fixed to 2.5. The disk inclination to the observer, i, and the line normalization were allowed to vary. This spectral characterization (`mo pow+pexmon+laor`) yielded an acceptable fit ($\chi^2/dof = 22.1/18$) and we recovered the `laor` line EW = 112^{+50}_{-47} eV, the disk inclination $i = 43.9^{+3.7}_{-6.1}$ degrees and the reflection fraction $R_{Dist} = 0.26 \pm 0.05$ for the reflector. The fit results are presented in Table 4.3. We note that the parameters of the illuminating power law continuum (e.g. photon index Γ and normalization) and `pexmon` (e.g. photon index Γ, cutoff energy, Fe abundance, normalization and the derivation of the reflection fraction R_{Dist} etc.) were treated as in the `pexrav` fits, with the only difference of inclination of the `pexmon` now fixed to 60 degrees.

To model the broad feature self-consistently, we assumed that the accretion disk is in a low state of ionization and refitted the "averaged ratio flux spectrum" by replacing the `laor` line with a blurred reflection component. We do this by convolving the `pexmon` model with `kdblur`, a convolution model to smooth a spectrum by relativistic effects from an accretion disk around a rotating black hole (Fabian et al. 2002). The inner radius of the blurred reflector (accretion disk) was fixed to $R_{in} = 6\ R_g$, whereas the outer radius, R_{out}, and the emissivity index, β, were fixed at 100.0 R_g and 3.0, respectively. The free parameters were the normalizations of both the reflectors (`pexmon` and `kdblur*pexmon`) and the inclination, i, of the blurred reflector. The average parameters for this model are presented in Table 4.3. We find that the blurred reflector covers a solid angle ($2\pi \times R_{Blur}$) of $(0.80 \pm 0.24)\ \pi$ at the X-ray source, while the distant neutral reflector subtends a solid angle of ($2\pi \times R_{Dist}$) of $(0.54 \pm 0.12)\ \pi$ at the X-ray source. The average inclination derived for the blurred reflection component is $38.8^{+6.2}_{-4.9}$ degrees. In the *top panel* of Fig. 4.11 we display the spectral fit to the "averaged ratio flux spectrum" using a power law and

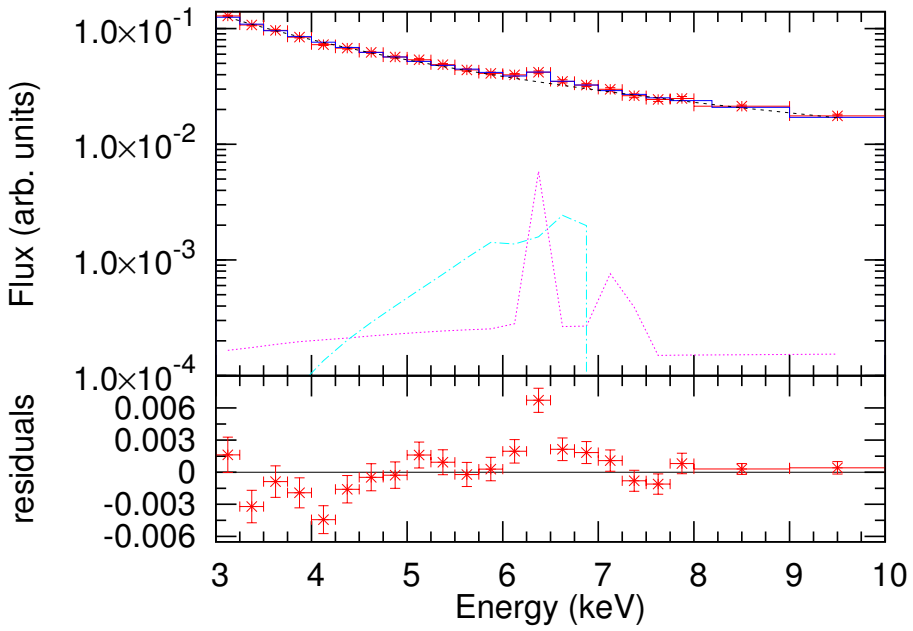

Figure 4.10: *Top panel* shows spectral fit to the "averaged ratio flux spectrum" using a model including a power law, a distant neutral reflector and a diskline (`mo pow+pexmon+diskline`) along with the model components. Residuals (with the `pexmon` and `diskline` normalizations set to zero for illustration purposes) are shown in the *bottom panel*.

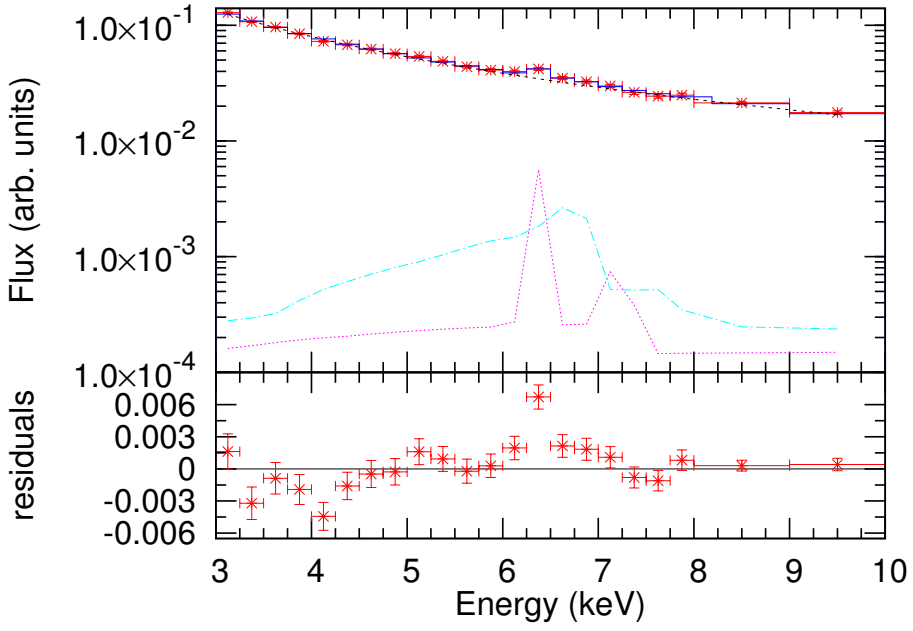

Figure 4.11: *Top panel* shows spectral fit to the "averaged ratio flux spectrum" using a power law and dual reflection spectra (`mo pow+pexmon+kdblur*pexmon`) along with the model components. Residuals (with the normalizations of both the reflectors set to zero for illustration purposes) are shown in the *bottom panel*.

the dual reflection spectra. The residuals (with the normalizations of both the reflectors set to zero for illustration purposes) are shown in the *bottom panel*.

Considering that the inner accretion disk is likely to be ionized, we then attempted to model the broad Fe K feature of the "averaged ratio flux spectrum" using the blurred ionized reflection component. For doing this, we convolved the ionized reflection model (denoted by `reflionx` in `XSPEC`[3]) of Ross & Fabian (2005) with `kdblur`. The incident power law photon index of the `reflionx` model was set equal to that of the primary power law component and the Fe abundance was fixed to 1. The ionization parameter and the normalization of the `reflionx` were allowed to vary. The other model components such as the power law, `pexmon` and `kdblur` etc. were set as in the previous fits.

This model (`mo pow+pexmon+kdblur*reflionx`) also produced a reasonably good fit with (χ^2/dof = 23.5/17). However, the ξ of the ionized reflector could not be constrained and we inferred an upper limit of 560 erg cm s^{-1} at 68 %. We outline the fact that the `reflionx` model does not include a formal parameter for the reflection fraction of the accretion disk and provides only the normalization of the `reflionx` component. Our measured value of the `reflionx` normalization is $(8.2^{+2.5}_{-7.6}) \times 10^{-4}$. We find that the parameters for the power law, distant reflector represented by `pexmon` and `kdblur` components are fully consistent with those obtained in the fit including the blurred neutral reflection component. The fit results are reported in Table 4.3.

In the next fits, we replaced the `kdblur` component with the `kerrconv` relativistic convolution model of Brenneman & Reynolds (2006) and investigated the variation in the fit parameters for the model comprising dual neutral reflection components. The `kerrconv` model consists of seven parameters: the emissivity indices for the inner and outer disk separated by a break radius, inner and outer radii for the disk emission, the spin parameter of the black hole and the inclination angle of the disk with respect to our line of sight. For the `kerrconv` component, we assumed a single emissivity index of 3. The black hole spin was fixed to 0, while the inclination angle of the disk was kept as a free parameter. We further fixed the inner radius of the disk to be equal to the radius of the marginally stable orbit, R_{ms}(= 6 R_g for a non-rotating black hole), and the outer radius to 400 R_{ms}. The best-fitting parameters for this model (`mo pow+pexmon+kerrconv*pexmon`) are given in Table 4.3. We report that the fit statistic as well as the fit parameters resulted from this model are in excellent agreement with those found in the fit using `kdblur` convolution model. A similar parametrization is obtained when the black hole spin is fixed to 0.998.

All the above discussed complex spectral models were also applied to the "averaged X-ray spectrum". The fit parameters retrieved from the "averaged X-ray spectrum" spectral fitting are summarized in Table 4.3. It can be seen that despite the slightly different underlying continuum of the "averaged X-ray spectrum", the parameters are fully consistent with those measured from the "averaged ratio flux spectrum". For illustration purposes, two spectral fits to the "averaged X-ray spectrum" are displayed in Fig. 4.12. The *top panel* plots spectral fit using a model including a power law, a distant neutral reflector and a `diskline` (`mo`

[3] In this model, an optically thick accretion disk is illuminated by a power law, producing fluorescence emission lines and the reflected continuum. The parameters of the `reflionx` model include the incident power law photon index Γ, Fe abundance and ionization parameter ξ, defined as $\xi = 4\pi F_{Tot}/n_H$, where F_{Tot} is the total illuminating flux and n_H is the density of the reflector.

pow+pexmon+diskline), while the *bottom panel* shows the fit using a power law plus dual reflection spectra (mo pow+pexmon+kdblur∗pexmon).

Finally, considering that the broad line EW or equivalently the reflection fraction of the blurred reflector, R_{Blur}, is the critical parameter of our work and many fit parameters (e.g. cutoff energy of the primary power law, Fe abundance, emissivity index, inner and outer radius of the disk etc.) were fixed in our spectral analysis, we investigated the effects of relaxing these fixed parameters on the inferred value of the R_{Blur}. We refitted the data by allowing the fixed parameters to vary one by one. We find that the R_{Blur} parameter measured from these new spectral fits is fully consistent with the values reported in Table 4.3. Based on this parameter space exploration, we can safely conclude that the R_{Blur} parameter determined from our data is <1.5 at the 5 sigma level.

4.5 Discussion

It is critical to have multiple independent methods to measure the average Fe Kα line properties. We have determined the Fe line parameters using two methods described in Section 4.3. We find that the average narrow core EW for the whole sample comprising 248 AGNs is ∼30 eV and is stable in various continuum models employed for the "averaged ratio flux spectrum" and "averaged X-ray spectrum" (Tables 4.1 and 4.2). We have demonstrated that the broad line parameters and its detection significance are highly sensitive to the adopted continuum modeling.

In order to examine the average Fe line properties as a function of the hard X-ray luminosity (2–10 keV) and also to investigate the variation in the line parameters obtained from the two methods we splitted the sample in 3 luminosity intervals (L1, $41 \leq logL_X \leq 43.5$ erg s^{-1}; L2, $43.5 < logL_X \leq 44.5$ erg s^{-1}; L3, $44.5 < logL_X \leq 46.0$ erg s^{-1}). We then computed the "averaged ratio flux spectra" from the averaged ratios and "averaged X-spectra" in these luminosity bins and performed their spectral analysis. Fig. 4.13 plots the narrow Fe Kα EWs measured from the spectral fitting of the "averaged ratio flux spectrum" (red) and "averaged X-ray spectrum" (green) against the X-ray luminosity in the 2–10 keV band for the whole sample of 248 AGNs (horizontal lines) and its sub-samples used for luminosity bins. An excellent agreement between the narrow line EWs determined from the two independent methods is evident. The narrow line EW decreases as the X-ray luminosity increases, a trend designated as the "X-ray Baldwin effect" or "Iwasawa-Taniguchi effect", first reported by Iwasawa & Taniguchi (1993). We do not concentrate on quantifying the X-ray luminosity dependence of the narrow line EW as it has been discussed in our previous work (see Chapter 3). However, we point out that the narrow line EWs derived in the rest-frame are consistent with the ones measured in the observed-frame. The neutral, narrow Fe Kα fluorescent emission line, peaking at 6.4 keV is reported to be a common and dominant feature in the X-ray spectra of local and distant AGNs (Yaqoob & Padmanabhan 2004; Nandra et al. 2007; Shu et al. 2010; Corral et al. 2008; Chaudhary et al. 2010). Our analysis further confirms this important finding.

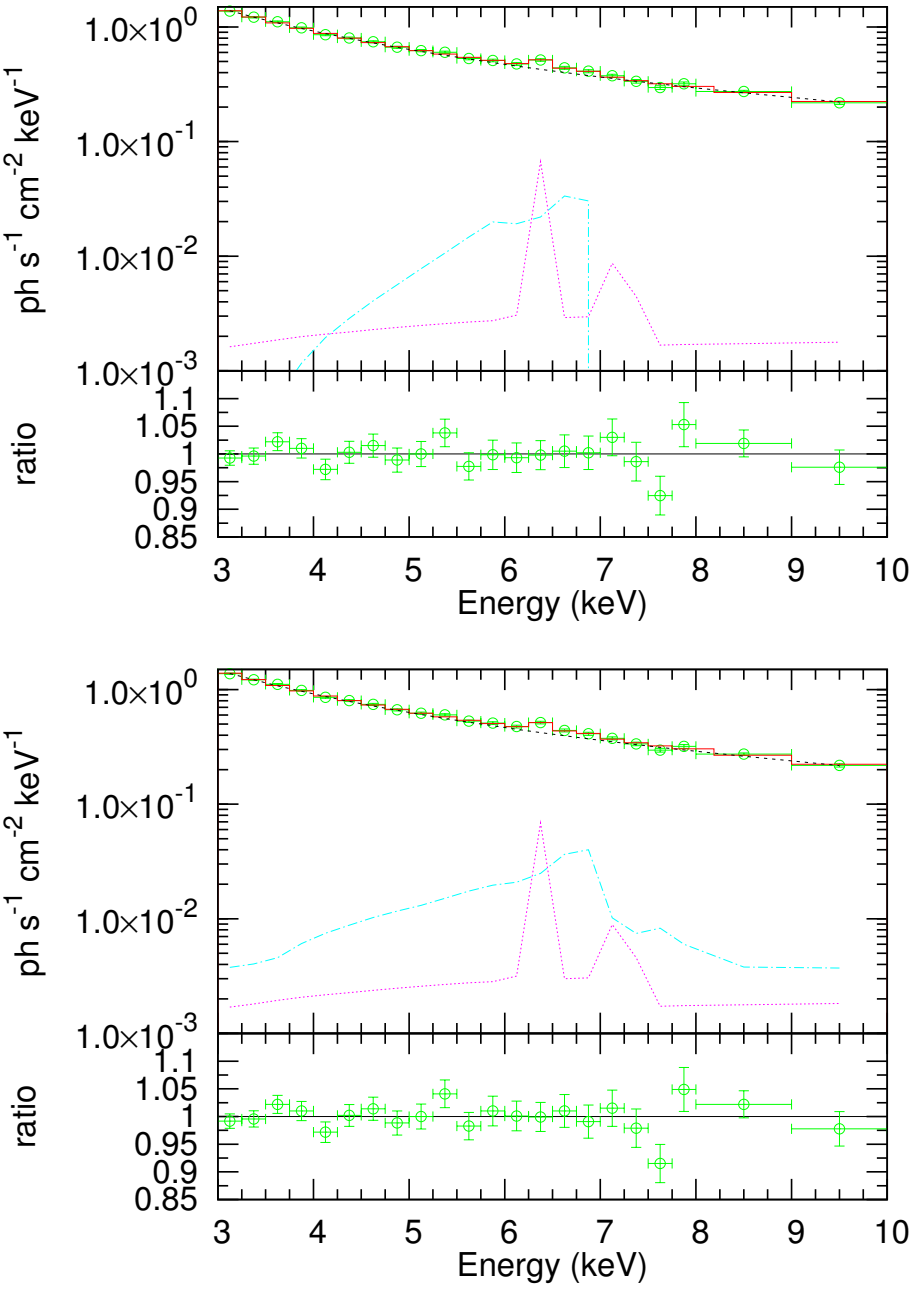

Figure 4.12: *Top panel* shows spectral fit to the "averaged X-ray spectrum" using a model including a power law, a distant neutral reflector and a diskline (mo pow+pexmon+diskline). *Bottom panel* displays the spectral fit including a power law and dual reflector spectra (mo pow+pexmon+kdblur∗pexmon). In both figures the *bottom panels* show respective data/model ratios.

Table 4.1: Results of the "averaged ratio flux spectrum" spectral fitting in the 3–10 keV

Model	Power law/pexrav				Gaussian			Diskline						
	Γ	$foldE$ (keV)	R_{Dist} ($\Omega/2\pi$)	$cosi$	$E_{K\alpha}$ (keV)	$\sigma_{K\alpha}$ (keV)	$EW_{K\alpha}$ (eV)	E_{Disk} (keV)	R_{in} (R_g)	R_{out} (R_g)	β	i (deg)	EW (eV)	χ^2/dof
Pow + Narrow	1.76 ± 0.02	...	...	...	6.40^*	0.01^*	45 ± 13	...	...	...	...	...	...	31.3/19
Pow + Broad	1.77 ± 0.02	...	...	...	6.40^*	$0.15^{+0.06}_{-0.04}$	75 ± 40	...	...	...	...	...	...	25.6/18
Pow + Disk	1.78^n	...	...	...	...	...	...	6.40^*	6.0^*	100.0^*	-2.5^*	35.3^n	128 ± 41	41.6/18
Pow + Narrow + Broad	1.78 ± 0.02	...	...	...	6.40^*	0.01^*	28 ± 20	...	...	...	...	...	...	
	...	...	...	...	6.40^*	$0.40^{+0.25}_{-0.14}$	73 ± 43	...	...	...	...	...	...	22.8/17
Pow + Narrow + Disk	1.78 ± 0.02	...	...	...	6.40^*	0.01^*	39 ± 14	6.40^*	6.0^*	100.0^*	-2.5^*	$44.6^{+3.0}_{-8.4}$	102^{+49}_{-55}	22.7/17
Pow + pexrav + Narrow + Broad	1.8^*	200^*	0.27 ± 0.17	0.9^*	6.40^*	0.01^*	28 ± 20	...	...	...	...	...	...	
	...	...	...	...	6.40^*	$0.37^{+0.31}_{-0.20}$	<105	...	...	...	...	...	...	21.6/17
Pow + pexrav + Narrow + Disk	1.8^*	200^*	0.24 ± 0.17	0.9^*	6.40^*	0.01^*	37 ± 14	6.40^*	6.0^*	100.0^*	-2.5^*	45.5 ± 3.5	<137	21.5/17

Notes: All errors and upper limits refer to the 68% confidence range for a single parameter.
In all the spectral fits, the errors in the Fe lines EW are calculated using `XSPEC` *eqw with err option*.
* denotes fixed parameter.
^{n} Error calculation is not possible due to poor fit.

Table 4.2: Results of the "averaged X-ray spectrum" spectral fitting in the 3–10 keV

Model	Power law/pexrav				Gaussian			Diskline						
	Γ	$foldE$ (keV)	R_{Dist} ($\Omega/2\pi$)	$cosi$	$E_{K\alpha}$ (keV)	$\sigma_{K\alpha}$ (keV)	$EW_{K\alpha}$ (eV)	E_{Disk} (keV)	R_{in} (R_g)	R_{out} (R_g)	β	i (deg)	EW (eV)	χ^2/dof
Pow + Narrow + Broad	1.64 ± 0.02	...	...	...	6.40^*	0.01^*	28 ± 10	...	...	...	...	...	...	
	...	...	...	...	6.40^*	$0.49^{+0.22}_{-0.14}$	92 ± 35	...	...	...	...	...	...	20.6/17
Pow + Narrow + Disk	1.64 ± 0.02	...	...	...	6.40^*	0.01^*	37 ± 8	6.40^*	6.0^*	100.0^*	-2.5^*	44.4 ± 2.4	128 ± 36	17.4/17
Pow + pexrav + Narrow + Broad	1.67^*	200^*	0.29 ± 0.18	0.9^*	6.40^*	0.01^*	29 ± 10	...	...	...	...	...	...	
	...	...	...	...	6.40^*	$0.52^{+0.29}_{-0.18}$	78 ± 40	...	...	...	...	...	...	20.2/17
Pow + pexrav + Narrow + Disk	1.67^*	200^*	0.25 ± 0.17	0.9^*	6.40^*	0.01^*	36 ± 8	6.40^*	6.0^*	100.0^*	-2.5^*	$45.1^{+3.8}_{-2.3}$	114 ± 41	17.4/17

All errors and upper limits are quoted at the 68% confidence range for a single parameter.
In all the spectral fits, the errors in the Fe lines EW are calculated using `XSPEC` *eqw with err option*.
* denotes fixed parameter.

Table 4.3: Results of the "averaged ratio flux spectrum" and "averaged X-ray spectrum" spectral fitting in the 3–10 keV using complex models

Model	Power law	Distant Reflector			Diskline/Blurred Reflector							
	Γ	$foldE$ (keV)	R_{Dist} ($\Omega/2\pi$)	i (deg)	E_{Disk} (keV)	R_{in} (R_g)	R_{out} (R_g)	β	i (deg)	EW (eV)	R_{Blur} ($\Omega/2\pi$)	χ^2/dof
"averaged ratio flux spectrum"												
Pow + pexmon + Disk	1.8^*	200^*	0.28 ± 0.06	60.0^*	6.40^*	6.0^*	100.0^*	-2.5^*	$37.9^{+7.6}_{-2.8}$	89^{+50}_{-38}	...	22.7/18
Pow + pexmon + Laor	1.8^*	200^*	0.26 ± 0.05	60.0^*	6.40^*	1.24^*	400.0^*	2.5^*	$43.9^{+3.7}_{-6.1}$	112^{+50}_{-47}	...	22.1/18
Pow + pexmon + kdblur∗pexmon	1.8^*	200^*	0.27 ± 0.06	60.0^*	...	6.0^*	100.0^*	3.0^*	$38.8^{+6.2}_{-4.9}$	...	0.40 ± 0.12	22.9/18
Pow + pexmon + kdblur∗reflionx	1.8^*	200^*	0.27 ± 0.06	60.0^*	...	6.0^*	400.0^*	3.0^*	$39.7^{+5.9}_{-7.1}$	...	...	23.5/17
Pow + pexmon + kerrconv∗pexmon	1.8^*	200^*	0.27 ± 0.06	60.0^*	...	6.0^*	2400.0^*	3.0^*	$43.9^{+2.8}_{-8.4}$	...	0.40 ± 0.12	23.1/18
"averaged X-ray spectrum"												
Pow + pexmon + Disk	1.65 ± 0.02	200^*	0.24 ± 0.06	60.0^*	6.40^*	6.0^*	100.0^*	-2.5^*	$38.5^{+6.8}_{-2.4}$	102^{+35}_{-28}	...	17.5/17
Pow + pexmon + Laor	1.65 ± 0.02	200^*	0.23 ± 0.06	60.0^*	6.40^*	1.24^*	400.0^*	2.7 ± 0.6	$43.9^{+3.3}_{-4.0}$	167^{+48}_{-61}	...	16.6/16
Pow + pexmon + kdblur∗pexmon	1.67 ± 0.02	200^*	0.25 ± 0.06	60.0^*	...	6.0^*	100.0^*	3.0^*	40.8 ± 4.1	...	0.49 ± 0.15	18.6/17
Pow + pexmon + kdblur∗reflionx	1.67 ± 0.06	200^*	0.27 ± 0.07	60.0^*	...	1.24^*	400.0^*	3.0^*	$33.8^{+4.9}_{-5.3}$	...	...	18.8/16
Pow + pexmon + kerrconv∗pexmon	1.66 ± 0.02	200^*	0.24 ± 0.05	60.0^*	...	6.0^*	2400.0^*	3.0^*	$43.8^{+2.6}_{-6.0}$	...	0.50 ± 0.16	18.3/17

Notes: All errors and upper limits refer to the 68% confidence range for a single parameter.
In all the spectral fits, the errors in the Fe lines EW are calculated using `XSPEC` *eqw with err option*.
In the fits including `kerrconv` component, the black hole spin is fixed to 0.
* denotes fixed parameter.

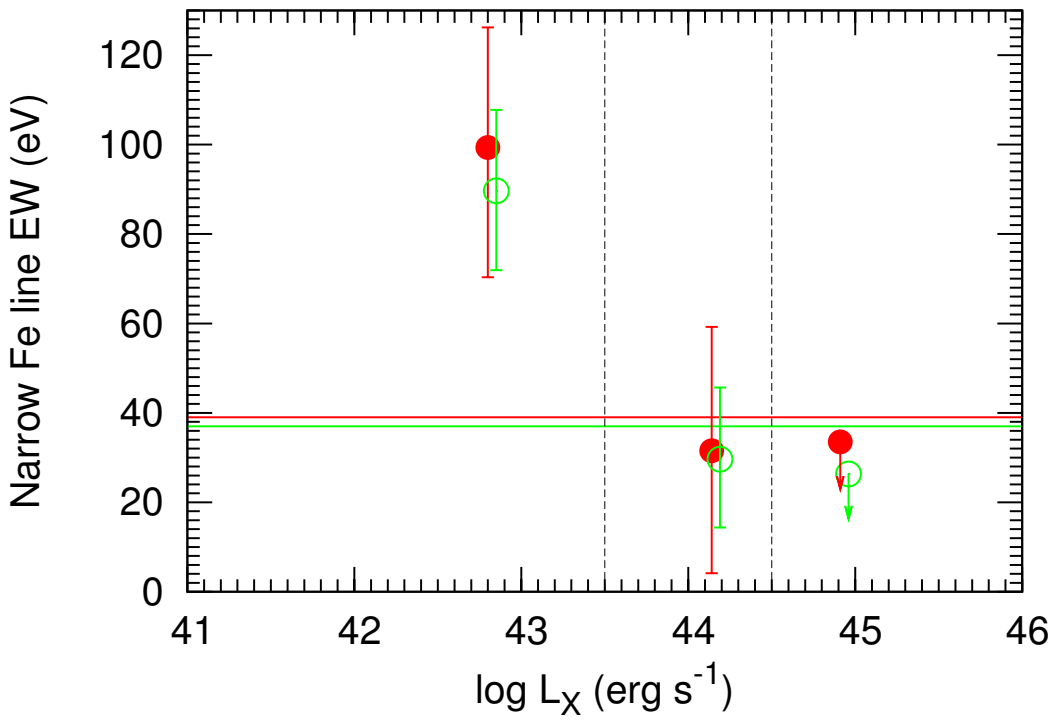

Figure 4.13: Equivalent width of the narrow Fe Kα line measured from the spectral fitting (`mo pow+gaussian+diskline`) of the "averaged ratio flux spectrum" (red) and "averaged X-ray spectrum" (green) of the total sample comprising 248 AGNs (horizontal lines) and the sub-samples used in 3 hard X-ray luminosity bins illustrated by the dotted vertical lines. The EW is plotted against the median luminosity in each bin. Errors and upper limits are drawn at the 68% confidence level.

When the broad line parameters such as its shape, EW and its detection significance in the "averaged ratio flux spectrum" and "averaged X-ray spectrum" of the total sample of 248 AGNs are considered, we notice that these parameters are dependent on the assumed continuum and adopted stacking method as illustrated in Fig. 4.14. In particular, despite having a well- defined sample with reasonable statistics (net counts ~198000) in the "averaged X-ray spectrum", we do not detect a clear extended red-wing, and the measured EW of the broad feature is always lower than 170 eV, in a good agreement with the recent studies of the average Fe K emission from AGNs (Guainazzi et al. 2006a; Corral et al. 2008; Longinotti et al. 2008).

Our derived broad line EW is significantly lower than the ~500 eV reported in the stacked spectrum of AGNs in the Lockman Hole (Streblyanska et al. 2005, hereafter S05). We briefly discuss possible causes for the difference. Considering that the fluorescent line profile originating from an accretion disk is a strong function of the disk ionization state (Fabian et al. 2000) and hence of the X-ray luminosity, we first investigated if the observed discrepancy in the Fe K line EW is caused by the different luminosity distribution of the two samples. The luminosities of the

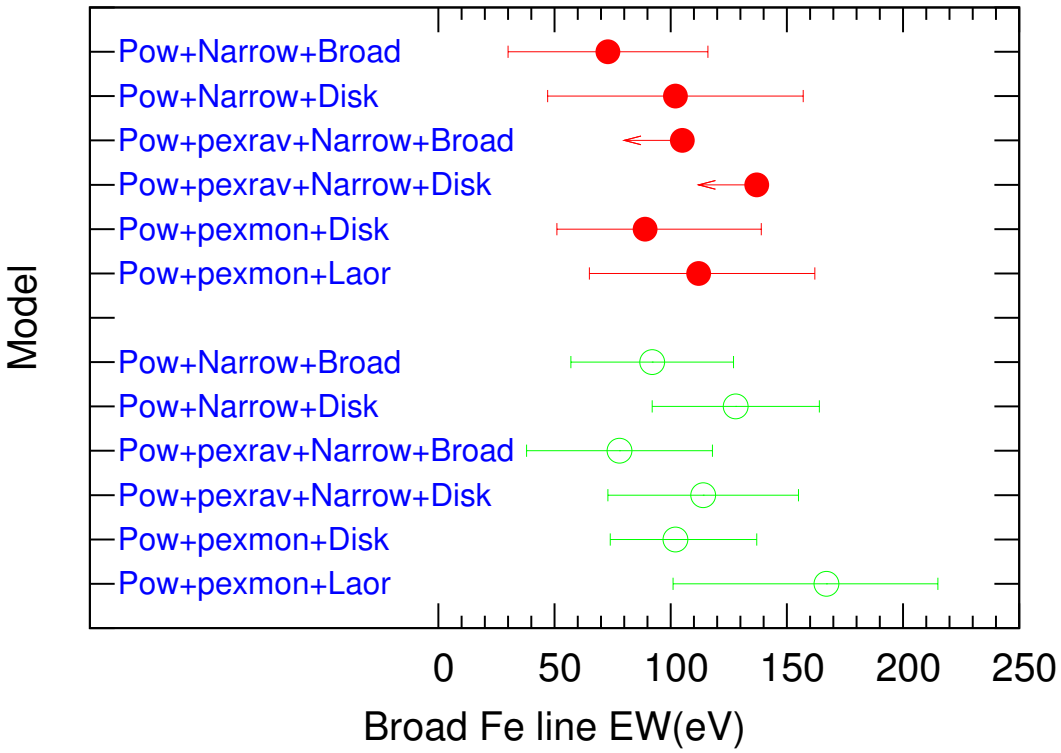

Figure 4.14: Comparison of the equivalent width of the broad Fe Kα line measured from the spectral fitting of the "averaged ratio flux spectrum (red) and "averaged X-ray spectrum" (green) of the total sample comprising 248 AGNs. Respective deterministic model is listed in blue. Errors and upper limits are drawn at the 68% confidence level.

Lockman Hole sample were taken from Mainieri et al. (2002). The 2–10 keV X-ray luminosity distributions of 53 Type 1 and 41 Type 2 AGNs used in S05 are very similar, with the mean luminosity of $10^{44.0}$ erg s^{-1}. The mean 2–10 keV X-ray luminosity of our sample is $10^{44.2}$ erg s^{-1}. We conclude that the luminosity difference does not contribute to the difference of the line strengths. Our measured broad line EW determined from a simple power law continuum parametrization is much lower than the associated value derived in S05. This implies that the continuum modeling is also not the key parameter behind the discrepant results. The observed discrepancy is most likely due to the difference in the adopted averaging techniques.

We also performed complex fits presented in Section 4.4.3 by modeling the "averaged ratio flux spectrum" and "averaged X-ray spectrum" with dual reflection models (a distant reflector and a disk reflector) handling emission lines and the Compton reflection self-consistently. Two types of reflection models (i.e. neutral and ionized) were applied to the data. We stress that from the statistical viewpoint, in both the explored averaging procedures, all models including two line components or dual reflection spectra provide good description of the data. Interestingly, characterization of the distant reflector with the `pexmon` model results in a high detection significance of the observed broad feature as compared to the `pexrav`. Given the available data

quality and the well-known degeneracy of accretion disk parameters, we could not derive all fit parameters independently. However, we emphasize that we have explored the parameter space in detail by relaxing the fixed parameters one by one. We note that the measured parameters from these fits are fully consistent with the values listed in Table 4.3. Furthermore, the derived average parameters of the dual reflectors such as the solid angle covered by the reflectors at the X-ray source and the inclination etc. agree well with the average values reported in the local AGNs samples with high counting statistics (Nandra et al. 2007; de La Calle Pérez et al. 2010).

According to the detailed calculations of George & Fabian (1991), the predicted EW of the Fe Kα arising from a centrally illuminated cold disk is 130–140 eV for a continuum with Γ in the range 1.8–1.9 and an inclination of 40 degrees. Our observed mean `diskline` EW of ∼100 eV agrees well with the theoretical prediction. Our results are also consistent with predictions of the relativistic Fe Kα line intensities from the integrated spectra of AGNs presented by (Ballantyne 2010, see Figure 1). In particular, the measured broad line EW and accretion disk reflection fraction ($R_{Blur} \sim 0.5$) in our data are consistent with Ballantyne (2010) predictions, despite the slightly different assumptions on the relativistic profile for the line (`laor2` versus `diskline`).

4.6 Conclusions

To characterize the average Fe K emission properties of AGNs in the source rest-frame we selected 248 AGNs from our reference sample of 507 sources. We employed two independent rest-frame stacking procedures to construct the integrated spectrum of the 248 AGNs. To examine the average Fe line properties as a function of the hard X-ray luminosity (2–10 keV) and also to investigate the variation in the line parameters obtained from the two procedures we also splitted the sample of 248 sources in 3 luminosity intervals and computed the integrated spectra for each sub-sample. These integrated spectra were referred as the "averaged ratio flux spectrum" and "averaged X-ray spectrum". We carried out a detailed spectral analysis of these integrated spectra using various models comprising simple/complex continuum and iron Kα line components. We performed simulations to identify the artifacts possibly introduced by the stacking procedure. The main results are the following:

- The average Fe Kα line profile in our sample is best represented by a combination of a narrow and a broad line. The EW of the narrow component in the integrated spectrum of 248 AGNs is ∼30 eV and is stable in various continuum models applied for the "averaged ratio flux spectrum" and "averaged X-ray spectrum".

- The narrow Fe Kα EWs determined from the integrated spectra (computed from the two rest-frame stacking procedures) of the sub-samples used in 3 luminosity bins decrease with the increase in the hard (2–10 keV) X-ray luminosity. We note that both procedures give statistically consistent narrow line EWs.

- The broad line parameters such as its shape, EW and its detection significance in the "averaged ratio flux spectrum" and "averaged X-ray spectrum" of the 248 AGNs are observed to be very sensitive to the assumed continuum and adopted stacking method. However,

despite having a well-defined sample with reasonable statistics (net counts ∼198000) in the "averaged X-ray spectrum", we do not detect a clear extended red-wing, and the measured EW of the broad feature is always lower than 170 eV, implying that most black holes are not maximally rotating.

- The broad line equivalent width we obtained is consistent with the theoretical predictions (George & Fabian 1991; Ballantyne 2010) as well as with the recent studies of the average Fe Kα emission from AGNs (Guainazzi et al. 2006a; Corral et al. 2008; Longinotti et al. 2008), except of the Lockman Hole AGNs (Streblyanska et al. 2005). We attribute this discrepancy to the difference in the adopted stacking techniques.

- When the "averaged ratio flux spectrum" of the 248 AGNs is fitted with a power law and dual (distant and blurred) neutral reflection spectra, we find that the blurred reflector covers a solid angle of (0.80 ± 0.24) π at the X-ray source, while the distant neutral reflector subtends a solid angle of (0.54 ± 0.12) π at the X-ray source. The average inclination derived for the blurred reflection component is $38.8^{+6.2}_{-4.9}$ degrees. The "averaged X-ray spectrum" spectral fitting also yields a similar parametrization for the reflectors. These parameters are in good agreement with the average values reported in the local AGNs samples with high counting statistics (Nandra et al. 2007; de La Calle Pérez et al. 2010).

Chapter 5

Summary and future perspectives

In this thesis I worked on characterizing the properties of the integrated spectrum of AGNs, such as the ubiquity of the Fe Kα emission line in distant AGNs, the dependence of the spectral parameters (e.g. the power law photon index and the Fe Kα equivalent width etc.) on the X-ray luminosity and redshift, and mean properties of the Fe Kα line in the source rest-frame. The final sample used in this work consists of 507 AGNs observed with XMM-*Newton* at high galactic latitude ($|BII| > 25$ degrees), with the sum of the EPIC-PN and EPIC-MOS 0.2–12 keV counts greater than 1000 and covering the redshift range $0 < z < 5$. One key advantage of this sample is that it includes higher statistics (approaching ~200000 counts, among the highest ever reported in literature for stacking studies) covering a wide range of luminosities at various redshifts, which allowed us to address the separate redshift and luminosity dependences of the spectral parameters. I employed two different rest-frame stacking procedures to construct the integrated spectrum of a sub-sample of 248 AGNs. I carried out a detailed spectral analysis of these integrated spectra using various models comprising simple/complex continuum and Fe Kα line components. I also verified the accuracy of our adopted stacking procedures by performing simulations in various redshift and luminosity intervals.

The main results of this work can be summarized as follows.

- We find that the narrow Fe Kα line at 6.4 keV is significantly detected up to $z = 1$. This confirms that the narrow Fe Kα line is an almost ubiquitous feature in the X-ray spectra of AGNs at high redshifts.

- The equivalent width of the narrow Fe Kα line is nearly independent of redshift up to $z \sim 0.8$ with an average value of 101 ± 40 (rms dispersion) eV in the luminosity range $43.5 \leq logL_X \leq 44.5$. The non evolution of the Fe Kα line strength with redshift can be interpreted as a constant fraction of iron through the cosmic time, which in turn translates into a constant fraction of metals since $z \sim 0.8$, if iron is representative of metals. Studies of quasar elemental abundances (derived from broad optical emission lines) also reported a similar (non evolutionary) trend of metallicity with redshift up to $z \sim 4.5$ (Hamann et al. 2007). Although limited to lower z, our study extends the results of Hamann et al. (2007) to objects of more typical AGNs luminosities.

- We find compelling evidence for an anticorrelation between the narrow Fe Kα equivalent width and 2–10 keV rest-frame luminosity (the so called "Iwasawa-Taniguchi effect") across a wide redshift interval larger than probed in any previous study. The anticorrelation is characterized by the relation $\log(EW_{Fe}) = (1.66 \pm 0.09) + (-0.43 \pm 0.07)\log(L_{X,44})$, where EW_{Fe} is the rest-frame equivalent width of the neutral Fe Kα line in eV and $L_{X,44}$ is the 2–10 keV X-ray luminosity in units of 10^{44} erg s^{-1}. The slope of the anticorrelation we obtained is steeper than the value reported in previous studies (Iwasawa & Taniguchi 1993; Page et al. 2004; Bianchi et al. 2007), likely due to the difference in composition of the samples. The exact physical cause of the "Iwasawa-Taniguchi effect" is unknown, one promising explanation is a decline in the covering factor of the putative molecular torus (i.e. the solid angle subtended by the torus at the nucleus divided by 4π) as the luminosity increases.

- We find a hardening of the power law photon indices at low luminosities ($logL_X < 43$) in the redshift bin 0.0–0.2. This can be linked to the increased absorption by the torus due to its high covering factor at these luminosities. The trend also reflects the decrease of the fraction of the absorbed sources with the X-ray luminosity revealed from extensive works in hard X-ray surveys studies (Ueda et al. 2003; La Franca et al. 2005; Hasinger 2008).

- In the rest-frame analysis, we find that the average Fe Kα line profile in our sample is best represented by a combination of a narrow and a broad line. The equivalent width of the narrow component in the integrated spectrum of 248 AGNs is ~30 eV and is stable in various continuum models applied for both the integrated spectra computed from two rest-frame stacking procedures. This further confirms that the narrow Fe Kα emission line is a common feature in the X-ray spectra of AGNs.

- The broad line parameters such as its shape, equivalent width and its detection significance in both the integrated spectra are found to be very sensitive to the assumed continuum and adopted stacking method. However, despite having a well-defined sample with reasonable statistics (net counts ~200000) in the integrated spectrum, we do not detect a clear extended red-wing, and the measured equivalent width of the broad feature is always lower than 170 eV, implying that most black holes are not maximally rotating.

- The broad line equivalent width we obtained is consistent with the theoretical predictions (George & Fabian 1991; Ballantyne 2010) as well as with the recent studies of the average Fe Kα emission from AGNs (Guainazzi et al. 2006a; Corral et al. 2008; Longinotti et al. 2008), except of the Lockman Hole AGNs (Streblyanska et al. 2005). We attribute this discrepancy to the difference in the adopted stacking techniques.

- Considering that the Fe Kα line in AGNs results from Compton reflection (reprocessing of the primary power law continuum in the accretion disk or torus), we applied different reflection models to the integrated spectra in addition to the direct power law continuum. We find that, in both the explored rest-frame stacking procedures, the models including a power law and two reflection spectra (corresponding to Compton reflection from the

accretion disk and torus) provide good description of the data similar to that obtained in the spectral fits with two line components (narrow and broad).

- We find that the accretion disk reflector covers a solid angle of $(0.80 \pm 0.24)\,\pi$ at the X-ray source, while the distant neutral reflector (torus) subtends a solid angle of $(0.54 \pm 0.12)\,\pi$ at the X-ray source. The average inclination derived for the accretion disk is $38.8^{+6.2}_{-4.9}$ degrees. These parameters are in good agreement with the average values reported in the local AGNs samples with high counting statistics (Nandra et al. 2007; de La Calle Pérez et al. 2010).

5.1 Future perspectives

In future work we plan to improve the statistics on X-ray data by a factor of 2 by including MOS1 and MOS2 data from XMM-*Newton*. We also plan to substantially increase the sample size by selecting new sources from the most recent publicly available versions of the 2XMM catalog. We further plan to collect multiwavelength data for all the sources selected in this way and perform a detailed spectral analysis of these spectra in the whole 0.2–12 keV XMM-*Newton* band. The advantage of such an approach is twofold. First, it would allow a systematic study of the soft X-ray properties of (at least) bright low redshift AGNs in our sample as a function of the source physical properties (e.g. the hard X-ray luminosity, black hole mass and accretion rate etc.). Second, since our sample comprises a large number of objects covering a wide redshift range $0 < z < 5$, for high redshift ($z \simeq 1$) AGNs, there is a greater band pass in hard X-rays as this (>10 keV) part of the spectrum is redshifted into the XMM-*Newton* rest-frame. Therefore, in the high redshift objects, which have sufficient signal-to-noise ratio, it should be possible to constrain the higher-energy Compton reflection hump using XMM-*Newton* data. Furthermore, we aim to identify the radio-quiet and radio-loud (characterized by high radio-loudness parameter (R > 10), where R is the flux ratio at 4.85 GHz and 4400 Å) AGNs in our sample and probe the structure of the accretion disks in these source populations through the characterization of the Fe Kα line and Compton reflection hump.

The future of the Fe K line studies is bright. In the next years, most of the progress in understanding the physics of the accreting black holes via X-ray spectroscopy is likely to be made by the continuing operation of XMM-*Newton*, *Chandra*, *Swift* and *Suzaku*. Owing to its ability to provide high signal-to-noise ratio spectra with very high energy resolution in the Fe K band (thereby completely characterizing any low-velocity component of the Fe K line) and broad band coverage (constraining the continuum shape over a wide energy range), *Suzaku* in particular, can provide an important breakthrough in the area of AGN X-ray spectroscopy.

Appendix

A.1 Background normalization in XSPEC

Let's assume source spectral files to be combined are,

$$S_1_spec, S_2_spec, , , \text{and } S_n_spec,$$

and these files have the EXPOSURE values

$$X_1, X_2, , \text{ and } X_n,$$

and BACKSCAL values

$$Y_1, Y_2, , \text{ and } Y_n,$$

respectively. These spectral files should have the unit COUNTS (not COUNTS/sec).

Corresponding background files are

$$B_1_spec, B_2_spec, , \text{ and } B_n_spec,$$

which have the EXPOSURE values

$$X'_1, X'_2, , \text{ and } X'_n,$$

and BACKSCAL values

$$Y'_1, Y'_2, , \text{ and } Y'_n,$$

respectively.

When XSPEC subtracts the background spectrum from the source spectrum, XSPEC normalizes the background in the following way :

$$\frac{S_1_spec}{X_1} - \frac{Y_1}{Y'_1}\frac{B_1_spec}{X'_1},$$
$$\frac{S_2_spec}{X_2} - \frac{Y_2}{Y'_2}\frac{B_2_spec}{X'_2},$$
$$\ldots,$$
$$\frac{S_n_spec}{X_n} - \frac{Y_n}{Y'_n}\frac{B_n_spec}{X'_n}.$$

A.2 Observed-frame stacking procedure

We adopt the following procedure to compute the integrated spectrum in all redshift and their luminosity bins.

- **Step 1:** Spectral counts (source + background) of all objects are summed in the observed frame using FTOOLS routine mathpha.
  mathpha expr=@s1expr.txt units=C outfil=!S.fits ERRMETH = 'POISS-0' exposure = 'CALC' areascal='NULL' ncomments=0
  where "s1expr.txt" is an ascii file containing "S_1_spec + S_2_spec+, , +S_n_spec", each S_n_spec represent source spectral file.

- **Step 2:** An integrated background spectrum is constructed. When integrated source and background spectra are created using `mathpha`, a care is needed to ensure that the correct amount of background is subtracted by `XSPEC`. First, BACKSCAL and EXPOSURE values for all sources and their corresponding background spectra are retrieved from header of these fits files. Thereafter, background normalization coefficients (C_n) for each background spectrum and BACKSCAL factor for the integrated background spectrum ((BACKSCAL)$_{bgd}$) are derived using the following formulae[1]:

$$C_1 = \frac{X_1' + X_2' + , , + X_n'}{X_1(Y_1/Y_1') + X_2(Y_2/Y_2') + , , + X_n(Y_n/Y_n')} \left(\frac{X_1}{X_1'}\right)\left(\frac{Y_1}{Y_1'}\right)$$

$$C_2 = \frac{X_1' + X_2' + , , + X_n'}{X_1(Y_1/Y_1') + X_2(Y_2/Y_2') + , , + X_n(Y_n/Y_n')} \left(\frac{X_2}{X_2'}\right)\left(\frac{Y_2}{Y_2'}\right)$$

$$, , ,$$

$$C_n = \frac{X_1' + X_2' + , , + X_n'}{X_1(Y_1/Y_1') + X_2(Y_2/Y_2') + , , + X_n(Y_n/Y_n')} \left(\frac{X_n}{X_n'}\right)\left(\frac{Y_n}{Y_n'}\right)$$

$$(BACKSCAL)_{bgd} = \frac{X_1 + X_2 + , , + X_n}{X_1(Y_1/Y_1') + X_2(Y_2/Y_2') + , , + X_n(Y_n/Y_n')}$$

  where $X_1, X_2, , ..X_n$ and $Y_1, Y_2, , ..Y_n$ are the EXPOSURE and BACKSCAL values for the source files, while $X_1', X_2', , ..X_n'$ and $Y_1', Y_2', , ..Y_n'$ are the EXPOSURE and BACKSCAL values for the background files (e.g. $B_1_spec, B_2_spec, ,$ and B_n_spec).

  Then, the following commands
  mathpha expr=@b1expr.txt units=C outfil=!B.fits ERRMETH = 'POISS-0' exposure = 'CALC' areascal='NULL' ncomments=0
  where "b1expr.txt" is an ascii file containing
  "$C_1 * B_1_spec + C_2 * B_2_spec$+, , +$C_n * B_{n_spec}$".
  fparkey (BACKSCAL)$_{bgd}$ B.fits[1] BACKSCAL

[1] http:heasarc.gsfc.nasa.govdocsasca/bgd_scale/bgd_scale.html

(actual numerical values of C_1,C_2 and C_n and $(BACKSCAL)_{bgd}$ are used.)
have been used to create an integrated background spectrum (B.fits) with an EXPOSURE equal to that of the integrated source spectrum (S.fits).

- **Step 3:** In the last step, response and ancillary files for the integrated source spectrum were produced using FTOOLS routine addrmf[2] and addarf[3], respectively. EXPOSURE weighting factors were applied to each input response and ancillary files.

  addrmf @rmfin.txt rmffile=!R.rmf
  addarf @arfin.txt out_ARF=!A.arf

  where “rmfin.txt” and “arfin.txt” are ascii files with weights and names of the response and ancillary files.

[2] http://heasarc.gsfc.nasa.gov/lheasoft/ftools/caldb/addrmf.html
[3] http://heasarc.nasa.gov/ftools/caldb/addarf.html

A.3 The sample

This Table provides the basic information about our final sample of 507 AGNs observed with XMM-*Newton*. The columns are organized as follows: Column (1) the source name as in the 2XMM catalog; Col. (2) redshift obtained from the Nasa's Extragalactic Database; Cols. (3) and (4) EPIC-PN net source counts and flux in the observed-frame 0.2–12 keV band as in the 2XMM catalog; Col. (5) EPIC-PN net source counts in the rest-frame 2–10 keV band; Cols. (6) and (7) power law photon index (Γ) and X-ray luminosity derived from the spectral fitting of each spectrum in the rest-frame 2–10 keV band.

Table A.3: Properties of the final sample

IAUNAME	z	PN counts [0.2–12 keV]	Flux [0.2–12 keV]	PN counts [2–10 keV]	Γ	$logL_X$ [2–10 keV]
2XMM J120929.7+434106	0.002960	4889.42	6.778490e-12	3684	1.65	41.02
2XMM J124252.3+131526	0.003400	2872.59	9.864980e-13	466	1.71	40.08
2XMM J011127.5-380500	0.011756	1823.14	2.184060e-12	432	0.35	41.50
2XMM J033339.6-050522	0.013427	787.03	4.332210e-13	176	-0.20	40.95
2XMM J030349.0-010613	0.013587	1426.14	1.312970e-12	806	-0.24	41.46
2XMM J013331.1+354006	0.015156	939.90	4.009670e-13	141	0.71	40.73
2XMM J012531.4+320811	0.015526	7625.06	2.111980e-12	1898	1.57	41.82
2XMM J011607.1+330522	0.015935	852.00	2.310160e-13	78	4.11	40.47
2XMM J201958.9-523718	0.016083	652.27	5.800490e-13	151	1.70	41.30
2XMM J014357.7+022059	0.017167	3615.23	8.077990e-13	188	1.06	41.08
2XMM J015002.6-072548	0.017654	2809.65	1.305120e-12	872	2.49	41.74
2XMM J235126.7+203509	0.018470	849.61	1.732550e-13	86	2.16	40.62
2XMM J012426.7+334758	0.019530	3278.13	5.024200e-12	2193	1.55	42.51
2XMM J095219.1-013643	0.019930	876.12	1.824970e-12	83	4.15	41.78
2XMM J033040.9-030815	0.020440	730.31	5.229280e-13	176	3.04	41.54
2XMM J113914.8+170837	0.021190	2046.51	1.336990e-12	360	1.32	41.88
2XMM J120256.9-205602	0.021790	3928.02	3.808530e-13	1706	1.93	41.46
2XMM J121016.6+391817	0.022080	813.32	6.021760e-14	120	2.28	40.43
2XMM J121049.5+392822	0.022510	2094.44	4.342170e-13	312	1.64	41.32
2XMM J130200.1+274657	0.023580	2134.57	2.352650e-13	3	2.56	39.95
2XMM J140715.5-270928	0.024330	3437.45	4.415840e-13	356	1.81	41.34
2XMM J153547.7+732703	0.024530	1543.81	2.584320e-13	56	4.50	40.38
2XMM J025218.5-011746	0.024577	997.81	3.622950e-13	235	1.63	41.47
2XMM J113240.2+525701	0.026420	763.19	6.516650e-13	266	-0.55	41.69
2XMM J220702.0+101401	0.026647	1387.13	9.795860e-13	491	0.02	41.97
2XMM J003413.6-212618	0.026826	2947.48	7.800530e-13	450	1.79	41.78
2XMM J215656.6-113930	0.028070	834.19	5.295290e-13	111	0.96	41.63
2XMM J143450.5+033843	0.028650	2014.64	3.176070e-13	278	2.02	41.45
2XMM J232756.7+084645	0.028904	1251.05	1.037590e-12	313	0.44	41.98
2XMM J173456.2+680734	0.029100	1267.99	3.478470e-13	241	1.83	41.57
2XMM J024912.8-081525	0.029419	559.13	6.612630e-13	80	1.79	41.80
2XMM J160534.5+323941	0.029660	1491.24	3.062130e-13	195	2.19	41.31
2XMM J231815.6+001540	0.029793	385.33	4.926710e-13	70	2.31	41.69
2XMM J030030.5-112456	0.029873	959.80	1.282380e-12	284	0.10	42.19
2XMM J032525.3-060838	0.034490	5353.10	2.631370e-12	1016	1.58	42.60
2XMM J150121.1+013813	0.035300	688.24	1.968020e-13	239	1.59	41.54
2XMM J141721.0+265127	0.036510	604.38	7.705780e-14	40	1.68	40.78
2XMM J113409.0+491516	0.037260	809.01	1.254880e-12	430	2.31	42.33
2XMM J224030.2+032130	0.038610	2871.99	7.258510e-13	622	1.73	42.11
2XMM J093551.5+612111	0.039370	892.67	2.556410e-13	316	0.24	41.66
2XMM J044001.8-453409	0.039600	773.02	5.469620e-13	426	1.48	42.12
2XMM J155651.2+812856	0.040800	1008.79	8.788060e-13	151	2.17	42.19
2XMM J052101.4-252144	0.042560	3305.59	4.196050e-12	1883	2.02	43.12
2XMM J235113.9+201346	0.043530	2385.23	6.372900e-13	672	1.80	42.18
2XMM J033703.3-251456	0.043710	673.29	7.589750e-13	397	2.53	42.29
2XMM J021822.1-050614	0.044000	551.20	4.719000e-13	431	1.14	42.22
2XMM J231546.7-590314	0.044600	534.12	2.824200e-13	149	1.03	41.94

continued.

IAUNAME	z	PN counts [0.2–12 keV]	Flux [0.2–12 keV]	PN counts [2–10 keV]	Γ	$logL_X$ [2–10 keV]
2XMM J133117.4+292205	0.047930	1264.46	2.805820e-13	207	1.46	41.87
2XMM J103408.5+600152	0.050500	819.11	3.423860e-13	114	0.60	41.87
2XMM J011356.4-144239	0.054000	1084.23	5.685770e-13	457	2.06	42.41
2XMM J004311.5-093815	0.054210	851.13	5.882620e-13	123	1.79	42.29
2XMM J174838.1+684217	0.055900	2136.49	1.038110e-12	544	1.73	42.66
2XMM J200824.5-444009	0.058080	10312.10	1.605370e-12	1219	2.04	42.71
2XMM J083139.1+524205	0.058590	603.81	1.209460e-13	387	1.73	41.83
2XMM J010852.8+132015	0.059700	1592.81	3.249640e-12	959	-0.33	43.24
2XMM J112916.7-042407	0.060000	6319.85	1.558710e-12	3245	2.08	42.99
2XMM J094057.1+032401	0.060730	5212.54	1.264150e-12	502	1.92	42.58
2XMM J043516.1-780156	0.060980	4977.00	3.141920e-12	963	1.78	43.18
2XMM J193121.5-723920	0.063700	343.47	3.573030e-13	101	0.64	42.32
2XMM J132037.8+341126	0.063920	1224.56	4.162290e-13	346	2.47	42.33
2XMM J221712.2+141421	0.065760	4020.13	4.423110e-12	2029	1.79	43.53
2XMM J050550.3-675018	0.070000	994.59	7.448770e-13	522	2.08	42.80
2XMM J053444.6-673856	0.072000	3399.49	8.164410e-13	1257	1.97	42.77
2XMM J131130.6+315201	0.072860	4479.00	7.445640e-13	726	1.69	42.66
2XMM J134351.0+000435	0.073600	1849.62	2.788530e-13	131	2.04	42.06
2XMM J003543.5-273730	0.073660	564.27	3.699430e-13	63	1.65	42.36
2XMM J122349.6+072657	0.074740	1287.54	3.017820e-13	80	2.13	42.02
2XMM J140700.4+282714	0.076580	858.40	4.564700e-13	289	1.11	42.56
2XMM J100035.4+052428	0.078630	1764.90	8.249830e-13	225	2.16	42.65
2XMM J111443.5+525834	0.079210	885.48	9.726420e-13	39	3.11	42.59
2XMM J083737.0+254750	0.079400	857.15	1.328090e-12	220	1.36	43.13
2XMM J130005.5+163213	0.080000	367.25	2.839020e-12	244	1.77	43.49
2XMM J221918.5+120753	0.081350	20201.30	4.555340e-12	1169	2.56	43.20
2XMM J101843.1+413515	0.083860	656.96	2.065280e-13	124	1.74	42.27
2XMM J102147.8+131227	0.085110	7828.64	2.374520e-12	1729	1.76	43.33
2XMM J134700.9-113335	0.085830	899.53	5.191200e-13	204	1.23	42.65
2XMM J134245.8+403913	0.089040	604.16	5.553290e-13	423	2.06	42.84
2XMM J141348.3+440014	0.089600	3304.35	7.457930e-13	808	0.95	42.89
2XMM J133152.2+111649	0.090000	1700.68	2.461130e-12	725	1.58	43.50
2XMM J123625.4+125844	0.093230	996.33	5.370610e-13	452	1.88	42.74
2XMM J153152.3+241429	0.096000	1272.19	9.012300e-13	127	1.96	42.86
2XMM J140621.8+222347	0.098000	2039.47	9.533440e-13	49	1.67	42.33
2XMM J102348.4+040554	0.098870	2662.45	1.505880e-13	253	2.02	42.11
2XMM J111552.2+424330	0.100780	959.59	1.437100e-13	253	1.62	42.29
2XMM J121118.8+503653	0.102330	2658.17	1.269450e-12	1615	1.64	43.34
2XMM J013943.5-674908	0.104000	666.83	1.814050e-13	152	1.16	42.47
2XMM J042600.7-571201	0.104000	31011.10	1.202050e-11	8147	1.34	44.29
2XMM J135724.5+652506	0.106340	5321.60	8.975900e-13	481	2.03	42.93
2XMM J130845.7-013053	0.111330	750.00	5.516080e-13	89	1.83	42.87
2XMM J033851.6-352644	0.112350	1239.31	1.686690e-13	227	1.66	42.42
2XMM J135042.6-334311	0.113050	5967.12	1.654000e-12	1224	1.82	43.41
2XMM J151041.0+333505	0.114190	6668.88	3.164620e-12	939	2.09	43.63
2XMM J151741.6+424819	0.116260	760.15	3.391890e-13	113	1.59	42.63
2XMM J124828.4+083113	0.120000	1727.09	6.282560e-13	298	2.23	43.00
2XMM J004350.2+005750	0.126000	946.14	5.571490e-13	198	1.15	43.05
2XMM J151640.1-010212	0.128160	880.41	2.270510e-13	164	3.87	42.66
2XMM J095858.5+021459	0.132780	1423.41	4.893180e-13	288	1.38	42.96
2XMM J124219.8-112402	0.135790	614.34	1.127040e-13	123	3.81	42.30
2XMM J234648.0-021619	0.136740	1012.21	2.154970e-13	150	1.66	42.63
2XMM J161546.9-060028	0.140000	630.42	3.880680e-13	144	2.22	42.99
2XMM J003515.5-433357	0.143000	5780.92	1.202460e-12	385	2.27	43.10
2XMM J133141.0-015212	0.145670	3228.61	8.252010e-13	282	1.83	43.12
2XMM J052402.0-701108	0.151000	2784.14	2.063930e-12	742	1.73	43.81
2XMM J135435.6+180518	0.152000	23172.20	5.477880e-12	2278	2.09	44.06
2XMM J221719.0-354951	0.152700	1952.45	3.624830e-13	178	2.10	42.90
2XMM J094439.8+034940	0.155420	2436.56	7.177610e-13	327	1.95	43.26
2XMM J105144.3+353930	0.158770	1300.96	2.510490e-12	625	2.04	44.07
2XMM J031146.1-550700	0.162000	539.42	9.011720e-13	66	7.45	43.31

continued.

IAUNAME	z	PN counts [0.2–12 keV]	Flux [0.2–12 keV]	PN counts [2–10 keV]	Γ	$logL_X$ [2–10 keV]
2XMM J015950.2+002341	0.163010	5549.35	2.729830e-12	603	1.90	43.85
2XMM J014159.8-543039	0.168000	2928.36	1.000580e-12	568	1.59	43.57
2XMM J015234.8-134735	0.170000	973.67	1.677010e-13	180	3.16	42.79
2XMM J151600.9+000949	0.170960	4066.19	7.461620e-13	831	1.86	43.44
2XMM J003517.2-431121	0.175000	795.57	7.929040e-14	124	0.76	42.58
2XMM J003833.6-272640	0.176700	2390.03	6.948930e-13	431	2.16	43.40
2XMM J113129.2+310944	0.179910	1654.20	5.083270e-13	338	1.61	43.36
2XMM J105128.4+335850	0.182660	1666.75	4.493100e-13	471	2.21	43.34
2XMM J134054.4+262253	0.183000	866.71	3.413260e-13	151	1.60	43.13
2XMM J095456.3-202155	0.183700	1911.30	1.877430e-13	361	1.56	42.96
2XMM J104444.7-012018	0.184700	754.12	7.460400e-14	155	2.18	42.54
2XMM J130237.6-024055	0.184900	495.74	2.991750e-13	162	2.44	43.07
2XMM J093922.9+370942	0.185940	3274.62	1.268480e-12	198	2.29	43.43
2XMM J140251.2+263118	0.187000	1666.22	3.322820e-12	351	1.49	44.22
2XMM J020757.1+351828	0.188000	868.49	1.795050e-13	125	1.33	42.97
2XMM J100055.4-193115	0.188110	1106.37	1.510110e-12	514	1.79	43.85
2XMM J022452.1-040519	0.189000	1205.47	1.085300e-13	114	1.54	42.56
2XMM J215501.4-092223	0.190000	704.79	7.617370e-14	91	1.37	42.54
2XMM J123113.6+151128	0.191890	554.32	6.072300e-13	75	1.84	43.44
2XMM J023713.4-522734	0.193000	1411.05	6.779930e-13	183	1.58	43.69
2XMM J002005.2-254326	0.194900	733.59	4.764610e-13	181	1.46	43.38
2XMM J234449.5+122142	0.199000	888.39	8.131230e-13	297	1.87	43.76
2XMM J105421.1+572544	0.205000	9290.71	1.786630e-12	3047	1.84	44.06
2XMM J144414.6+063306	0.208050	19526.70	5.301390e-12	3291	1.76	44.47
2XMM J205635.6-044716	0.217000	683.28	3.709540e-13	131	2.74	43.27
2XMM J153228.8+045358	0.219000	5807.02	2.136630e-12	1120	1.93	44.06
2XMM J031155.2-765150	0.223000	32949.10	4.756280e-12	7459	1.63	44.50
2XMM J043944.8-454042	0.224000	6968.04	5.100980e-13	338	2.33	43.16
2XMM J111816.2+074316	0.225280	865.36	4.625520e-14	197	2.11	42.46
2XMM J153304.0+302508	0.227240	766.26	2.673750e-13	119	2.18	43.22
2XMM J072135.9+711322	0.232000	578.19	4.178550e-13	114	1.48	43.50
2XMM J205829.8-423634	0.232000	1292.76	6.701530e-13	360	2.00	43.67
2XMM J023042.6-011105	0.232380	870.87	5.615950e-13	167	1.70	43.58
2XMM J123305.8+001438	0.234500	4382.69	3.810960e-13	957	1.77	43.42
2XMM J101922.6+412050	0.238690	1928.33	4.774560e-13	342	1.68	43.49
2XMM J121007.8+392312	0.239000	702.65	1.470730e-13	159	2.81	42.98
2XMM J100726.0+124856	0.240820	2189.57	5.137670e-13	738	1.96	43.68
2XMM J130128.1+275106	0.243210	1248.05	5.403750e-13	103	1.96	43.45
2XMM J014612.6-392305	0.244000	25613.40	2.582460e-12	4896	1.79	44.31
2XMM J100150.8-193623	0.244480	722.14	1.470420e-12	99	2.13	43.96
2XMM J154316.4+540526	0.245250	1067.43	2.416780e-13	134	5.04	43.10
2XMM J145426.6+182956	0.247000	2956.00	4.079430e-13	298	2.21	43.33
2XMM J142325.4+384032	0.248930	1391.64	5.431190e-13	142	2.93	43.42
2XMM J140139.4+025721	0.249000	1143.14	1.796850e-13	182	1.75	43.17
2XMM J003739.4-333049	0.249500	744.35	1.847580e-13	202	1.78	43.10
2XMM J141658.3+521205	0.250000	726.62	1.073940e-13	68	2.41	42.58
2XMM J140145.0+025332	0.250600	783.95	3.131350e-13	376	2.21	43.42
2XMM J022438.9-042706	0.252000	1290.66	2.752230e-13	168	2.19	43.25
2XMM J123123.9+142124	0.255770	4339.61	2.358550e-12	468	3.13	44.33
2XMM J141531.4+113156	0.256000	3067.69	4.263790e-13	684	2.05	43.60
2XMM J095921.3+024030	0.259680	2016.70	2.010080e-13	151	2.71	43.02
2XMM J133441.8+380011	0.260000	616.31	6.194650e-14	132	2.53	42.78
2XMM J050923.5-672125	0.260000	658.31	1.240200e-13	168	1.95	43.05
2XMM J075216.4+500251	0.263080	736.29	8.149200e-13	141	1.66	43.84
2XMM J140127.6+025606	0.264560	4160.39	1.131650e-12	1573	1.99	44.12
2XMM J075204.7+362500	0.267950	781.13	1.907700e-12	72	1.31	44.12
2XMM J121613.5+524245	0.269600	1947.26	2.116170e-12	195	1.79	44.26
2XMM J111121.6+482047	0.280870	1039.06	4.683930e-13	296	2.17	43.66
2XMM J000031.8-245501	0.283000	640.04	1.995440e-13	91	2.48	43.24
2XMM J122018.4+064120	0.286360	4587.45	2.416710e-12	862	1.85	44.42
2XMM J093535.4+611920	0.287000	1441.98	1.597200e-13	228	0.72	43.20

continued.

IAUNAME	z	PN counts [0.2–12 keV]	Flux [0.2–12 keV]	PN counts [2–10 keV]	Γ	$logL_X$ [2–10 keV]
2XMM J130803.4+292909	0.288000	1028.02	1.302950e-13	228	1.78	43.20
2XMM J163309.5+571041	0.288000	667.60	4.307350e-13	62	2.10	43.64
2XMM J151547.5+561033	0.296000	862.39	2.243980e-13	107	1.94	43.26
2XMM J182446.5+650924	0.303000	685.71	1.014740e-12	109	2.64	44.05
2XMM J123126.4+105111	0.304060	4274.30	3.837870e-13	242	1.84	43.44
2XMM J132447.6+032431	0.305780	3395.27	1.299940e-12	643	2.10	44.16
2XMM J123752.7+621628	0.305930	1127.87	9.840580e-14	341	2.28	43.15
2XMM J033312.2-361946	0.308000	1105.35	2.276540e-12	134	2.83	44.27
2XMM J004319.7+005115	0.308100	11361.90	1.987950e-12	2328	1.72	44.43
2XMM J213216.8-425411	0.311000	4891.00	4.227720e-13	403	2.43	43.53
2XMM J015957.6+003310	0.311750	720.45	7.834310e-13	143	1.81	44.04
2XMM J110318.4+381544	0.314000	763.50	1.886270e-13	214	0.87	43.49
2XMM J231830.0-422041	0.316000	1616.08	8.190340e-14	415	2.19	43.11
2XMM J142455.5+421408	0.316030	2935.41	1.407220e-12	405	2.01	44.24
2XMM J121122.4+130936	0.324040	1004.80	8.376440e-13	204	1.37	44.13
2XMM J033720.8-345123	0.325270	793.01	1.034030e-13	226	1.50	43.28
2XMM J223607.6+134355	0.325870	4541.28	1.536540e-12	598	2.27	44.23
2XMM J015327.1-135225	0.326000	1829.97	3.484910e-13	280	1.39	43.92
2XMM J053600.4-704127	0.330000	1859.53	9.844190e-13	686	1.75	44.23
2XMM J134844.7-302943	0.330000	1447.08	1.484930e-12	197	3.16	44.46
2XMM J000027.6-250442	0.335000	999.03	1.601120e-13	213	2.50	43.36
2XMM J012433.1+034334	0.336000	1093.30	3.770930e-13	237	2.09	43.79
2XMM J141751.0+522311	0.350000	705.04	7.675930e-14	202	1.70	43.23
2XMM J141649.4+522531	0.350000	556.84	1.243180e-13	135	3.07	43.33
2XMM J143025.8+415957	0.352440	1211.90	3.541440e-13	277	1.91	43.84
2XMM J080608.0+244421	0.357970	2167.23	5.701310e-13	323	3.59	43.89
2XMM J173707.8+660103	0.358000	2202.20	5.058210e-13	739	1.49	44.05
2XMM J020011.5-093125	0.360530	682.81	8.420040e-13	205	1.88	44.16
2XMM J100043.1+020637	0.360600	729.83	1.258980e-13	134	2.87	43.28
2XMM J080711.0+390419	0.368550	886.71	7.608150e-13	188	1.85	44.13
2XMM J123356.1+074755	0.370990	3605.73	7.228920e-13	740	1.62	44.17
2XMM J100025.2+015852	0.372810	4365.98	4.484410e-13	922	1.81	43.96
2XMM J081422.1+514839	0.376760	2286.34	1.235040e-12	468	1.95	44.41
2XMM J024207.2+000038	0.385000	1073.15	1.388040e-13	168	2.44	43.42
2XMM J163331.8+570520	0.386000	1212.77	3.384670e-13	249	1.60	43.84
2XMM J100921.9+534925	0.387870	952.14	2.102780e-13	142	2.10	43.61
2XMM J094404.3+480647	0.391790	1952.77	3.561740e-13	165	3.05	43.69
2XMM J105407.1+573524	0.394000	1019.72	1.508720e-13	104	3.23	43.29
2XMM J121808.5+471613	0.397900	2257.52	3.022100e-13	485	1.97	43.83
2XMM J154530.3+484608	0.399610	1487.42	7.955350e-13	160	3.34	44.08
2XMM J124408.9+113334	0.401000	3151.89	2.708970e-13	634	1.89	43.83
2XMM J134859.3+601457	0.404000	668.30	1.497830e-13	127	1.72	43.52
2XMM J215151.0-194605	0.424000	2019.62	8.103410e-13	571	1.82	44.41
2XMM J000102.4-245849	0.433000	615.35	1.710100e-13	123	1.92	43.68
2XMM J151703.6+562338	0.434000	1109.59	3.717660e-13	261	1.81	44.01
2XMM J134255.4+000635	0.436000	699.59	1.489070e-13	103	2.41	43.58
2XMM J123800.9+621336	0.440300	2049.47	1.857910e-13	233	3.11	43.54
2XMM J125906.4-014827	0.442900	3084.68	3.854710e-13	893	1.78	44.10
2XMM J105224.9+441505	0.443510	1346.01	6.083390e-13	264	2.15	44.24
2XMM J112455.9+384634	0.444000	824.36	7.589230e-14	98	1.96	43.22
2XMM J131014.1+322422	0.448000	1542.97	7.921660e-14	212	2.00	43.32
2XMM J030234.8+000107	0.450000	658.05	8.534050e-14	195	1.79	43.45
2XMM J022039.4-030820	0.451000	1106.73	3.088550e-13	131	3.77	43.86
2XMM J234715.9+005602	0.455700	710.17	1.533000e-13	156	2.28	43.70
2XMM J105205.1+574114	0.462000	862.07	9.330060e-14	152	2.26	43.33
2XMM J033912.2-352812	0.463000	1494.99	2.016790e-13	543	1.89	43.86
2XMM J005030.8-520010	0.463000	999.01	3.062260e-13	172	2.08	44.00
2XMM J211452.5+060742	0.466000	1058.92	1.048720e-13	457	1.53	43.56
2XMM J104026.8+204544	0.467000	1326.26	1.507430e-12	298	2.04	44.68
2XMM J002618.7+105019	0.474000	1543.49	7.392750e-13	420	1.87	44.43
2XMM J233154.3+193834	0.475000	1051.86	4.066030e-13	253	2.43	44.11

continued.

IAUNAME	z	PN counts [0.2–12 keV]	Flux [0.2–12 keV]	PN counts [2–10 keV]	Γ	$logL_X$ [2–10 keV]
2XMM J134304.5+403217	0.475790	2825.30	3.052170e-13	299	2.11	43.98
2XMM J021618.2-050608	0.478000	1334.73	2.674330e-13	426	1.59	44.00
2XMM J141724.5+523025	0.478700	1233.37	1.203660e-13	252	2.02	43.56
2XMM J124219.2+023118	0.479610	815.06	1.900990e-13	63	1.83	43.64
2XMM J150148.8+014403	0.484000	720.98	1.764090e-13	134	1.71	43.73
2XMM J214041.4-234718	0.490000	874.63	5.272120e-13	197	1.58	44.32
2XMM J003039.4+262055	0.492000	2168.31	7.539070e-13	566	1.81	44.52
2XMM J123127.3+135447	0.511360	636.88	3.223380e-13	99	3.39	44.04
2XMM J123702.7+621544	0.512360	822.75	4.480310e-14	348	1.59	43.38
2XMM J002914.1+345632	0.517000	617.13	3.228070e-13	344	1.95	44.29
2XMM J121923.2+470940	0.520000	947.28	4.013630e-13	310	1.59	44.29
2XMM J093347.9+551846	0.523000	542.15	2.840860e-13	227	1.57	44.20
2XMM J091029.0+542719	0.525940	4934.31	3.875610e-13	532	2.10	44.14
2XMM J130454.3+673007	0.538510	683.79	1.313400e-13	119	2.31	43.67
2XMM J133739.8-125725	0.539000	17040.80	5.114570e-12	5693	1.69	45.47
2XMM J033208.6-274734	0.544000	4919.29	2.202730e-13	1350	2.00	44.06
2XMM J001831.9+162925	0.553000	2410.91	2.411140e-13	489	2.67	44.02
2XMM J111135.6+482945	0.558440	5847.60	1.101890e-12	1210	1.91	44.73
2XMM J024049.2-080942	0.563000	807.46	6.227280e-14	215	2.52	43.58
2XMM J145411.4+183945	0.567000	860.00	1.083190e-13	173	1.70	43.73
2XMM J084858.0+445435	0.573000	819.36	6.060290e-14	197	2.72	43.57
2XMM J140053.0+030105	0.573000	613.59	1.139050e-13	174	2.55	43.84
2XMM J101850.4+411508	0.577110	2155.47	5.494270e-13	442	2.08	44.41
2XMM J022716.1-044539	0.590000	662.96	1.175990e-13	164	2.27	43.82
2XMM J132447.4+300900	0.594000	663.75	1.822610e-13	482	1.63	44.19
2XMM J164131.6+385841	0.595840	1190.21	7.038370e-13	759	1.75	44.73
2XMM J083117.4+524855	0.604000	1101.50	7.037920e-14	376	2.35	43.68
2XMM J123725.9+620232	0.605000	836.71	5.229540e-14	159	3.03	43.42
2XMM J125903.9+344702	0.608020	875.30	2.100270e-13	221	1.96	44.15
2XMM J124903.4-061046	0.610000	1484.80	2.545970e-13	271	2.11	44.09
2XMM J094009.6+033042	0.615640	1118.97	2.706040e-13	267	2.39	44.21
2XMM J094104.0+385351	0.615690	8046.19	9.707500e-13	2157	1.66	44.81
2XMM J091011.1+542724	0.625000	18851.90	1.124780e-12	4533	1.81	44.89
2XMM J095640.9+695201	0.626000	648.03	2.321360e-13	103	3.99	44.16
2XMM J021923.3-045149	0.629000	1540.05	1.366640e-13	286	2.41	43.91
2XMM J030206.7-000121	0.641000	2174.87	4.958450e-13	665	1.81	44.50
2XMM J140745.3+283028	0.642000	1624.88	8.417300e-13	394	1.70	44.72
2XMM J122051.3+750532	0.643000	1223.94	7.894300e-13	410	1.80	44.78
2XMM J023057.3-010033	0.649390	665.24	1.362710e-13	132	1.62	43.99
2XMM J130028.5+283010	0.649400	7346.30	1.238050e-12	2238	1.99	45.00
2XMM J012447.7+320727	0.654000	4342.53	1.481180e-12	1270	1.72	45.08
2XMM J163255.5+373500	0.655480	1435.34	4.222710e-13	228	2.18	44.43
2XMM J102147.4+130850	0.655980	1425.27	2.813720e-13	452	1.84	44.37
2XMM J004258.3-203713	0.656000	1169.84	5.029590e-13	309	1.78	44.59
2XMM J100232.1+023537	0.657170	588.34	1.606500e-13	125	2.19	44.02
2XMM J020118.6-091936	0.660820	740.38	2.803750e-13	214	3.26	44.39
2XMM J083026.8+524601	0.661000	756.28	1.074510e-13	289	1.63	43.93
2XMM J030707.3-000424	0.663900	974.25	9.277680e-14	212	2.18	43.89
2XMM J004800.1-250953	0.664000	1090.41	2.173690e-13	432	1.79	44.27
2XMM J114656.7+472755	0.667760	849.50	3.770570e-13	202	2.45	44.46
2XMM J024952.0-311402	0.669000	889.36	1.227180e-13	92	1.81	44.04
2XMM J111606.9+423645	0.670220	2815.96	4.168520e-13	1008	1.65	44.57
2XMM J100309.4+554134	0.673750	688.18	1.487560e-13	153	2.13	44.08
2XMM J164056.2+363404	0.676260	990.62	7.374430e-13	261	1.79	44.81
2XMM J123716.2+620708	0.679000	996.62	4.664900e-14	239	2.42	43.52
2XMM J005324.5+123344	0.679000	1289.68	4.783500e-13	456	1.59	44.61
2XMM J084047.6+131223	0.680800	4278.33	3.024110e-12	1747	1.65	45.49
2XMM J031253.7-765414	0.683000	689.68	1.761130e-13	334	1.43	44.25
2XMM J095938.9+021201	0.688950	835.97	7.309280e-14	132	2.11	43.71
2XMM J105433.6-114932	0.694500	779.54	1.059890e-13	241	2.78	43.98
2XMM J112306.3+013749	0.695700	1379.43	1.274230e-13	206	3.28	43.86

continued.

IAUNAME	z	PN counts [0.2–12 keV]	Flux [0.2–12 keV]	PN counts [2–10 keV]	Γ	$logL_X$ [2–10 keV]
2XMM J111750.7+075710	0.698000	3656.28	5.636710e-13	1465	2.18	44.73
2XMM J133027.6-013900	0.701100	670.10	2.054770e-13	172	1.61	44.24
2XMM J115024.7+015620	0.705730	970.03	2.299550e-13	357	1.81	44.27
2XMM J123538.5+621643	0.712000	1997.67	2.486790e-13	570	1.72	44.39
2XMM J021808.2-045844	0.712000	8885.98	6.271730e-13	2183	1.76	44.76
2XMM J103344.9+574910	0.713000	916.22	6.580090e-14	174	1.64	43.70
2XMM J084840.3+445801	0.716000	703.14	1.084370e-13	257	1.83	44.10
2XMM J033226.9-274105	0.730000	3522.70	1.788940e-13	786	1.76	44.23
2XMM J141700.7+521918	0.740000	838.89	4.228830e-14	160	2.20	43.58
2XMM J015234.7-135929	0.743900	534.92	3.288040e-14	146	2.44	43.63
2XMM J103413.9+585252	0.745190	576.68	2.070960e-13	101	5.12	44.22
2XMM J125301.4-292538	0.746500	741.09	3.961430e-14	255	1.76	43.69
2XMM J221715.1+002615	0.753600	1343.79	1.800050e-13	396	1.97	44.27
2XMM J222823.7-051306	0.758000	864.94	1.282140e-13	345	1.63	44.16
2XMM J105254.3+572342	0.761000	881.80	6.194140e-14	304	0.76	43.79
2XMM J011547.0+331238	0.764000	624.03	3.184190e-13	232	1.90	44.67
2XMM J103446.8+575128	0.765000	678.00	9.763310e-14	184	2.02	44.01
2XMM J100001.3+024845	0.765920	735.48	1.445060e-13	244	2.15	44.34
2XMM J053910.7-283526	0.770000	612.02	7.488650e-14	131	2.12	43.89
2XMM J045419.6-030419	0.775000	1728.78	1.703740e-13	413	3.02	44.29
2XMM J105348.7+573034	0.780000	609.19	6.745200e-14	384	1.39	43.96
2XMM J134133.1+353252	0.780000	948.84	4.973120e-13	249	1.92	44.74
2XMM J104522.0-012844	0.782000	1633.18	4.639290e-13	355	2.21	44.73
2XMM J115057.7-284401	0.789000	1472.86	1.742480e-13	502	2.24	44.36
2XMM J121836.1+054628	0.795290	555.11	2.928460e-13	68	1.39	44.30
2XMM J134256.5+000057	0.804350	1422.13	3.733730e-13	471	1.64	44.73
2XMM J141651.3+522047	0.807700	639.58	3.609840e-14	236	2.61	43.82
2XMM J081014.5+280337	0.821020	1856.76	6.464710e-13	500	1.83	44.95
2XMM J150431.2+474151	0.823800	1729.54	7.567630e-13	645	2.09	44.98
2XMM J004341.4+005610	0.830000	915.48	3.111520e-13	276	2.03	44.54
2XMM J033238.0-273945	0.836600	566.17	7.295920e-14	108	2.64	43.74
2XMM J123739.3+622059	0.837000	1004.98	6.237470e-14	312	2.25	43.92
2XMM J123038.0+162540	0.841000	1116.08	3.553070e-13	229	1.97	44.61
2XMM J111832.8+074901	0.847000	1309.16	1.016870e-13	190	2.39	44.12
2XMM J133408.8+375707	0.850000	672.66	4.016050e-14	237	2.14	43.86
2XMM J000100.1-250501	0.851000	615.20	2.129870e-13	345	1.47	44.62
2XMM J033737.5-350003	0.853830	2073.79	1.217540e-13	526	2.47	44.22
2XMM J082257.6+404149	0.864780	959.59	5.389330e-13	333	1.70	44.98
2XMM J035348.8-102015	0.870000	685.61	1.475430e-13	183	2.52	44.32
2XMM J021640.7-044404	0.870000	1809.60	3.524850e-13	473	1.69	44.69
2XMM J134323.6+001223	0.873970	1257.31	3.193340e-13	352	2.15	44.70
2XMM J081030.2+281326	0.887470	650.60	1.692050e-13	216	1.98	44.49
2XMM J134252.9+403202	0.905810	2254.94	3.425680e-13	823	1.63	44.72
2XMM J123759.5+621102	0.908420	2033.85	2.883920e-13	609	2.02	44.64
2XMM J131107.3-012857	0.912600	1203.59	2.083280e-13	343	2.40	44.55
2XMM J141717.8+231719	0.921000	466.14	6.300670e-13	174	2.11	45.10
2XMM J124244.5+022954	0.937160	1076.42	1.374240e-13	414	1.97	44.45
2XMM J103338.1+574544	0.945000	1254.05	7.960170e-14	428	2.34	44.23
2XMM J022711.8-045038	0.946000	916.85	1.459900e-13	342	1.86	44.49
2XMM J023932.7-342527	0.947000	2233.52	1.364740e-13	750	1.88	44.40
2XMM J015311.0-135105	0.949000	750.78	1.268290e-13	246	1.39	44.36
2XMM J111609.6+441845	0.953610	1207.00	2.198900e-13	352	1.82	44.59
2XMM J221523.6-174318	0.956000	2061.55	6.499670e-14	575	1.99	44.05
2XMM J090029.0+390145	0.963730	1177.38	2.324690e-13	336	2.13	44.66
2XMM J215212.9-272455	0.968700	921.55	1.688440e-13	200	2.28	44.49
2XMM J024105.8-081153	0.978580	928.85	5.888360e-14	258	2.15	44.09
2XMM J141735.9+523029	0.985000	1428.46	1.572350e-13	450	1.78	44.48
2XMM J112014.7+133228	0.995000	1266.99	9.529160e-14	409	1.95	44.33
2XMM J130248.9-023521	1.014200	555.48	1.000770e-13	139	4.94	44.22
2XMM J123706.8+621702	1.020000	772.54	6.671810e-14	201	2.19	44.14
2XMM J004647.4-252149	1.022000	1326.59	1.621740e-13	297	2.65	44.10

continued.

IAUNAME	z	PN counts [0.2–12 keV]	Flux [0.2–12 keV]	PN counts [2–10 keV]	Γ	$logL_X$ [2–10 keV]
2XMM J095857.3+021314	1.024310	2262.92	5.157100e-13	848	1.81	45.07
2XMM J033226.4-274035	1.030000	1173.85	5.810340e-14	469	1.84	44.58
2XMM J112340.3+385129	1.034080	994.58	3.832630e-13	208	2.22	44.82
2XMM J100056.5+554059	1.038000	607.90	2.227610e-13	197	3.74	44.66
2XMM J123049.7+640848	1.040230	770.30	7.037050e-14	178	2.58	44.20
2XMM J033942.8-352409	1.042950	2378.30	1.360880e-13	588	2.33	44.48
2XMM J230444.8+031146	1.044000	2293.78	5.980140e-13	700	2.19	45.17
2XMM J220230.0-190151	1.045000	930.22	2.073950e-13	151	2.62	44.60
2XMM J030307.3+001020	1.046800	798.85	9.803930e-14	300	2.64	44.41
2XMM J085841.4+140944	1.048000	5042.28	1.705540e-12	2355	1.79	45.60
2XMM J092053.8+365832	1.082830	1414.47	1.776080e-13	367	1.98	44.66
2XMM J021817.4-045112	1.085000	3435.60	5.110530e-13	1031	1.81	45.07
2XMM J085808.9+274522	1.090110	3138.97	1.667330e-13	1103	2.16	44.65
2XMM J103419.6+574449	1.098000	830.95	6.998300e-14	296	2.19	44.30
2XMM J033609.3-360731	1.100000	983.82	3.644900e-13	292	1.62	44.97
2XMM J141643.2+521436	1.110000	1352.10	1.734290e-13	505	1.58	44.70
2XMM J024200.8+000021	1.112000	1467.45	3.135950e-13	535	2.07	44.86
2XMM J141838.2+522400	1.118400	714.80	8.225710e-14	193	2.18	44.44
2XMM J221738.4+001207	1.121000	657.38	3.458620e-14	211	1.94	43.93
2XMM J140719.3+281814	1.121000	908.23	4.564820e-13	341	1.98	45.05
2XMM J121715.4+471214	1.132700	1274.27	1.719270e-13	413	2.52	44.65
2XMM J120450.6+442835	1.141880	732.30	1.471390e-13	190	2.07	44.57
2XMM J035319.0-101703	1.146000	648.07	2.137180e-13	214	3.33	44.72
2XMM J053905.5-283316	1.158000	739.70	1.607400e-13	383	2.27	44.73
2XMM J221515.2-173222	1.159000	3029.71	1.923980e-13	694	2.44	44.64
2XMM J095918.7+020951	1.161600	611.88	2.444850e-13	237	2.45	44.81
2XMM J022735.7-041123	1.167000	1202.54	2.745170e-13	358	1.53	45.00
2XMM J134511.9+554759	1.168510	951.07	3.762520e-13	177	2.29	44.89
2XMM J085810.0+275052	1.169000	855.21	7.726200e-14	409	1.06	44.25
2XMM J133903.0+043649	1.175000	633.19	1.809870e-13	228	1.54	44.69
2XMM J130808.4+293448	1.176000	649.25	8.033430e-14	111	3.17	44.08
2XMM J103031.6+052455	1.182860	2269.82	9.686790e-14	720	2.13	44.51
2XMM J123337.5+073133	1.184880	678.00	4.313310e-13	333	1.81	45.12
2XMM J031015.6-765133	1.187000	3753.83	7.648110e-13	1823	1.65	45.46
2XMM J052108.7-251912	1.200000	978.01	5.459570e-13	349	1.76	45.22
2XMM J142355.5+383150	1.205010	654.31	1.423270e-13	207	1.97	44.65
2XMM J011302.0-453021	1.208000	1633.53	7.431200e-14	296	3.59	44.27
2XMM J115838.5+435505	1.208350	564.86	5.451000e-14	247	1.46	44.24
2XMM J005724.5-273200	1.209000	1757.92	1.136870e-13	525	2.68	44.53
2XMM J011327.2-453830	1.220000	561.33	8.389810e-14	134	2.83	44.16
2XMM J124728.5+671725	1.220510	1024.47	9.414510e-14	386	1.69	44.53
2XMM J033229.9-274528	1.221000	603.93	4.346770e-14	214	2.56	44.15
2XMM J102623.2+383701	1.225930	789.03	1.584840e-13	331	2.58	44.70
2XMM J021745.1-734723	1.234000	1010.09	5.907490e-13	474	2.12	45.35
2XMM J095924.4+015954	1.236040	628.09	1.370560e-13	184	1.90	44.73
2XMM J053923.5-284222	1.245000	1518.52	2.431180e-13	540	2.62	44.87
2XMM J101112.2+554447	1.246000	1659.62	2.152470e-13	801	1.64	44.97
2XMM J094345.1+465155	1.246140	590.05	6.016820e-14	225	2.01	44.49
2XMM J103337.9+574238	1.265000	1021.99	6.328700e-14	368	2.02	44.41
2XMM J133027.5-014203	1.268060	1385.77	3.405330e-13	579	1.82	45.11
2XMM J114031.1+660858	1.269000	966.58	2.348640e-13	351	2.26	44.92
2XMM J125456.8+564941	1.272490	489.68	2.108460e-13	235	1.63	45.04
2XMM J031311.7-765430	1.274000	839.57	1.967650e-13	426	2.02	44.87
2XMM J000020.4-322100	1.275000	738.69	1.912820e-13	221	1.90	44.75
2XMM J100717.2+124543	1.280850	1060.22	1.561950e-13	403	2.62	44.79
2XMM J105050.0+573819	1.281410	1221.30	9.271300e-14	365	2.05	44.57
2XMM J084911.4+444454	1.286000	779.85	8.160270e-14	296	2.57	44.40
2XMM J092633.4+304535	1.308940	675.46	1.581580e-13	226	2.63	44.71
2XMM J095908.3+024309	1.317420	2836.26	3.848530e-13	483	2.09	45.09
2XMM J033216.2-273930	1.320000	623.90	4.201020e-14	138	4.30	44.08
2XMM J234724.7+005248	1.322600	895.60	2.083620e-13	338	1.61	44.97

continued.

IAUNAME	z	PN counts [0.2–12 keV]	Flux [0.2–12 keV]	PN counts [2–10 keV]	Γ	$logL_X$ [2–10 keV]
2XMM J163428.9+703132	1.334000	12470.60	2.579540e-12	5015	2.08	46.08
2XMM J002114.5-483432	1.340000	954.62	1.357390e-13	307	2.46	44.71
2XMM J124406.9+113524	1.343710	1762.32	1.381080e-13	712	1.88	44.85
2XMM J141352.9+440230	1.347000	620.20	8.935500e-14	185	1.64	44.54
2XMM J021834.5-051356	1.351000	559.41	7.279720e-14	232	2.98	44.54
2XMM J133431.3+374831	1.359000	1157.66	8.788320e-14	511	1.72	44.60
2XMM J130100.8+281944	1.360000	1846.04	1.835570e-13	699	2.03	44.89
2XMM J145344.7+033329	1.365000	728.07	1.093890e-13	363	1.80	44.76
2XMM J130120.0+282137	1.369350	1282.24	4.465700e-13	475	2.28	45.18
2XMM J091301.0+525929	1.376400	2778.93	1.671380e-12	1123	1.69	45.85
2XMM J105242.2+573158	1.380000	558.32	3.112350e-14	349	1.84	44.23
2XMM J024849.7-311542	1.390000	2195.34	2.871110e-13	717	2.14	45.14
2XMM J120913.6+433920	1.397840	1274.13	5.950030e-13	628	1.83	45.48
2XMM J083049.6+524910	1.400000	2407.86	2.011800e-13	1157	1.81	45.03
2XMM J021830.5-045623	1.401000	1224.24	9.413900e-14	424	2.40	44.69
2XMM J095852.1+025156	1.407200	973.54	9.836850e-14	316	2.25	44.60
2XMM J024008.0-343420	1.408000	1224.42	8.111080e-14	462	2.87	44.58
2XMM J103026.6+053816	1.411950	613.10	9.812900e-14	220	2.99	44.50
2XMM J100120.7+555351	1.413060	5230.60	2.101720e-12	1759	2.09	46.01
2XMM J102412.2+042025	1.425000	854.91	1.566340e-13	248	3.25	44.96
2XMM J153452.4+013104	1.435000	365.44	1.533440e-12	141	1.44	45.91
2XMM J105230.0+573913	1.437000	1220.03	6.811700e-14	480	2.30	44.57
2XMM J123707.1+622144	1.449790	611.75	4.159620e-14	301	2.21	44.36
2XMM J112320.7+013748	1.462000	2004.66	3.546820e-13	1234	2.37	45.34
2XMM J111840.5+075323	1.462870	998.20	1.084170e-13	416	1.81	44.76
2XMM J095456.7+174332	1.472000	3745.13	9.449740e-13	1971	1.60	45.76
2XMM J163201.1+373749	1.476070	1973.67	3.746020e-13	647	2.31	45.30
2XMM J154352.0+540002	1.480000	765.70	1.521130e-13	303	2.56	44.91
2XMM J221751.3+001146	1.491400	746.21	5.070120e-14	332	2.32	44.39
2XMM J140856.4-075225	1.494000	1904.42	7.062000e-13	890	1.53	45.59
2XMM J105257.1+572507	1.527000	971.83	3.349470e-14	385	2.14	44.30
2XMM J100248.9+325130	1.535510	733.98	1.410170e-13	287	2.25	44.89
2XMM J105108.2+573345	1.540000	596.77	5.304040e-14	320	2.26	44.48
2XMM J095908.6+025423	1.556380	586.49	7.817160e-14	167	3.08	44.66
2XMM J012505.5+014626	1.559000	1657.10	2.990000e-13	831	1.58	45.23
2XMM J105309.2+572821	1.568000	671.45	2.762790e-14	257	2.24	44.11
2XMM J104424.8-013519	1.570000	775.36	1.684480e-13	393	1.59	45.08
2XMM J083205.4+524353	1.572500	1192.40	6.429360e-14	528	2.02	44.61
2XMM J104039.5+061521	1.583880	975.21	1.292150e-13	453	2.15	44.91
2XMM J115726.2+434954	1.597000	734.45	1.419310e-13	186	3.26	44.53
2XMM J085851.9+274738	1.598980	814.47	4.989590e-14	374	2.16	44.69
2XMM J033211.6-273726	1.600000	579.23	9.784790e-14	255	1.66	44.65
2XMM J141622.7+521916	1.600000	761.42	1.001330e-13	384	1.84	44.82
2XMM J133358.6+375938	1.610000	649.87	7.101330e-14	283	2.46	44.67
2XMM J111822.2+074449	1.615000	1635.61	1.007440e-13	740	2.00	44.80
2XMM J135023.6+265243	1.615000	644.67	1.580450e-13	224	2.61	44.94
2XMM J105259.0+573030	1.676000	1159.85	4.327620e-14	569	1.44	44.53
2XMM J182158.3+681840	1.692000	862.80	5.242400e-13	374	1.94	45.59
2XMM J034015.4-352849	1.740000	864.89	1.064420e-13	185	2.09	44.91
2XMM J121804.5+470850	1.743000	613.04	6.942570e-14	314	1.75	44.73
2XMM J124615.7+673032	1.769170	1004.07	1.740890e-13	496	1.79	45.14
2XMM J102417.4+041657	1.775000	1174.59	2.061240e-13	539	1.70	45.20
2XMM J093359.2+551550	1.863470	775.21	9.922010e-14	416	1.59	45.04
2XMM J233630.5+021045	1.871000	795.55	2.737400e-13	211	1.62	45.38
2XMM J095834.0+024427	1.888290	1484.29	6.935060e-14	622	1.92	44.85
2XMM J133452.1+375744	1.890000	772.25	5.126730e-14	333	1.91	44.62
2XMM J044858.8-204446	1.894000	405.11	8.195490e-13	249	2.43	45.78
2XMM J021642.3-043552	1.985000	594.33	1.639290e-13	435	1.74	45.36
2XMM J121732.7+465829	1.990710	1093.33	2.226120e-13	469	3.78	45.27
2XMM J100159.7+022641	2.032930	661.47	1.186610e-13	303	1.94	45.02
2XMM J022415.7-041416	2.106000	734.78	4.616020e-14	387	1.79	44.74

continued.

IAUNAME	z	PN counts [0.2–12 keV]	Flux [0.2–12 keV]	PN counts [2–10 keV]	Γ	$logL_X$ [2–10 keV]
2XMM J105643.1-034042	2.115000	598.29	1.035210e-13	285	2.07	45.03
2XMM J013205.2-400048	2.120000	612.47	1.440330e-13	240	3.86	45.19
2XMM J111517.9-215656	2.140000	2581.03	2.325690e-13	1320	2.17	45.57
2XMM J112011.8+133122	2.150000	950.89	7.420210e-14	444	2.00	45.12
2XMM J112338.0+052038	2.180610	976.50	3.322290e-13	532	1.64	45.61
2XMM J121422.9+024252	2.223180	1465.00	5.750050e-13	798	1.72	45.89
2XMM J124220.1+023257	2.224230	662.26	8.550120e-14	277	2.79	44.97
2XMM J032353.3-371556	2.246000	1135.31	2.334570e-13	596	1.78	45.59
2XMM J110633.4-182123	2.319200	682.20	2.168440e-13	350	1.71	45.53
2XMM J115005.3+013852	2.325360	604.40	1.183220e-13	321	2.60	45.19
2XMM J134843.9-035324	2.344000	910.32	1.502770e-13	482	1.79	45.46
2XMM J154359.4+535902	2.370410	723.34	1.383640e-13	429	2.47	45.46
2XMM J111928.3+130250	2.400640	1290.55	3.052340e-13	673	1.67	45.73
2XMM J222006.7-280322	2.406000	2944.91	3.197810e-13	1418	1.94	45.81
2XMM J123622.9+621526	2.591960	603.58	2.542410e-14	268	2.63	44.68
2XMM J144453.5+291906	2.638000	2805.68	3.281000e-13	1491	2.01	45.89
2XMM J021659.8-053202	2.809000	788.54	1.381700e-13	441	2.14	45.51
2XMM J152553.8+513649	2.882510	2270.55	2.837280e-13	1360	2.23	45.89
2XMM J124300.3+113554	2.940280	1026.37	1.834010e-13	607	1.75	45.63
2XMM J111038.5+483116	2.954900	813.13	7.408580e-14	416	2.36	45.33
2XMM J013301.9-400628	3.023000	1890.14	2.032130e-13	1011	2.12	45.81
2XMM J042214.7-384452	3.110000	2155.29	7.200770e-13	1287	1.80	46.41
2XMM J122135.6+280614	3.305000	3467.54	4.868880e-13	1929	1.42	46.07
2XMM J200324.1-325144	3.773000	3705.66	9.101580e-13	2171	1.73	46.56
2XMM J000322.9-260318	4.098000	1366.02	9.734330e-14	852	2.28	45.83
2XMM J132611.8+074357	4.170000	779.53	7.725790e-14	486	2.34	45.71
2XMM J092636.4+305504	4.190000	1010.67	9.972560e-14	626	2.70	45.88
2XMM J102838.8-084438	4.276000	5650.75	1.454850e-12	3069	1.57	46.77
2XMM J151002.9+570243	4.308720	1606.90	6.873270e-13	888	1.85	46.47
2XMM J052506.1-334305	4.413000	7538.45	1.582970e-12	4222	1.81	46.92
2XMM J002207.9-150539	4.528000	729.95	5.146440e-14	414	1.45	45.58
2XMM J143023.7+420436	4.715000	1578.67	2.509710e-12	956	2.03	47.30
2XMM J145147.0-151220	4.763000	792.81	2.563280e-13	458	1.38	46.21

Bibliography

Antonucci, R. 1993, ARA&A, 31, 473

Antonucci, R. R. J. & Miller, J. S. 1985, ApJ, 297, 621

Arnaud, K. A. 1996, in Astronomical Society of the Pacific Conference Series, Vol. 101, Astronomical Data Analysis Software and Systems V, ed. G. H. Jacoby & J. Barnes

Arnaud, K. A., Branduardi-Raymont, G., Culhane, J. L., et al. 1985, MNRAS, 217, 105

Awaki, H., Koyama, K., Inoue, H., & Halpern, J. P. 1991, PASJ, 43, 195

Balestra, I., Tozzi, P., Ettori, S., et al. 2007, A&A, 462, 429

Ballantyne, D. R. 2010, ApJ, 716, L27

Bambynek, W., CRASEMANN, B., FINK, R. W., et al. 1972, Rev. Mod. Phys., 44, 716

Bardeen, J. M., Press, W. H., & Teukolsky, S. A. 1972, ApJ, 178, 347

Barvainis, R. 1987, ApJ, 320, 537

Barvainis, R. 1990, ApJ, 353, 419

Baskin, A. & Laor, A. 2004, MNRAS, 350, L31

Bassani, L., Dadina, M., Maiolino, R., et al. 1999, ApJS, 121, 473

Begelman, M. C. 1985, in Astrophysics of Active Galaxies and Quasi-Stellar Objects, ed. J. S. Miller, 411–452

Behar, E., Rasmussen, A. P., Blustin, A. J., et al. 2003, ApJ, 598, 232

Bennert, N., Falcke, H., Schulz, H., Wilson, A. S., & Wills, B. J. 2002, ApJ, 574, L105

Bennett, A. S. & Smith, F. G. 1961, MNRAS, 122, 71

Bevington, P. R. 1969, Data reduction and error analysis for the physical sciences, ed. Bevington, P. R.

Bianchi, S., Guainazzi, M., Matt, G., & Fonseca Bonilla, N. 2007, A&A, 467, L19

Blandford, R. D. 1985, Theoretical models of active galactic nuclei, ed. Neckel, T. & Vehrenberg, H., 281–299

Blustin, A. J., Kriss, G. A., Holczer, T., et al. 2007, A&A, 466, 107

Bowyer, C. S., Lampton, M., Mack, J., & de Mendonca, F. 1970, ApJ, 161, L1+

Brandt, W. N. & Hasinger, G. 2005, ARA&A, 43, 827

Brenneman, L. W. & Reynolds, C. S. 2006, ApJ, 652, 1028

Brusa, M., Gilli, R., & Comastri, A. 2005, ApJ, 621, L5

Cappi, M., Panessa, F., Bassani, L., et al. 2006, A&A, 446, 459

Cash, W. 1979, ApJ, 228, 939

Chaudhary, P., Brusa, M., Hasinger, G., Merloni, A., & Comastri, A. 2010, A&A, 518, A58

Corral, A., Page, M. J., Carrera, F. J., et al. 2008, A&A, 492, 71

Crenshaw, D. M., Kraemer, S. B., & George, I. M. 2003, ARA&A, 41, 117

Crummy, J., Fabian, A. C., Gallo, L., & Ross, R. R. 2006, MNRAS, 365, 1067

Cunningham, C. T. 1975, ApJ, 202, 788

de La Calle Pérez, I., Longinotti, A. L., Guainazzi, M., et al. 2010, A&A, 524, A50

den Herder, J. W., Brinkman, A. C., Kahn, S. M., et al. 2001, A&A, 365, L7

Dong, X., Wang, T., Wang, J., et al. 2009, ApJ, 703, L1

Edge, D. O., Shakeshaft, J. R., McAdam, W. B., Baldwin, J. E., & Archer, S. 1959, MmRAS, 68, 37

Elvis, M., Maccacaro, T., Wilson, A. S., et al. 1978, MNRAS, 183, 129

Fabian, A. C., Iwasawa, K., Reynolds, C. S., & Young, A. J. 2000, PASP, 112, 1145

Fabian, A. C. & Miniutti, G. 2005, ArXiv Astrophysics e-prints

Fabian, A. C., Rees, M. J., Stella, L., & White, N. E. 1989, MNRAS, 238, 729

Fabian, A. C., Vaughan, S., Nandra, K., et al. 2002, MNRAS, 335, L1

Fiore, F., Giommi, P., Vignali, C., et al. 2001, MNRAS, 327, 771

Frank, J., King, A., & Raine, D. J. 2002, Accretion Power in Astrophysics: Third Edition, ed. Frank, J., King, A., & Raine, D. J.

George, I. M. & Fabian, A. C. 1991, MNRAS, 249, 352

George, I. M., Turner, T. J., Netzer, H., et al. 1998, ApJS, 114, 73

Ginzburg, V. L. & Ozernoi, L. M. 1977, Ap&SS, 50, 23

Greenstein, J. L. 1963, Nature, 197, 1041

Guainazzi, M., Bianchi, S., & Dovčiak, M. 2006a, Astronomische Nachrichten, 327, 1032

Guainazzi, M., Siemiginowska, A., Stanghellini, C., et al. 2006b, A&A, 446, 87

Guilbert, P. W. & Rees, M. J. 1988, MNRAS, 233, 475

Haardt, F. & Maraschi, L. 1991, ApJ, 380, L51

Haardt, F. & Maraschi, L. 1993, ApJ, 413, 507

Haardt, F., Maraschi, L., & Ghisellini, G. 1994, ApJ, 432, L95

Halpern, J. P. 1984, ApJ, 281, 90

Hamann, F., Warner, C., Dietrich, M., & Ferland, G. 2007, in Astronomical Society of the Pacific Conference Series, Vol. 373, The Central Engine of Active Galactic Nuclei, ed. L. C. Ho & J.-W. Wang, 653–+

Hasinger, G. 2008, A&A, 490, 905

House, L. L. 1969, ApJS, 18, 21

Iwasawa, K. & Taniguchi, Y. 1993, ApJ, 413, L15

Jaffe, W., Meisenheimer, K., Röttgering, H. J. A., et al. 2004, Nature, 429, 47

Jansen, F., Lumb, D., Altieri, B., et al. 2001, A&A, 365, L1

Kaspi, S., Brandt, W. N., George, I. M., et al. 2002, ApJ, 574, 643

Kaspi, S., Maoz, D., Netzer, H., et al. 2005, ApJ, 629, 61

Kawaguchi, T., Shimura, T., & Mineshige, S. 2001, ApJ, 546, 966

Kellermann, K. I., Sramek, R., Schmidt, M., Shaffer, D. B., & Green, R. 1989, AJ, 98, 1195

Koratkar, A. & Blaes, O. 1999, PASP, 111, 1

Korista, K., Baldwin, J., & Ferland, G. 1998, ApJ, 507, 24

Kraemer, S. B. & Crenshaw, D. M. 2000, ApJ, 544, 763

Krolik, J. H. 1999, Active galactic nuclei : from the central black hole to the galactic environment, ed. Krolik, J. H.

La Franca, F., Fiore, F., Comastri, A., et al. 2005, ApJ, 635, 864

Laor, A. 1991, ApJ, 376, 90

Lightman, A. P. & White, T. R. 1988, ApJ, 335, 57

Longair, M. S. 1992, High energy astrophysics. Vol.1: Particles, photons and their detection, ed. Longair, M. S.

Longinotti, A. L., de La Calle, I., Bianchi, S., Guainazzi, M., & Dovčiak, M. 2008, Mem. Soc. Astron. Italiana, 79, 259

Lynden-Bell, D. 1969, Nature, 223, 690

Magdziarz, P. & Zdziarski, A. A. 1995, MNRAS, 273, 837

Mainieri, V., Bergeron, J., Hasinger, G., et al. 2002, A&A, 393, 425

Makishima, K. 1986, in Lecture Notes in Physics, Berlin Springer Verlag, Vol. 266, The Physics of Accretion onto Compact Objects, ed. K. O. Mason, M. G. Watson, & N. E. White, 249–+

Mao, W., Hu, C., Wang, J., Zhao, G., & Zhang, S. 2010, Research in Astronomy and Astrophysics, 10, 905

Marshall, N., Warwick, R. S., & Pounds, K. A. 1981, MNRAS, 194, 987

Mason, K. O., Breeveld, A., Much, R., et al. 2001, A&A, 365, L36

Matt, G. 1999, in Astronomical Society of the Pacific Conference Series, Vol. 161, High Energy Processes in Accreting Black Holes, ed. J. Poutanen & R. Svensson, 149–+

Matt, G., Perola, G. C., & Piro, L. 1991, A&A, 247, 25

Miller, J. M. 2007, ARA&A, 45, 441

Miller, L., Turner, T. J., & Reeves, J. N. 2009, MNRAS, 399, L69

Morita, S. & Fujita, J. 1983, Journal of the Physical Society of Japan, 52, 1957

Mortlock, D. J., Warren, S. J., Venemans, B. P., et al. 2011, Nature, 474, 616

Mushotzky, R. & Ferland, G. J. 1984, ApJ, 278, 558

Mushotzky, R. F., Done, C., & Pounds, K. A. 1993, ARA&A, 31, 717

Nandra, K. 2006, MNRAS, 368, L62

Nandra, K., George, I. M., Mushotzky, R. F., Turner, T. J., & Yaqoob, T. 1997, ApJ, 488, L91

Nandra, K., O'Neill, P. M., George, I. M., & Reeves, J. N. 2007, MNRAS, 382, 194

Nandra, K. & Pounds, K. A. 1992, Nature, 359, 215

Nandra, K. & Pounds, K. A. 1994, MNRAS, 268, 405

Nayakshin, S. 2000a, ApJ, 540, L37

Nayakshin, S. 2000b, ApJ, 534, 718

Ness, J., Ehle, M., Breitfellner, M., & Díaz Trigo, M. 2010, XMM-Newton Users Handbook, issue 2.8.1, (ESA: XMM-Newton SOC)

Page, D. N. & Thorne, K. S. 1974, ApJ, 191, 499

Page, K. L., O'Brien, P. T., Reeves, J. N., & Turner, M. J. L. 2004, MNRAS, 347, 316

Panessa, F. & Bassani, L. 2002, A&A, 394, 435

Pappa, A., Georgantopoulos, I., Stewart, G. C., & Zezas, A. L. 2001, MNRAS, 326, 995

Patrick, A. R., Reeves, J. N., Porquet, D., et al. 2010, ArXiv e-prints

Perola, G. C., Matt, G., Cappi, M., et al. 2002, A&A, 389, 802

Peterson, B. M. 1997, An Introduction to Active Galactic Nuclei, ed. Goméz de Castro, A. I. & Franqueira, M.

Peterson, B. M., Wanders, I., Bertram, R., et al. 1998, ApJ, 501, 82

Pineau, F.-X., Motch, C., Carrera, F., et al. 2011, A&A, 527, A126+

Porquet, D., Reeves, J. N., O'Brien, P., & Brinkmann, W. 2004, A&A, 422, 85

Pounds, K. & Reeves, J. 2002, ArXiv Astrophysics e-prints

Pounds, K. A., Nandra, K., Stewart, G. C., George, I. M., & Fabian, A. C. 1990, Nature, 344, 132

Pozdnyakov, L. A., Sobol, I. M., & Syunyaev, R. A. 1983, Astrophysics and Space Physics Reviews, 2, 189

Pringle, J. E. 1981, ARA&A, 19, 137

Protassov, R., van Dyk, D. A., Connors, A., Kashyap, V. L., & Siemiginowska, A. 2002, ApJ, 571, 545

Rees, M. J. 1984, ARA&A, 22, 471

Reeves, J. N., Fabian, A. C., Kataoka, J., et al. 2006, Astronomische Nachrichten, 327, 1079

Reynolds, C. S. 1996, PhD thesis, university of Cambridge

Reynolds, C. S. & Nowak, M. A. 2003, Phys. Rep., 377, 389

Ross, R. R. & Fabian, A. C. 1993, MNRAS, 261, 74

Ross, R. R. & Fabian, A. C. 2005, MNRAS, 358, 211

Ross, R. R., Fabian, A. C., & Young, A. J. 1999, MNRAS, 306, 461

Rybicki, G. B. & Lightman, A. P. 1979, Radiative processes in astrophysics, ed. Rybicki, G. B. & Lightman, A. P.

Salpeter, E. E. 1964, ApJ, 140, 796

Schmidt, M. 1963, Nature, 197, 1040

Schneider, D. P., Richards, G. T., Hall, P. B., et al. 2010, AJ, 139, 2360

Seyfert, C. K. 1943, ApJ, 97, 28

Shakura, N. I. & Sunyaev, R. A. 1973, A&A, 24, 337

Shu, X. W., Yaqoob, T., & Wang, J. X. 2010, ApJS, 187, 581

Singh, V., Shastri, P., & Risaliti, G. 2011, ArXiv e-prints

Smith, D. A. & Done, C. 1996, MNRAS, 280, 355

Streblyanska, A., Hasinger, G., Finoguenov, A., et al. 2005, A&A, 432, 395

Strüder, L., Briel, U., Dennerl, K., et al. 2001, A&A, 365, L18

Tanaka, Y., Nandra, K., Fabian, A. C., et al. 1995, Nature, 375, 659

Terlevich, R., Tenorio-Tagle, G., Franco, J., & Melnick, J. 1992, MNRAS, 255, 713

Thorne, K. S. 1974, ApJ, 191, 507

Tran, H. D. 2001, ApJ, 554, L19

Tran, H. D. 2003, ApJ, 583, 632

Tristram, K. R. W., Meisenheimer, K., Jaffe, W., et al. 2007, A&A, 474, 837

Turner, M. J. L., Abbey, A., Arnaud, M., et al. 2001, A&A, 365, L27

Turner, T. J. & Miller, L. 2009, A&A Rev., 17, 47

Turner, T. J. & Pounds, K. A. 1989, MNRAS, 240, 833

Ueda, Y., Akiyama, M., Ohta, K., & Miyaji, T. 2003, ApJ, 598, 886

Ulrich, M.-H., Maraschi, L., & Urry, C. M. 1997, ARA&A, 35, 445

Urry, C. M. & Padovani, P. 1995, PASP, 107, 803

Walter, R. & Fink, H. H. 1993, A&A, 274, 105

Warner, C., Hamann, F., & Dietrich, M. 2004, ApJ, 608, 136

Watson, M. G., Schröder, A. C., Fyfe, D., et al. 2009, A&A, 493, 339

Wu, J., Vanden Berk, D. E., Brandt, W. N., et al. 2009a, ApJ, 702, 767

Wu, Y., Charmandaris, V., Huang, J., Spinoglio, L., & Tommasin, S. 2009b, ApJ, 701, 658

Xu, Y., Bian, W., Yuan, Q., & Huang, K. 2008, MNRAS, 389, 1703

Yaqoob, T. & Padmanabhan, U. 2004, ApJ, 604, 63

Zdziarski, A. A., Johnson, W. N., Done, C., Smith, D., & McNaron-Brown, K. 1995, ApJ, 438, L63

Zhou, X. & Wang, J. 2005, ApJ, 618, L83

XSA XMM-*Newton* Science Archive 36
ODF observation data files 36
XRTs X-ray telescopes 31
EPIC European Photon Imaging Camera 31
SSC Survey Science Center 33
GTI Good-Time-Interval 33
HST Hubble Space Telescope vii

Acknowledgments

First of all, I would like to express my sincere thanks to my PhD supervisor Prof. Dr. Günther Hasinger for giving me the opportunity to work at Max-Planck-Institut für extraterrestrische Physik (MPE). I sincerely thank him for his motivation, supervision and constant support at all levels throughout the whole duration of this work.

I sincerely thank Prof. Dr. Ralf Bender for agreeing to be the first referee of this thesis. I also thank Prof. Kirpal Nandra for his valuable advices and for agreeing to be the second referee of this thesis.

I am grateful to Dr. Marcella Brusa for her constant guidance, sound advices, encouragement and support throughout the whole duration of this work. This thesis wouldn't have been possible without you Marcella. Thank you very much for sharing your expertise, having time for me and teaching me many aspects of the scientific writing. Your enthusiasm and passion for science has always inspired me.

I thank Dr. Kazushi Iwasawa for introducing me to the subject of active galactic nuclei and giving me many exercises in the beginning of this project. I am thankful to Dr. Andrea Merloni and Prof. Andrea Comastri for their valuable comments and constructive suggestions on many drafts of our two papers.

Many thanks to all the members of MPE for their kind help over the years. In particular, I am indebted to Mrs. Christa Ingram, Mrs. Birgit Boller and Mrs. Gabi Kratschmann for their enormous help at all levels. Sincere thanks to Mrs. Gabi Kratschmann for proofreading a substantial portion of this thesis. Special thanks to Prof. Dr. Werner Becker and Prof. Dr. Thomas Boller for their caring nature and advices. Sincere thanks to Mr. Harald Baumgartner for his assistance in solving all computer related problems.

I wish to thank all my friends Ania Raitor, Angela Bongiorno, Martin Mühlegger, Martin Henze, Prabhdeep Kaur, Inderpal Singh, Ritu Agarwal and many others, for helping me get through the difficult times, and for all the emotional support, entertainment, and caring they provided. I am especially thankful to Martin Mühlegger for being a friendly office-mate, sharing his expertise, a careful reading of my thesis abstract and his kind help on German translation of the abstract.

I am especially grateful to my family for their love, moral support and encouragement. Special thanks to my husband, Anuj Kumar, and my daughter, Apoorva for their love and understanding.

Curriculum Vitae of Pooja Chaudhary

Personal

Date of birth: 16 April 1979
Place of birth: Uttar Pradesh (India)
Nationality: Indian
Current address:
Max Planck Institute for Extraterrestrial Physics
P. O. Box 1312, 85741 Garching, Germany
Tel: (+49) 89 30000-3341

E-mail: chaudhary@mpe.mpg.de

Permanent address:
208, Prempuri
Muzaffarnagar, Uttar Pradesh, India

Educational Qualifications

September 2007 – present:

Pursuing PhD in the High Energy Astrophysics under the International Max-Planck Research School on Astrophysics (IMPRS) program, at Max Planck Institute for Extraterrestrial Physics (MPE), Garching, Germany
PhD Thesis Project: Properties of the integrated spectrum of active galactic nuclei
Thesis Supervisor: Prof. Dr. Günther Hasinger

November 2003 – November 2006:

Research Fellowship at Indian Space Research Organization (ISRO) Satellite Center (ISAC), Banglore, India under the supervision of Dr. P. Sreekumar, Head Space Astronomy and Instrumentation Division, ISAC, Banglore

Projects:

- NainiTal-Cape Survey (A collaborative program initiated between India and South Africa) to search for new Northern Hemisphere "roAp" stars and studying them
- Development of the Data Analysis Software Package for the Solar X-ray Spectrometer Low Energy Detector Experiment (SLD) onboard the Indian satellite GSAT-2
- Timing and spectral analysis of solar flares observed with the SLD onboard GSAT-2 and RHESSI (Reuven Ramaty High Energy Solar Spectroscopic Imager)

June 1998 – June 2000
Master of Science (M.Sc.) in Physics from Chaudhary Charan Singh University, Meerut, India

June 1995 – June 1998
Bachelor of Science (B.Sc.) from Kurukshetra University, Haryana, India

Computer Skills:

- Proficiency in data reduction packages and working knowledge of the X-ray and optical astronomy softwares: XMM-SAS (XMM-Newton data reduction and analysis package), XSPEC (an X-ray spectral fitting tool), FTOOLS, QED, IRAF and DS9
- Extensive experience with astronomical databases (e.g. NED, HEASARC, SIMBAD etc.) and cross-correlation of multiwavelength catalogs using TOPCAT
- Operating systems: Linux, Windows
- Languages: C, Awk, TCL, Perl
- Proficiency in graphics tools: Gnuplot, IDL

Participation in Conferences/Schools

- "Astrosat Workshop on Black Holes", 5–11 May, 2005, Mumbai, India
- "National Space Science Symposium", 9–12 February, 2006, Vishakhapattanam, India, poster contribution
- "Scientific Writing for Young Astronomers", 19–21 May, 2008, Blakenberge, Belgium
- "XMM-Newton SSC Consortium Meeting", 15–17 October, 2008, Madrid, oral contribution
- "AGN-mini Workshop", 20 January, 2009, MPE, Garching, oral contribution
- "Mathematica Workshop", 10 March, 2009, MPE, Garching
- "X-ray Astronomy 2009 Conference", 7–11 September, 2009, Bologna, Italy, poster contribution
- "Bash-Python Course", 3–7 May, 2010, MPE, Garching
- "Black Hole Workshop", 7–11 June, 2010, Bad Honnef, Germany, poster contribution
- "First Gravitas Science Meeting", 25–26 October, 2010, MPE, Garching
- "The X-ray Universe 2011", 27–30 June, 2011, Berlin, Germany, poster contribution

Strengths:

- Ability to work hard with complete dedication
- Ability to learn and absorb new skills quickly and apply them professionally
- Honesty and Integrity

Major Skills: Proficiency in the XMM-Newton data reduction, stacking analysis of X-ray sources in the observed and rest-frame, Monte Carlo simulations to assess the robustness of the results, timing and spectral analysis and cross-correlation of the multiwavelength catalogs

Refereed publications
Properties of the integrated spectrum of serendipitous 2XMM catalog sources (Chaudhary et al. 2010, A&A, 518, A58)
Conference proceedings
Fe Kα Line in the Integrated Spectrum of Serendipitous 2XMM Catalog Sources (Chaudhary, P. and Brusa, M. AIP Conf. Proc., 2010, 1248, 407)
Submitted to A&A
Rest-frame stacking of 2XMM catalog sources: Properties of the Fe Kα line

References:

- Prof. Dr. Guenther Hasinger, Institute for Astronomy, Honolulu, USA
- Dr. Marcella Brusa, Max Planck Institute for Extraterrestrial Physics, Garching, Germany
- Dr. Andrea Merloni, Max Planck Institute for Extraterrestrial Physics, Garching, Germany
- Dr. P. Sreekumar, Space Astronomy and Instrumentation Division, ISRO Satellite Center, Bangalore, India